공학박사학위논문

The Design of Soft Gel Conductor based Biological Signal Sensing Devices for Intimate Communication with Human

소프트 젤 기반 전도성 재료를 활용한 생체 신호 감지 소자 설계에 대한 연구

2019년 8월

서울대학교 대학원

재료공학부

임 승 민

소프트 젤 기반 전도성 재료를 활용한 생체 신호 감지 소자 설계에 대한 연구

THE DESIGN OF SOFT GEL CONDUCTOR BASED BIOLOGICAL SIGNAL SENSING DEVICES FOR INTIMATE COMMUNICATION WITH HUMAN

지도교수: 주 영 창

이 논문을 공학박사 학위논문으로 제출함

2019년 8월

서울대학교 대학원

재료공학부

임 승 민

임 승 민의 박사학위 논문을 인준함

2019년 7월

위 원 장	선 정 윤	(인)
부 위 원 장	주 영 창	(인)
위 원	최 인 석	(인)
위 원	정 택 동	(인)
위 원	김 병 준	(인)

ABSTRACT

The Design of Soft Gel Conductor based Biological Signal Sensing Devices for Intimate Communication with Human

Seung-Min Lim
Department of Materials Science and Engineering
The Graduate School
Seoul National University

Due to the recent advances in electronics, devices are getting close to humans. Integrated on the flexible and stretchable substrates, wearable devices have been widely developed in skin-mountable and implantable forms to detect the various biological signals more directly. However, a large difference in mechanical properties between active components and flexible substrate materials still have been a major issue in forming stable contact with human skin. Furthermore, in case of biological signal sensing, signal transfer in human-machine interfaces also can be a critical issue due to the differences in signal carriers (*i.e.* electrons and ions). In this respect, a new design of active components in wearable devices as well as supporting materials is required considering their mechanical compliance and signal transfer efficiency with biological systems, respectively.

In this study, the solutions for the issues in wearable devices have been suggested by using soft gel based-conductors as an active component of wearable sensing devices.

Firstly, the mechanical reliability of epidermal sensor was improved by introducing soft-gel type conductors as an electrode material for capacitive type stretchable strain sensors (Chapter 3). Due to their entangled polymeric conduction network, conductive gels have an inherent mechanical flexiblity with the unique mechano-electrical characteristics, thus the fabricated devices show a high stretchability until 400 % with a stable mechanical endurance. As all of device components were based on soft materials, it shows an excellent mechanical compliance when mounted on skins. Furthermore, a way to improve the sensing performance of capacitive type strain sensor was suggested by embedding a re-entrant auxetic frame within Ecoflex™ dielectric layer.

Secondly, an ionic signal processing device was designed for the direct communication with ion-based biological signals (Chapter 4 & 5). To date, biological signals have been acquired by electronic devices using metal electrodes or conjugated electroactive polymers. However, since the signals from a biological system are mainly based on ions, the fundamental signal carrier mismatch between electrical devices and biological tissue has made direct communication persistently difficult to facilitate, creating the high impedance at human-machine interfaces (HMIs). Furthermore, as the amount of ions acquired from biological systems is very small, it is required to amplify the weak ionic signals for the effective signal processing. However, the physics of signal amplification in an ionic system has not been introduced yet, and it is very difficult to apply the mechanism of signal amplification for electrical semiconductors to an ionic system because ions are relatively heavier than electrons, so that they have low mobility. In this study, the unique sensing and amplification mechanisms were demonstrated based on the inherent features of ionic systems. By designing an open junction structure in microfluidic chip-based ionic diodes, ionic signals from the external environment can

be directly transmitted to an ionic diode. Moreover, the minute ionic signals injected to the devices and also can be amplified to a large amount of ions. The signal transduction mechanism of the ion-to-ion amplification is suggested and clearly verified by systematic case studies. Finally, various methods for enhancing the amplification are suggested through the scaling down of devices.

Keywords: Wearable strain sensor, Stretchable conductor, Microfluidic chip, Ionic diode, Ionic signal amplification, Polyelectrolyte hydrogel,

***Student Number*:** 2013-20618

Table of Contents

Chapter 3. Soft Conductive Gel based Stretchable Strain Sensor for Epidermal Applications

Chapter 4. Development of Open Junction Ionic Diode for Direct Ionic Signal Sensing

Chapter 5. Ion-to-Ion Amplification through Open Junction Ionic Diode

LIST OF TABLES

LIST OF FIGURES

Figure 2.3 Inherently soft conductors by polymeric composites. (a) Schematic illustration and (b) images of PEDOT:PSS/Polyacrylamide organo-gel. The LED circuits interconnected with gel conductors can be operated under the large deformations. (c) *I-V* characteristics and (d) measured resistivity of PEDOT:PSS /Polyacrylamide organo-gels with respect to concentration of PEDOT:PSS. (e) Resistance changes-strain curves from 1st to 1000th cycles. The strain-insensitive behavior of PEDOT:PSS/ Poly-acrylamide organo-gels was demonstrated. (f) Schematics to depict the microstructure and (g) measured electrical characteristics of PEDOT:PSS/Polyacrlyamide nanoweb.

Figure 2.4 Schematics for showing strain-responsive mechanisms of (a) resistive and (b) capacitive type stretchable strain sensors.

Figure 2.5 (a) Schematics for composition of hydrogels. Hydrogels are composed of polymeric network and water. (b) Basic characteristics of hydrogels. Based on their inherent softness with containing a large amount of water, hydrogel shows excellent flexible and biocompatible properties. Also, hydrogels have merits for ion transportation.

Figure 2.6 Charge transport in electrolyte and polyelectrolyte. (a) Mobile ions in hydrogel. (b) Mobile ions and fixed charge of polymer chains in polyelectrolyte hydrogel.

Figure 4.11 (a) Device configuration for ion injection. The volume of injected ionic solution was precisely controlled using a picoliter injector. Nonpolarizable Ag/AgCl electrodes were connected to the reservoir for in situ current measurement upon ion injection. (b) Microscopic images of open junction ionic diode before ion injection.

Figure 4.12 Schematic illustrations and fluorescence images indicating how the distribution of injected ions is monitored. (a) After the injection of the Rhodamine 6G fluorescent cations, most of the green fluorescence was observed in the pSPA region. (b) The injected fluorescent sodium salt anions were observed in the pDADMAC region, indicating ion injection into the devices through the open junction.

Figure 4.13 Schematics showing the expected behavior of ionic signal detection through an OJID. (a), (b) In the reverse biased state of devices, mobile counter ions in polyelectrolyte gels are depleted and only small leakage current can be measured. (c), (d) Through the ion injection to the open junction structure, ionic signals from external environment can be directly transmitted to active elements of devices and also detected by the ionic current peak.

Figure 4.14 The change of ionic currents in the OJID during ion injection through the open structure of devices. The minute ionic signals can be detected in the form of reverse current peak.

Figure 5.1 (a) Schematic representation of an OJID. Through the ion-injectable hole structure formed on the polyelectrolyte gel region, ionic signals can be directly transmitted to the active element of devices. (b-d) Suggested signal amplification mechanism by ion injection. (b) In the reverse-biased state of an OJID, the depletion region is formed in the diode, and mobile ions in the reservoir are piled up at reservoir/gel interfaces by charge repulsion. (c) When an ion is injected through the open junction, local charge neutralization in the diode occurs, and in addition to the injected ions, (d) an additional breakdown current from the reservoir can be observed.

Figure 5.2 (a) Schematic depictions and (b) images of fluorescence induced by Cu^{2+} ion after ion injection. When Rhodamine B hydrazide (RBH) was incorporated into the reservoir on the pSPA side, red fluorescence emerged after KCl injection to the open junction, which was caused by the Cu^{2+} ion flux induced by the breakdown of the ionic diode.

Figure 5.3 (a) Schematic illustrations and (b) images of fluorescence induced by OH^- ion flux after ion injection. As pH-sensitive carboxylfluorescein (cFlu) dye was introduced into the reservoir on the pDADMAC side, OH^- based anionic flux was visualized through cyan fluorescence.

Figure 5.4 (a) 2D model and boundary conditions for numerical simulation. (b) Before ion injection, Cl^- ions were piled up at the reservoir/gel interface by charge repulsion. When ions were injected into the open junction at 1 s, charge neutralization in pSPA occurred locally, and the breakdown current (Cl^- ion flux) could be observed on the reservoir side.

Figure 5.5 (a) Change of detected charge amount during ion-to-ion amplification calculated by using FEM simulation. Considering that the transportation of co-ions in OJID is based on temporary breakdown of diodes, it was fitted by a sigmoidal Weibull function (red line). (b) Expected ionic current behavior through the differentiation of fitted curve in (a).

Figure 5.6 *I-V* sweep curves of various OJIDs with respect to (a) reservoir ionic solution and (b) width of constituent polyelectrolyte gels. The scan rate during the *I-V* sweep was set to 25 mV/s.

Figure 5.7 Changes in responsive ionic current after ion injection. Amplified ionic current began to flow when an ionic signal was injected and lasted for 20-30 s. (a) When the ion concentration in the reservoir was increased from 1 mM to 0.1 M, a remarkable change in the breakdown current was measured, thus (b) increasing the charge amount detected from the current peak.

Figure 5.8 Changes of responsive ionic currents with respect to the bias conditions. (a) An additional increase in the breakdown currents was observed by varying the reverse-bias voltage conditions; this increase is related to the increase in the field applied to the diodes during breakdown. (b) The variation of the detected charge amount well matched the simulation results.

Figure 5.9 Comparison of the ion-to-ion amplification performance with the hole position. The representative image of OJIDs where the hole is located on (a) pSPA and (b) pDADMAC gel side. (c) The change in the responsive breakdown ionic current and (d) detected charge amount upon ion injection with respect to the position of hole. Despite the change of hole position, the characteristics of responsive current peak were nearly unchanged.

Figure 5.10 Breakdown current response map of various OJIDs considering the cations in the reservoir and injected ionic solutions. As the hydrated ionic radius increases ($K^+ < Na^+ < Li^+$), the ion mobility in the polyelectrolyte gels decreases, which yields different signal responses with varying constituent ions.

Figure 5.11 Measured charge amount from responsive current peak of various OJIDs with respect to the cation species in the reservoir and injected ionic solutions.

Figure 6.2 (a) Illustrations of expected percolation network in PEDOT:PSS-Ag nanowire/PAAm hybrid organogels. (b) SEM images of freeze dried PEDOT:PSS-Ag nanowire hybrid nanocomposites solute. The percolation network of Ag nanowire was well dispersed in PEDOT:PSS matrix. (c) Electrical conductivity of the hybrid organogels with varying contents of Ag nanowire. (d) Resistance changes of hybrid organogels during the repeated deformation. Continuous resistance decreases of hybrid gel were measured until 5000 cycles.

Figure 6.3 (a) Images of guided hippocampus neurons on the glass chip. (b) Propagation of an action potential in neurons mediated by transportation of cations (Na^+, K^+) across the cell membrane through the each ion channel. (c) Schematics for showing the suggested mechanisms of recording neuronal signals upon somatic stimulation by using an OJID.

CHAPTER 1

Introduction

1.1. Wearable devices for intimate communications with human

Electronic devices have been rapidly evolved with the remarkable progress of fabrication technologies. Previously, the development of electronic devices was mainly focused on improvement of computing performance. Followed by the Moore's law, scaling down of semiconductor devices was performed continuously, which leads to the integration of the high density memory and logic devices[1.1].

Along with the performance improvement, nowadays, electronics are developing in a new way to be incorporated into humans, which called wearable devices (**Figure 1.1**). The main purpose of integrating such a wearable device is to achieve an intimate communication with physical and biological signals from humans. Therefore, the design of wearable devices is mostly determined by the types of signals from the human body.

Figure 1.2 presents the various signals occurring from the human body. In terms of sensing distance, the signals can be classified into three parts. First of all, in case of acoustic (sound) signals and images (*e.g.* recognition of face or iris), they can be detected even at a long distance. These signals can be measured by the conventional computing devices with the advanced signal processing systems. Secondly, there are signals which occur near the skins such as deformations from human activities and temperature changes. To detect these signals, electronic devices should be designed in a skin-mountable form. Therefore, the various sensing devices have been fabricated on the flexible and stretchable substrate for the epidermal applications[1,2]. Furthermore, beyond the skin-mountable forms, the implementation of biointegrated devices have been researched to detect the biological signals such as ion transfer in the brain activity or pH changes in biological systems[1,3,4]. To date, intensive researches have been performed to realize the wearable devices by considering the mechanical flexibility and biocompatibility. For the commercialization of wearable devices, however, further optimization of the active element of devices is required for the signal processing with high stability and efficiency. The issues in previously reported wearable devices will be discussed subsequently.

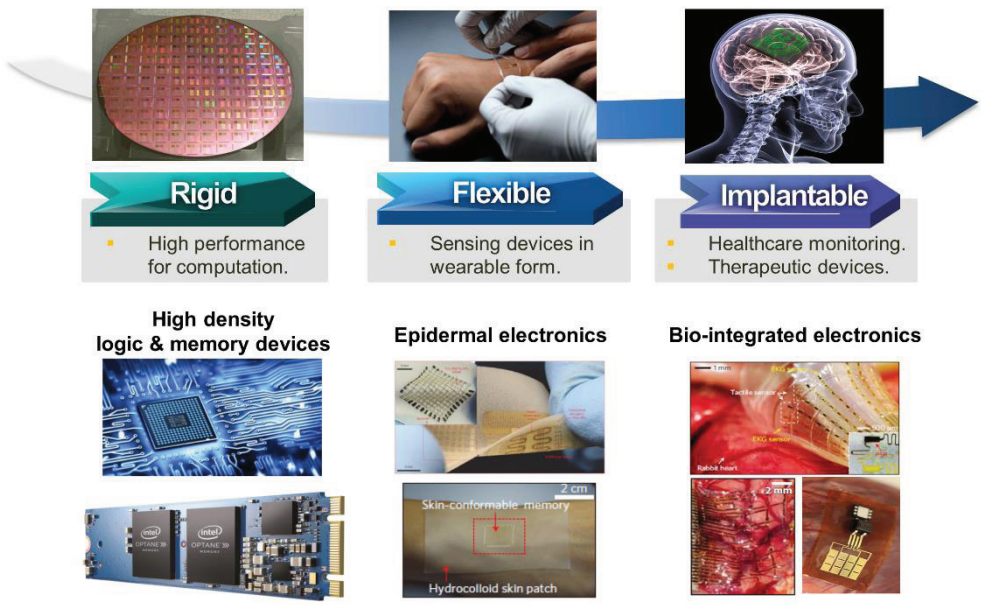

Figure 1.1 Technology trends of electronic devices[1.1-4].

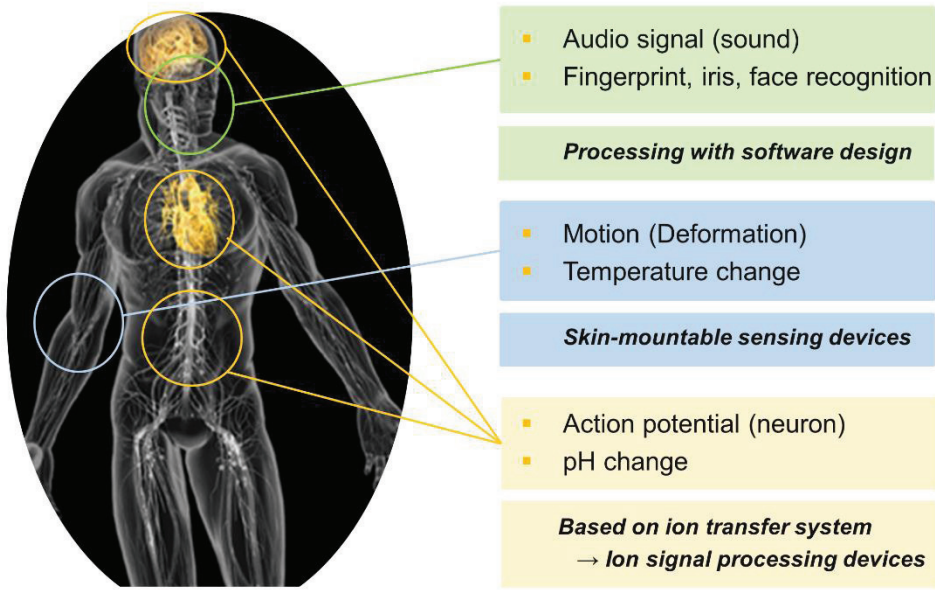

Figure 1.2 Schematics for presenting various signals from human bodies.

1.2. Issues in wearable devices

1.2.1. Stretchable conductors for epidermal sensors

Recent progress in wearable electronics has called for its use for epidermal sensors. The physical, chemical, and environmental status of humans can be directly monitored by integrating various sensing elements on stretchable substrates (*e.g.* PDMS, Ecoflex™) with consideration of the mechanical compatibility with skins[1.5,6]. Epidermal sensors can be utilized as various areas such as healthcare monitoring devices, motion detectors and artificial skins for the soft robotics (**Figure 1.3a**)[1.7-9].

To fabricate the epidermal sensors, the stretchable conductors as well as supporting materials are required to transport electrical signals under various mechanical deformation. Up to date, the conducting components for wearable sensors have been implemented by introducing wavy patterned conducting films using compressed buckling methods or metallic nanomaterials (*e.g.* Ag nanowires, CNT) embedded in elastomers[1.10]. However, when they integrated on devices, it has a severe issue in mechanical instability such as continuous disconnection of percolation network or delamination at interfaces under large deformations, which results in a degradation of sensitivity and reliability of devices. (**Figure 1.3b-d**)[1.11].

These issues are closely related to the large difference of mechanical properties (elastic modulus and Poisson's ratio) between conducting elements and flexible substrates. For the practical use, it is essential to develop the inherently soft material-based conductors by considering the mechanical compliance with soft matrix and human skins[1.12, 13].

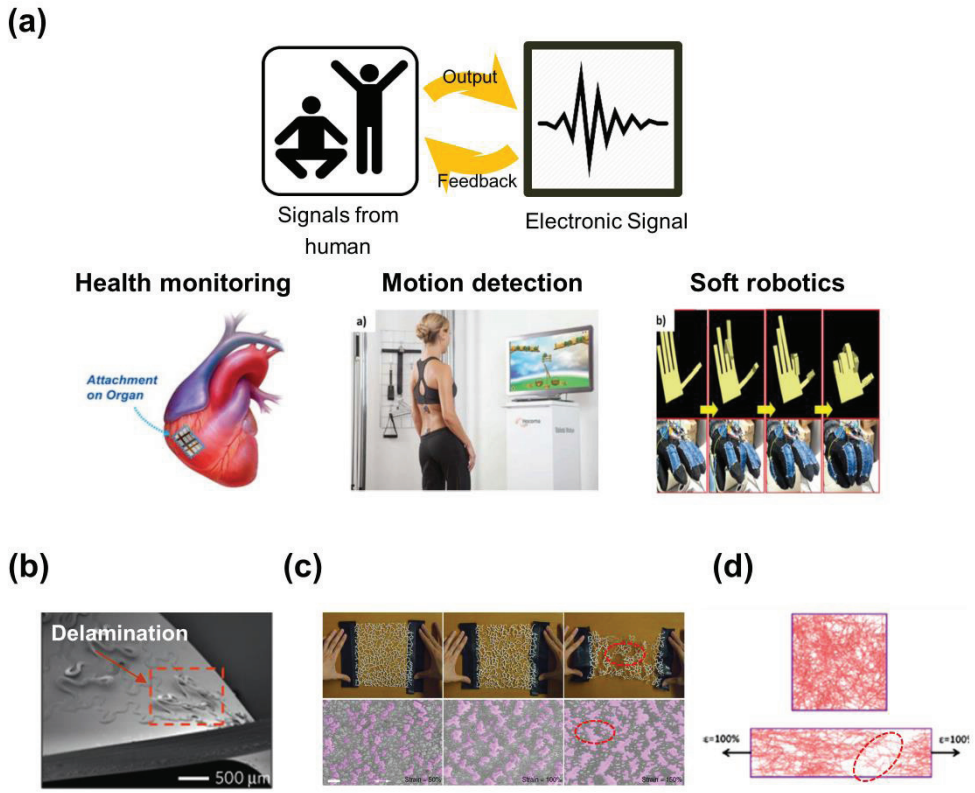

Figure 1.3 (a) Schematics for showing the main principles and functionalities of wearable sensors[1.6-8]. (b-d) Issues in conventional metal based stretchable conductors. Under the harsh deformation, (b) delamination between film and substrate and (c), (d) structural degradation of conductive elements can occur due to their inherently rigid mechanical properties[1.9, 13-14].

1.2.2. Practical issues in biointegrated devices

Beyond the epidermal devices inspired by stretchable electronics, electronic devices are being incorporated into human bodies (**Figure 1.4a**). The development of the bio-integrated devices[1.7,16] which can sense and transmit signals for the communications with biological systems has resulted in its use in a wide range of healthcare applications such as diagnosis for electroencephalography (EEG)[1.17], cardiac electrophysiology [1.18], and drug delivery devices[1.19].

To detect the signals from biological areas, microelectrode patches[1.20,21] fabricated on flexible organic substrate have been widely used (**Figure 1.4b, c**). Since the patch-type electrodes can form a conformal contact to the surface of brain or hearts, the mapping of neural and cardiac signals is available. Furthermore, additional improvement of biointegrated devices have been suggested recently by using biodegradable materials to give a convenience for disposal of devices after transient use[1.22].

However, there are some issues in electronics-based bio-integrated devices for the intimate communications between biotic and abiotic systems since the signal transfer system in biological area is mainly based on the ion transportation. The fundamental mismatch of signal carriers between electrical devices and biological area leads to high impedance at human-machine interfaces (HMIs)[1.23,24]. Therefore, signals acquired through the microelectrodes by capacitive coupling[1.25] between electronic and ionic charges are have made direct communication with biological areas persistently difficult to facilitate. Thus, we are still in need of biocompatible devices that can directly interpret the biological signals with consideration of ion-based signal transfer characteristics.

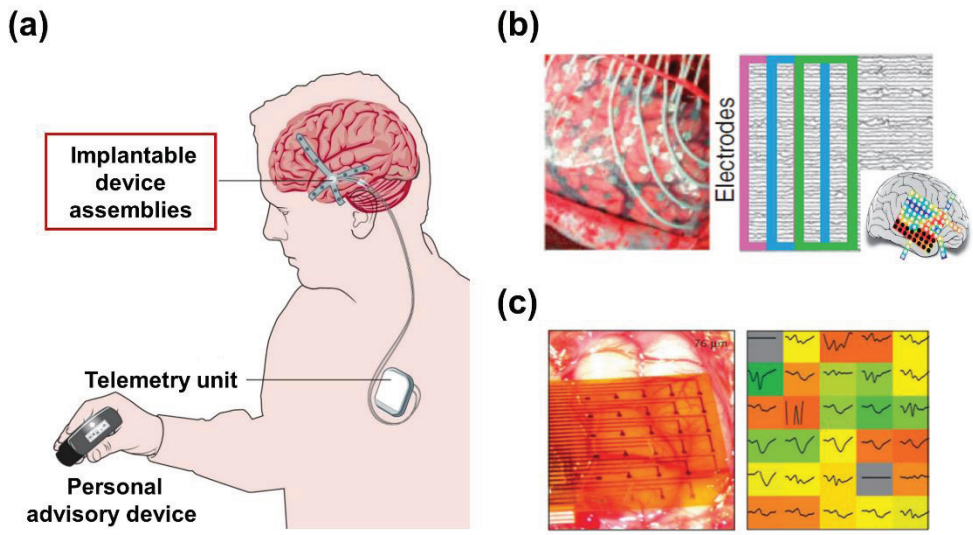

Figure 1.4 (a) Major components of bio-integrated devices[1.26]. (b), (c) Integrated microelectrode patches for recording interfacial brain and cardiac signals[1.20,21].

1.3. Objective of the thesis

Following the Si-based rigid electronics, the rapid evolution of flexible electronics has led to its use in a wide range of wearable applications which can sense various signals from human more closely. Being implemented on the soft and stretchable substrates considering mechanical compliance and biocompatibility, the change of environmental status of humans can be directly detected in epidermal and biointegrated platforms. However, it is still required to consider the issues in active component of wearable devices for the practical applications, which causes the degradation of mechanical reliability and low signal transfer efficiency with biological systems, respectively.

The objective of this thesis is to solve the issues in wearable devices by introducing soft gel conductors as an active element of devices. The first focus is to enhance mechanical reliability of wearable strain sensor. By using a conducting polymer based soft gel conductor as an electrode, the highly stretchable capacitive type strain sensor can be fabricated. Since all components of devices is based on soft materials, it shows mechanical invisibility when worn on to skins. Furthermore, the sensing performance of devices can be improved by incorporating a re-entrant auxetic frame within Ecoflex™ dielectric layer, which overcomes the theoretical limit of capacitive type strain sensor.

The second objective is to design an ionic device which can directly interpret ionic signals from biological systems. By designing an open junction structure, ionic signals from the external environment can be directly transmitted to an ionic diode. Moreover, the principles of signal amplification in ionic systems was investigated, which can be called ion-to-ion amplification. The signal transduction mechanism of the ion-to-ion amplification is suggested and clearly verified by revealing the generation of breakdown

ionic currents during an ion injection.

By taking advantages of gels that show highly mechanical flexibility and biocompatibility due to their inherent softness with a large amount of liquid, gel-based conductors have a merit for improving mechanical and conductive property of wearable devices. Our findings can point to future opportunities for more interactive communications with humans through the epidermal or bio-integrated devices.

1.4. Organization of the thesis

This thesis consist of six chapters. In Chapter 2, basic information on wearable devices, which contains soft material-based wearable electronics, strain–responsive mechanisms of stretchable strain sensor, research backgrounds of hydrogel based ionic conductors and device applications are explained in detail. Chapter 3 shows the results of development of mechanically reliable stretchable strain sensor by using conducting polymer-based gel conductors for epidermal applications. In Chapter 4, the architecture design of ionic devices, called open junction ionic diodes, for direct communication of ionic signals from external environments is introduced. In Chapter 5, the mechanism of the ion-to-ion signal amplification in open junction ionic diodes is discussed. Finally, Chapter 6 summarized the result of this study.

References

[1.1] Bourzac, K. Has Intel Created a Universal Memory Technology? *IEEE Spectrum* **54**, 9-10, doi:10.1109/MSPEC.2017.7906883 (2017).

[1.2] Son, D. *et al.* Multifunctional wearable devices for diagnosis and therapy of movement disorders. *Nat Nanotechnol* **9**, 397-404, doi:10.1038/nnano.2014.38 (2014).

[1.3] Kim, D. H. *et al.* Materials for multifunctional balloon catheters with capabilities in cardiac electrophysiological mapping and ablation therapy. *Nat Mater* **10**, 316-323, doi:10.1038/nmat2971 (2011).

[1.4] Dagdeviren, C. *et al.* Conformal piezoelectric energy harvesting and storage from motions of the heart, lung, and diaphragm. *Proc Natl Acad Sci U S A* **111**, 1927-1932, doi:10.1073/pnas.1317233111 (2014).

[1.5] Amjadi, M., Kyung, K.-U., Park, I. & Sitti, M. Stretchable, Skin-Mountable, and Wearable Strain Sensors and Their Potential Applications: A Review. *Advanced Functional Materials* **26**, 1678-1698, doi:10.1002/adfm.201504755 (2016).

[1.6] Trung, T. Q. & Lee, N. E. Flexible and Stretchable Physical Sensor Integrated Platforms for Wearable Human-Activity Monitoringand Personal Healthcare. *Adv Mater* **28**, 4338-4372, doi:10.1002/adma.201504244 (2016).

[1.7] Pang, C., Lee, C. & Suh, K. Y. Recent advances in flexible sensors for wearable and implantable devices. *Journal of Applied Polymer Science* **130**, 1429-1441, doi:10.1002/app.39461 (2013).

[1.8] Patel, S., Park, H., Bonato, P., Chan, L. & Rodgers, M. A review of wearable sensors and systems with application in rehabilitation. *J Neuroeng Rehabil* **9**, 21, doi:10.1186/1743-0003-9-21 (2012).

[1.9] Amjadi, M., Pichitpajongkit, A., Lee, S., Ryu, S. & Park, I. Highly stretchable and sensitive strain sensor based on silver nanowire-elastomer nanocomposite. *ACS Nano* **8**, 5154-5163, doi:10.1021/nn501204t (2014).

[1.10] Yao, S. & Zhu, Y. Nanomaterial-enabled stretchable conductors: strategies, materials and devices. *Adv Mater* **27**, 1480-1511, doi:10.1002/adma.201404446 (2015).

[1.11] Dickey, M. D. Stretchable and Soft Electronics using Liquid Metals. *Adv Mater* **29**, doi:10.1002/adma.201606425 (2017).

[1.12] Lee, Y. Y. *et al.* A Strain-Insensitive Stretchable Electronic Conductor: PEDOT:PSS/Acrylamide Organogels. *Adv Mater* **28**, 1636-1643, doi:10.1002/adma.201504606 (2016).

[1.13] Choi, G. M. *et al.* PEDOT:PSS/Polyacrylamide Nanoweb: Highly Reliable Soft Conductors with Swelling Resistance. *ACS Appl Mater Interfaces* **11**, 10099-10107, doi:10.1021/acsami.9b00314 (2019).

[1.14] Kim, R. H. *et al.* Waterproof AlInGaP optoelectronics on stretchable substrates with applications in biomedicine and robotics. *Nat Mater* **9**, 929-937, doi:10.1038/nmat2879 (2010).

[1.15] Guo, C. F., Sun, T., Liu, Q., Suo, Z. & Ren, Z. Highly stretchable and transparent nanomesh electrodes made by grain boundary lithography. *Nat Commun* **5**, 3121, doi:10.1038/ncomms4121 (2014).

[1.16] Kim, D. H., Ghaffari, R., Lu, N. & Rogers, J. A. Flexible and stretchable electronics for biointegrated devices. *Annu Rev Biomed Eng* **14**, 113-128, doi:10.1146/annurev-bioeng-071811-150018 (2012).

[1.17] Kipke, D. R. *et al.* Advanced neurotechnologies for chronic neural interfaces: new horizons and clinical opportunities. *J Neurosci* **28**, 11830-11838, doi:10.1523/JNEUROSCI.3879-08.2008 (2008).

[1.18] Timko, B. P. *et al.* Electrical recording from hearts with flexible nanowire device arrays. *Nano Lett* **9**, 914-918, doi:10.1021/nl900096z (2009).

[1.19] Zhang, H. B., Jackson, J. K. & Chiao, M. Microfabricated Drug Delivery Devices: Design, Fabrication, and Applications. *Advanced Functional Materials* **27**, doi:ARTN 170360610.1002/adfm.201703688 (2017).

[1.20] Sinha, N. *et al.* Predicting neurosurgical outcomes in focal epilepsy patients using computational modelling. *Brain* **140**, 319-332, doi:10.1093/brain/aww299 (2017).

[1.21] Kim, D. H. *et al.* Dissolvable films of silk fibroin for ultrathin conformal bio-integrated electronics. *Nat Mater* **9**, 511-517, doi:10.1038/nmat2745 (2010).

[1.22] Li, R., Wang, L., Kong, D. & Yin, L. Recent progress on biodegradable materials and transient electronics. *Bioact Mater* **3**, 322-333, doi:10.1016/j.bioactmat.2017.12.001 (2018).

[1.23] Asplund, M., Nyberg, T. & Inganas, O. Electroactive polymers for neural interfaces. *Polym Chem-Uk* **1**, 1374-1391, doi:10.1039/c0py00077a (2010).

[1.24] Lee, H. R., Kim, C. C. & Sun, J. Y. Stretchable Ionics - A Promising Candidate for Upcoming Wearable Devices. *Adv Mater* **30**, e1704403, doi:10.1002/adma.201704403 (2018).

[1.25] Fattahi, P., Yang, G., Kim, G. & Abidian, M. R. A review of organic and inorganic biomaterials for neural interfaces. *Adv Mater* **26**, 1846-1885, doi:10.1002/adma.201304496 (2014).

[1.26] Cook, M. J. *et al.* Prediction of seizure likelihood with a long-term, implanted seizure advisory system in patients with drug-resistant epilepsy: a first-in-man study. *The Lancet Neurology* **12**, 563-571, doi:10.1016/s1474-4422(13)70075-9 (2013).

CHAPTER 2

Theoretical background

2.1. Soft conducting materials for wearable electronics

As devices have become wearable, soft material based electronic devices have been developed by considering the mechanical compatibility with humans. Soft materials are the materials that can be easily deformed by thermal stresses or thermal fluctuations at about room temperatures, which includes liquids, polymer, gels, as well as mots soft biological materials[2.1]. Furthermore, they can be defined by their mechanical properties (Young's modulus less than 100 MPa), which can be flexibly deformed when an external force is applied, and has a very large elastic limit. Taking the advantages of the flexibility and stretchability, soft materials can be widely applied to the wearable strain sensors for healthcare monitoring and actuators for soft robotics, etc (**Figure 2.1**).

For the successful implementation of the soft electronic devices, soft material based

conductors as well as dielectrics are required. For the soft dielectrics, polymeric insulating materials such as elastomers and hydrogels are mainly used. In case of conductors, on the other hand, conventional metal-based materials still have been used by designing their structures with compressed buckled or wavy patterned shape[2.2,3] (**Figure 2.2a**). Also, metal based nanomaterials such as silver nanoparticles or nanowires have been introduced with embedded in elastomer substrate[2.4-6], which shows better stretchability compared to wavy patterned metal films on stretchable substrates (**Figure 2.2b**). Although conventional metal-based conductors shows high electrical conductivities than any other materials, mechanical mismatches between metal-based conductor and stretchable substrates have resulted in irreversible increase of resistance, constrained stretchable areas and severe interface delamination during the large deformation of devices[2.7]. Recently, liquid metals (*e.g.* EGaIn) have been suggested for the stretchable interconnects due to their inherent flexibility with high conductivity. However, liquid metals also have issues in toxicity, cost, resolution limits in patterning electrochemical (oxidation) stability[2.8].

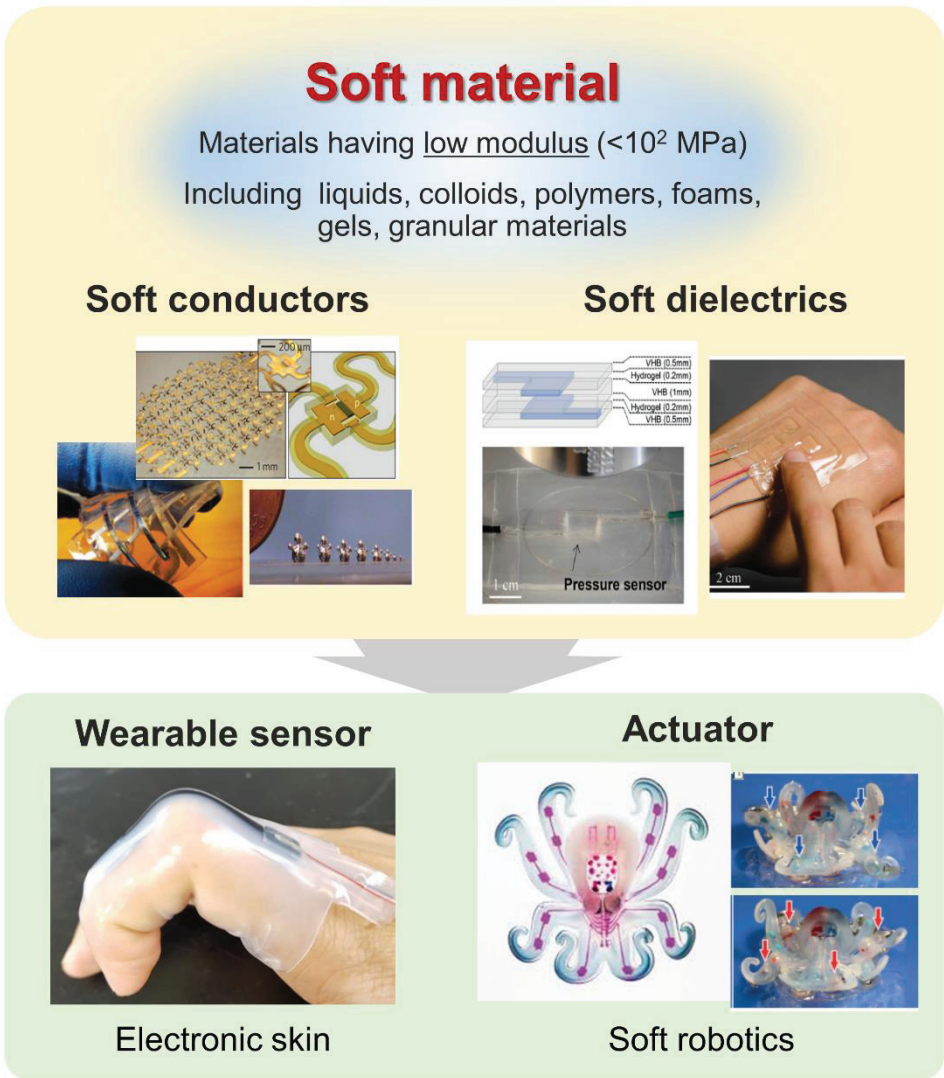

Figure 2.1. Classification of soft materials and device applications for wearable electronics[2.3, 8-10].

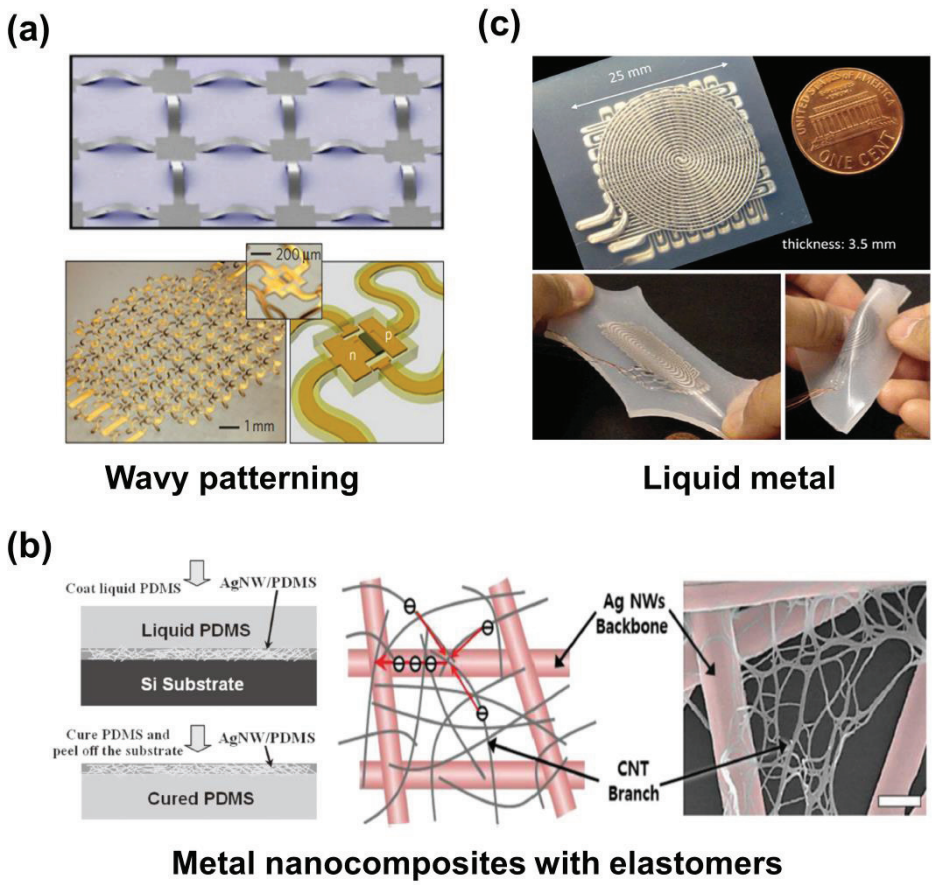

Figure 2.2. Previously reported stretchable conductors for wearable electronic devices[2.2-6, 11].

Therefore, polymer-based naturally soft conductors that can transport electrical signals are required to overcome the mechanical mismatch between conducting elements and supporting materials. In this respect, soft gel-based conducting materials which show the excellent mechanical compliance have been produced by combining conductive polymers with a highly cross-linkable matrix polymer. By using closely packed and partially crystallized poly(3,4-ethylene-dioxythiophene) poly(4-styrenesulphonate) (PEDOT:PSS) sheets as a conducting component, a polymeric conduction network was effectively formed inside the polyacrylamide based gels. For the perfect electric conduction without electrochemical reactions, extra-ions were successfully removed by additional dialysis process, and the water in the gels was fully replaced with the ethylene glycol solvent, which shows a high electrochemical stability. Moreover, due to the entangled polymeric conduction paths in a conductive gel, the change in electrical resistance under tensile strain was minimized without abrupt failure and was almost invariant up to 50% strain (**Figure 2.3a-e)**[2.12].

Furthermore, to improve the percolation network and swelling issues in gel type conductors, PEDOT:PSS/Polyacrylamide nanofiber was also developed. The fabricated PEDOT:PSS/PAAm nanofiber shows improvements in an electrical conductivity as well as mechanical reliability in water since its conduction path is densely packed into nanofiber structure (**Figure 2.3f,g)**[2.13]. However, as the inherent electrical conductivities of conducting polymer is still quite lower than that of metallic materials, it is still required to enhance the electrical conductivities of gel based materials for the practical use.

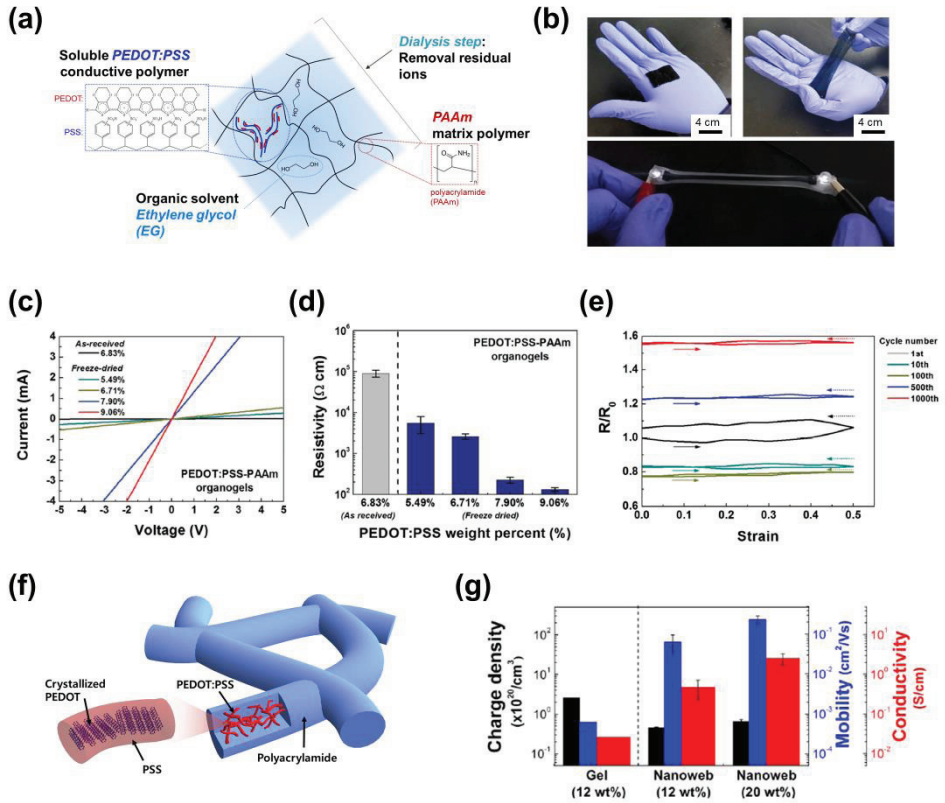

Figure 2.3. Inherently soft conductors by polymeric composites[2.12,13]. (a) Schematic illustration and (b) images of PEDOT:PSS/Polyacrylamide organo-gel. The LED circuits interconnected with gel conductors can be operated under the large deformations. (c) *I-V* characteristics and (d) measured resistivity of PEDOT:PSS /Polyacrylamide organo-gels with respect to concentration of PEDOT:PSS. (e) Resistance changes-strain curves from 1st to 1000th cycles. The strain-insensitive behavior of PEDOT:PSS/ Poly-acrylamide organo-gels was demonstrated. (f) Schematics to depict the microstructure and (g) measured electrical characteristics of PEDOT:PSS/Polyacrlyamide nanoweb.

2.2. Wearable strain sensor

Among the various wearable electronic devices, physical motions of human body can be detected by implementing stretchable strain sensor in a skin-attachable form. A strain sensor is a device that converts mechanical deformation as a change of electrical signals[2.14]. In terms of strain-responsive mechanism, strain sensors are classified into resistive type and capacitive type. The resistive type strain sensors consists of stretchable conductors such as metal-based nanomaterials which can patterned on flexible substrates (**Figure 2.10a**). Considering the geometrical and piezoresistive effects the relative resistance change of strain sensor during the tensile deformation can be expressed as

$$\frac{\Delta \boldsymbol{R}}{\boldsymbol{R}} = (\mathbf{1} + \mathbf{2}\boldsymbol{v})\boldsymbol{\epsilon} + \frac{\boldsymbol{\Delta \rho}}{\boldsymbol{\rho}} \qquad (\boldsymbol{Eq.2.1})$$

where v is the poisson's ratio of substrates, ϵ is the strain and ρ is the resistivity of conductors. Due to the piezoresistive change effects, resistive type strain sensors show a high gauge factor by utilizing the drastic changes in resistivity of conductors such as disconnection of percolation path in metal-based nanomaterials or crack propagations in film typed-stretchable conductors[2.15]. However, as their responsive mechanism are mainly caused by the fracture of electrically active materials, it leads to degradation of the electrical properties under repeated deformations.

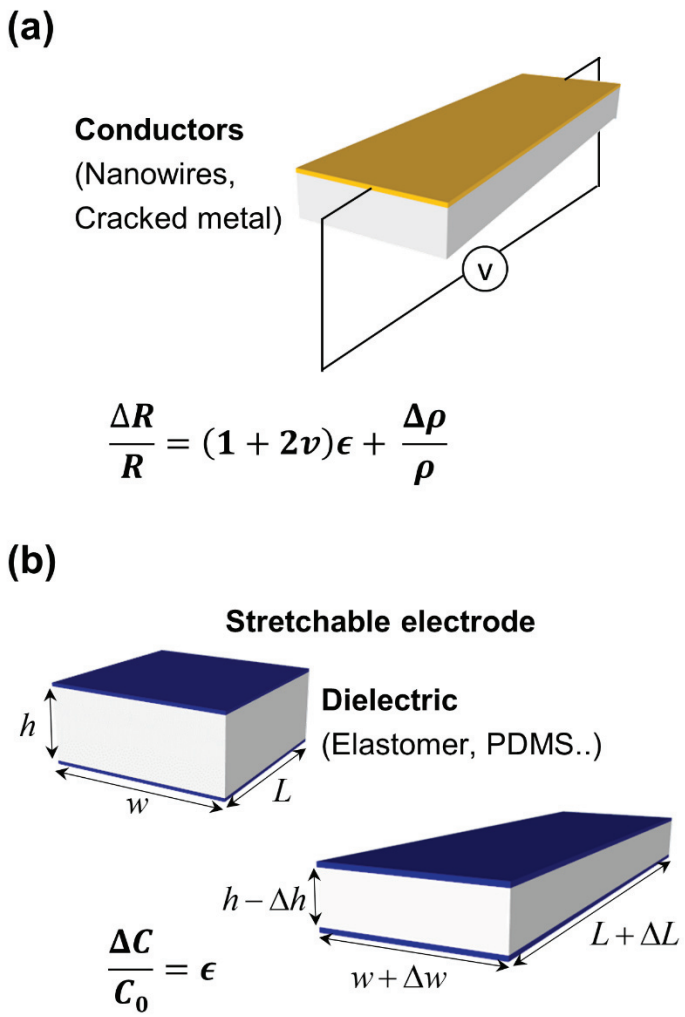

Figure 2.4. Schematics for showing strain-responsive mechanisms of (a) resistive and (b) capacitive type stretchable strain sensors.

In case of capacitive type sensor, which is composed of two stretchable electrodes separated by a stretchable dielectric layer (*e.g.* elastomer, PDMS), the change of capacitance is dependent on the geometrical change of dielectric layer. The initial capacitance of dielectric layer can be expressed as

$$\boldsymbol{C_0 = e_0 e_r \frac{x_0 y_0}{z_0}} \qquad (\boldsymbol{Eq.2.2})$$

where e_0 and e_r are the dielectric constant of vaccum and relative permittivity of dielectric layer, respectively. When stretched to the direction of x-axis, the capacitance changes to

$$\boldsymbol{C = e_0 e_r \frac{x(1+\epsilon_x) y(1+\epsilon_y)}{z(1+\epsilon_z)}} \qquad (\boldsymbol{Eq.2.3})$$

when the dielectric layer is isotropic ($\epsilon_y = \epsilon_z$), it can be expressed to

$$\boldsymbol{C = e_0 e_r \frac{xy(1+\epsilon_x)}{z}} \qquad (\boldsymbol{Eq.2.4})$$

Therefore, the relative change of capacitance can be derived by

$$\boldsymbol{\frac{\Delta C}{C_0} = \frac{C - C_0}{C_0} = \epsilon_x} \qquad (\boldsymbol{Eq.2.5})$$

Through the **Eq. 2.5**, the gauge factor of capacitive type strain sensor (the slope of relative signal changes with tensile strain) can be derived to 1, which is independent to the electrical properties of conductors[2.16, 2.17].

Table 2.1 shows the performance of currently reported stretchable strain sensors with respect to gauge factor, linearity and mechanical reliability. The resistive type strain sensors show a high gauge factor performance even over 10^3. However, their rapid resistance changes also lead to the issues in non-linearity behavior of devices as well as mechanical instability under repeated deformations. On the other hand, the capacitive type stretchable strain sensors have a great advantage in terms of linearity and durability, which also summarized in **Table 2.2**. However, despite the various advantages, the conventional capacitive type strain sensors have a limitation in aspects of sensitivity because the gauge factor is restricted to 1, which is only dependent on the geometric factor of the dielectric layer.

Type	Materials	Gauge factor	Linearity	Maximum stretchability	Repeated cycle	Ref.
Resistive	Carbon black-PDMS	5.5 (~10 %), 1.8 (~ 80%)	Two linear-like region	80 %	30 (10 % strain)	2.18
	Cracked Pt/PUA	2000	Nonlinear	2 % (Nano Crack)	5000 (2 % strain)	2.19
	AuNW-PANI MP-Rubber	13 ~ 31	Nonlinear	150 %	10000 (5 % strain)	2.20
	CNT-PEDOT: PSS-PU	8.7~62.3 (2.5 %)	Nonlinear	100 %	1000 (20 % strain)	2.21
	Carbon paper-PDMS	25.3 (~2 %), 4.73 (~20 %)	Two linear-like region	20 %	1000 (3 % strain)	2.22
	Graphene platelets-Si rubber	27.9	Nonlinear	12 %	1000 (10 % strain)	2.23
Capacitive	vCNT/Ecoflex	~1	Linear	100 %	-	2.24
	CNT-Elastomer	0.99	Linear	100 %	3000 (100 % strain)	2.16
	AgNW/PDMS	~1	Linear	50 %	-	2.4
	AgNW/PDMS	0.8	Linear	100 %	1000 (100 % strain)	2.25

Table 2.1. Performance of currently reported stretchable strain sensors[2.4,16,18-25].

Performance	Resistive	Capacitive
GF (Sensitivity)	Over 10	~1
Linearity	Non-linearity	Good linearity
Hysteresis	Large	Small
Response	Slow	Fast
Overshoot	Large	Small

Table 2.2. Comparison between resistive type and capacitive type stretchable strain sensors with respect to the performance factors[2.15].

2.3. Hydrogel based ionic conductor

2.3.1. Hydrogel

Hydrogels consist of three-dimensional cross-linked polymeric chains and water based solvent (**Figure 2.5a**). Due to their hydrophilic functional group attached to the polymeric backbone, hydrogels can absorb a large amount of water without dissolution. The water inside the hydrogels can facilitate free diffusion of solutes such as ions and molecules with maintaining their shapes by the strong bonding between polymeric chains[2.26].

These half liquid-like properties and half solid-like properties of hydrogels cause many interesting material characteristics, not found in either solid or liquid (**Figure 2.5b**). In terms of mechanical properties, hydrogels are flexible and further stretchable since their mechanical behaviors are mainly based on the cross-linked polymeric network[2.27,28]. Also, hydrogels show an excellent biocompatibility[2.29,30] as hydrogels contain a large amount of aqueous solvent. Furthermore, hydrogels have an advantage for ion transportation[2.31] when they include electrolytes that contain a large quantity of ions. Since the signals in a biological system are mainly based on transportation of ions, hydrogel based-ionic conductors can be used to detect various biological signals by minimizing potential loss at interfaces. Based on these merits, hydrogels can be applied to wearable and bio-integrated devices for the neural signal sensing[2.32] and drug delivery[2.33].

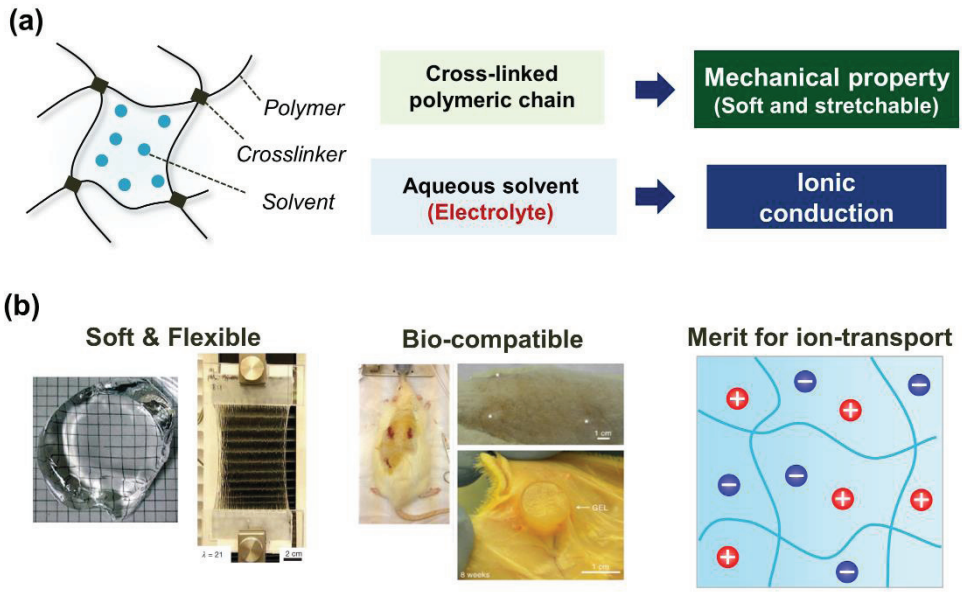

Figure 2.5 (a) Schematics for composition of hydrogels. Hydrogels are composed of polymeric network and water. (b) Basic characteristics of hydrogels. Based on their inherent softness with containing a large amount of water, hydrogel shows excellent flexible and biocompatible properties. Also, hydrogels have merits for ion transportation.

2.3.2. Polyelectrolyte hydrogel

Polyelectrolyte gels are composed of the charged polymer network with macro-ions fixed on the polymer chains, which called polyelectrolytes, neutralized by counter-ions in electrolytes imbibed in gels[2.34]. In case of hydrogels, both positive and negative charges in electrolytes are mobile, and can serve as an ionic conductor as shown in **Figure 2.6a**. However, in case of polyelectrolyte gels, either positive or negative charges in polymer chains are spatially fixed, therefore, only ions of opposite charge on a polymeric backbone are mobile due to Donnan exclusion (**Figure 2.6b**). By utilizing the unique ionic transport behavior of polyelectrolyte gels, it is possible to mimic the semiconductor physics in electronic devices. Inspired by the electronic devices using p- and n-type solid materials, two different types of polyelectrolyte gels can be used as fine substitutes for conventional semiconductors. Unlike metal and silicon, where the absence of electrons make p-type semiconductors, the gel-based semiconductors have actually mobile positive ions with negatively charged polymer backbones, and vice versa.

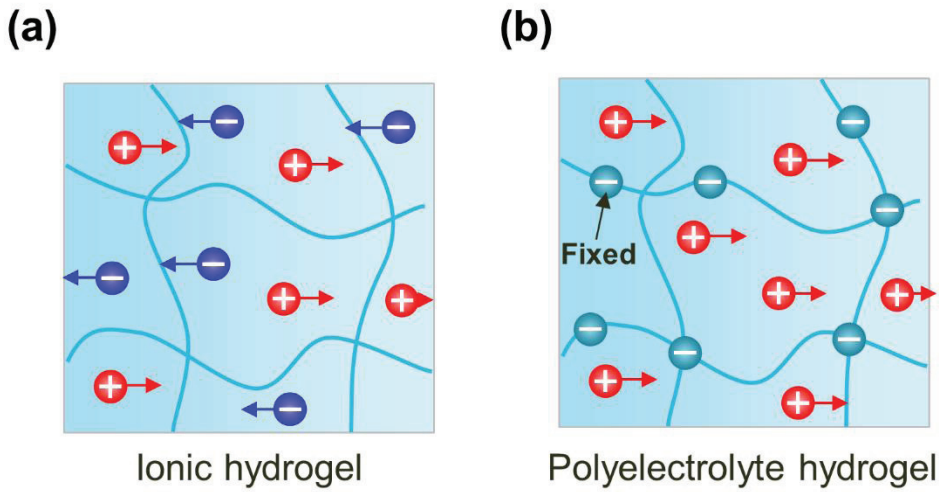

Figure 2.6 Charge transport in electrolyte and polyelectrolyte. (a) Mobile ions in hydrogel. (b) Mobile ions and fixed charge of polymer chains in polyelectrolyte hydrogel.

2.4. Comparison between ionics and electronics

Ionics are signal processing systems operated by delivery of ions as signal carriers. The comparison of key properties between ionics and electronics are presented in **Table 2.3**. In case of electronics, signals are processed by transportation of electrons and holes, which has high field-effect mobility. By utilizing the fast speed of carriers and specialized characteristics such as recombination and tunneling effect, it has merits for designing the signal processing devices such as diodes and field-effect transistors for the rectification and amplification, respectively.

In case of ionics, on the other hand, the size of ions are much larger than electrons and holes, which results in low mobility. Moreover, as recombination of carriers does not occur in ionic systems, it is difficult to expect the high rectification and amplification properties compared to electronic devices, up to date. However, since the signals from biological systems are mainly based on ion transportation (Na^+, K^+, Cl^-, Ca^{2+}, NO, and neurotransmitters), the development of ion-based signal processing systems has been attracted for achieving the direct communication between devices and biological systems[2.35]. Furthermore, another advantage of ionic systems rather than electronics is that it has selectivity for the various kinds of signal carriers in aspect to their size or charge valance, which shows a high order of degeneracy for the biomimic information processing[2.36]. Considering the abovementioned merits, ionic materials, especially in gel types, have been favored for the due to their physical and biological compatible properties[2.33].

	Electronics	Ionics	
Type	Solid	Liquid	Gel
Materials	Metals	Electrolyte	Hydrogel
Signal carrier	Electrons	Ions	
Speed	**Fast**	Slow	
Biocompatibility	No	**Yes**	
Stretchability	Yes	No	**Yes**
Characteristics	Recombination Tunneling	Selectivity by species of ions	

Table 2.3 Comparison of main characterstics between electronics and ionics.

2.5. Recent advances in ionic devices

2.5.1. Previous reported ionic devices

To date, ionic devices have been developed for the effective processing of ionic signals. **Figure 2.7a** shows a nanofluidic diode based on nanotube heterojunctions[2.37] through designing longitudinal heterostructured SiO_2/Al_2O_3 nanotubes with opposite surface charges. By using different pH value at point of zero charge, an asymmetric charge distribution in channel was formed and non-linear current-voltage (*I-V*) characteristics can be produced.

Figure 2.7b presents the rectifying behavior of liquid metal based ionic diodes. By using an electrochemical reaction between liquid metal electrode and aqueous electrolyte solution, self-limiting oxide layer was formed at the interface and ionic current was well rectified at positive bias region, which leads to high rectification ratio up to 450 at ± 5 V by increasing the ion conductivity in electrolyte region[2.38].

Along with the examples abovementioned, polymer based ionic active elements have been widely studied due to their inherent mechanical flexibility for the wearable applications. By introducing ion selective bipolar membranes (**Figure 2.7c**) and polyelectrolyte gels (**Figure 2.7d**) which have fixed charges at polymeric backbones, selective ionic conduction with their charges can be controlled due to Donnan exclusion. More recently, by combining oppositely charged ion selective materials, the rectification characteristics of ion p-n junction[2.39, 2.40] have been demonstrated.

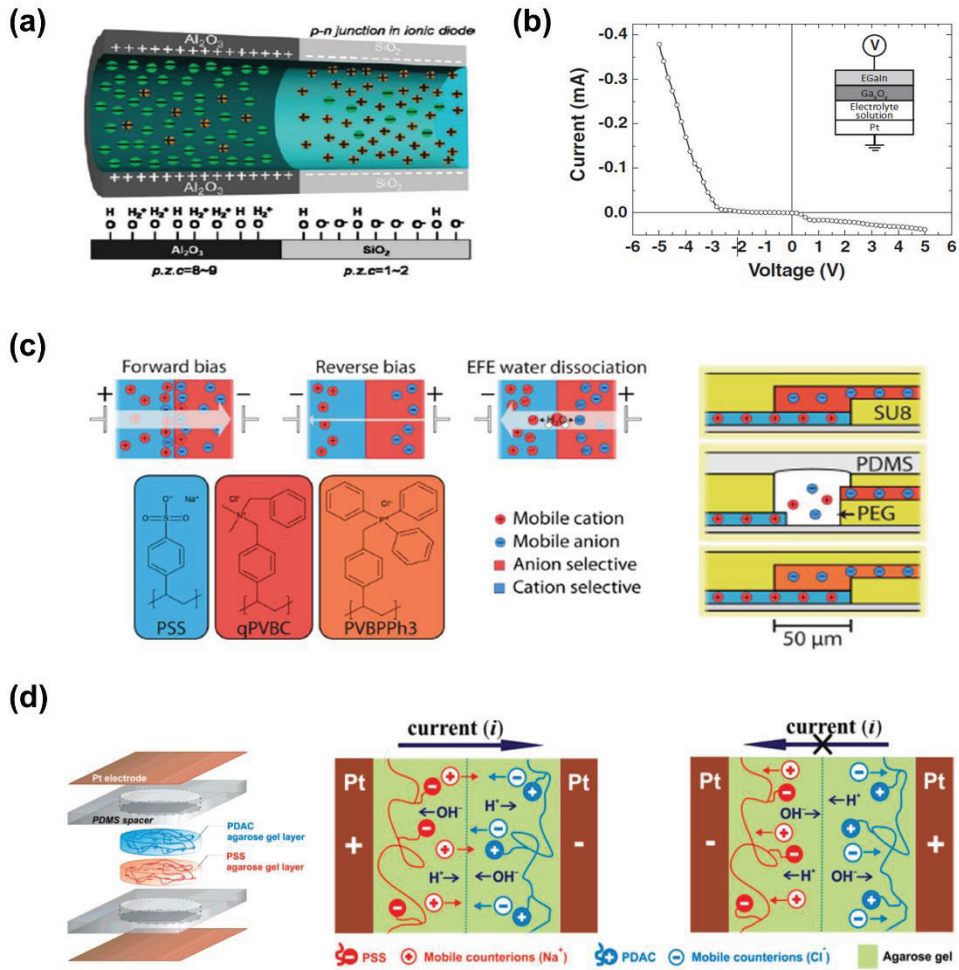

Figure 2.7 Various ionic devices for rectification of ionic currents. (a) Nanofluidic diodes based on heterostructured SiO_2/Al_2O_3 nanotubes[2.37]. (b) Soft-matter diodes by using the oxidation of liquid-metal electrodes[2.38]. Ionic diodes based on polymeric ionic active elements by introducing (c) polyphosphonium-based bipolar membrane[2.39] and (d) polyelectrolyte gels[2.40].

Among the various polymer based ionic active materials, polyelectrolyte gel-based ionic devices have a merit for bio-integration since polyelectrolyte gels contain a large amount of water with the desirable ion conductive properties, which is comparable to the environment of biological area. In this respect, there have been intensively researched for the implementation of gel-based ionic devices with an elaborated structural design.

Figure 2.8a exhibits the polyelectrolyte gel diodes implemented on a microfluidic chip[2.41]. By patterning poly(2-acrylamido-2-methyl-1-propanesulfonicacid) (pAMPSA) as a negatively charged polymeric backbone and poly(diallyldimethy-lammonium-chloride) (pDADMAC) as a positively charged polymeric backbown through the sequential UV-photopolymerization process, ionic active elements were formed in an microfluidic channel of glass chip. As polyelectrolyte gels were well defined at narrow neck-like intersection of channels, the electrical potential drop can be concentrated at junction of ionic gels, which leads to an increase of rectification performance. Furthermore, by replacing Pt electrodes with non-polarizable Ag/AgCl electrodes for the electrical contact with reservoirs, contact resistance can be lowered and high exchange current can be measured (**Figure 2.8b**). Based on the stable rectification performance of ionic diodes, it can be applied to the ionic circuit elements. By patterning two polyelectrolyte gel diodes connected in parallel, ion based AND logic gate can be designed on a microfluidic chip (**Figure 2.8c**).

In addition to the ionic diodes, 3-terminal based ionic circuit elements were also integrated for switching of ionic currents[2.42]. **Figure 2.8d** shows the representative depiction of an ionic field effect transistor (FET) on a microfluidic chip system. By patterning pAMPSA and pDADMAC gels at gate region, ionic currents in microchannel across the source and drain were effectively controlled by the gate voltage (**Figure 2.8e**).

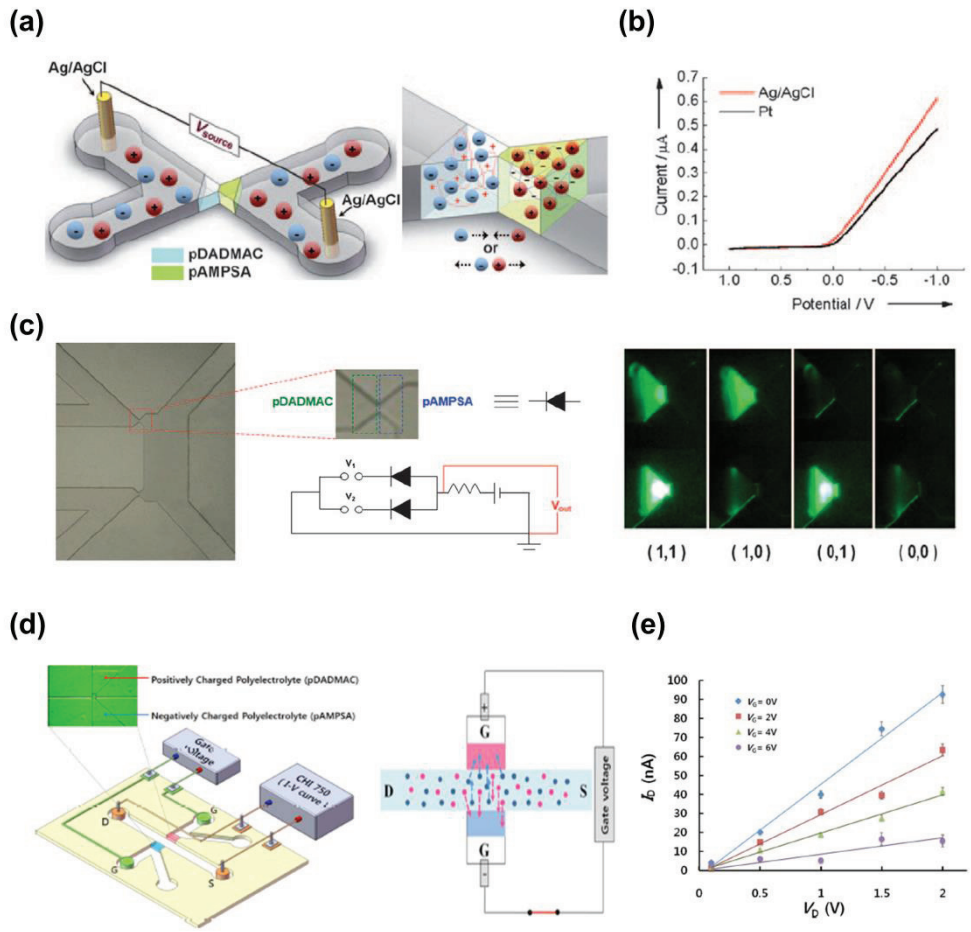

Figure 2.8 (a) Schematics of polyelectrolyte gel based ionic diodes on a microfluidic chip and (b) *I-V* characteristics of polyelectrolyte gel diodes. (c) Ionic logic circuits comprised of two pairs of ionic diodes. The output signals of AND gate were verified by followed fluorescent images[2.41]. (d) Representative illustrations of polyelectrolyte junction field effective transistor (FET) and (e) output transfer curve of and ionic FET[2.42].

Through the implementation of ionic devices on microfluidic-chip, Stable operation of ionic circuits can be verified in an aqueous system with the micro-scaled design.

2.5.2. Rectification behavior of polyelectrolyte gel ionic diodes

The nonlinear *I-V* characteristics of polyelectrolyte gel ionic diodes seem to be similar to these of conventional semiconductor based diodes, but there are some differences in the mechanism of rectification caused by different signal carriers (*i.e* Electron and holes vs. Ions). **Figure 2.9** presents *I-V* sweep characteristics and schematics for explaining the rectification behavior of polyelectrolyte gel based ionic diodes[2.43]. When the forward bias are applied to ionic diodes, a large amount of mobile counter-ions from reservoir electrolytes crosses the polyelectrolyte gel regions and forms accumulation state of devices, leading to high penetration currents in diodes. The *I-V* characteristics of ionic diodes at forward scan region is similar to these of solid-state electronics. However, the level of current density is markedly lower than that of semiconductor-based diodes because the relatively large charge carriers have a rather low mobility.

On the other hand, as the reverse bias voltages are applied to devices, the hysteresis behavior can be observed, which was not found in semiconductor physics. Since recombination of carriers does not occur in an ionic system, ions in a polyelectrolyte gel junction need to be migrated back to reservoir electrolyte regions for the formation of depletion state of devices. After getting into the depletion state, only small ionic current occurs, which results in non-linear *I-V* characteristics of devices. The rectification current is suggested by water dissociation at the junction as well as leakages in gels since large potential drops are generated in a depletion region adjacent to junction[2.36, 2.44].

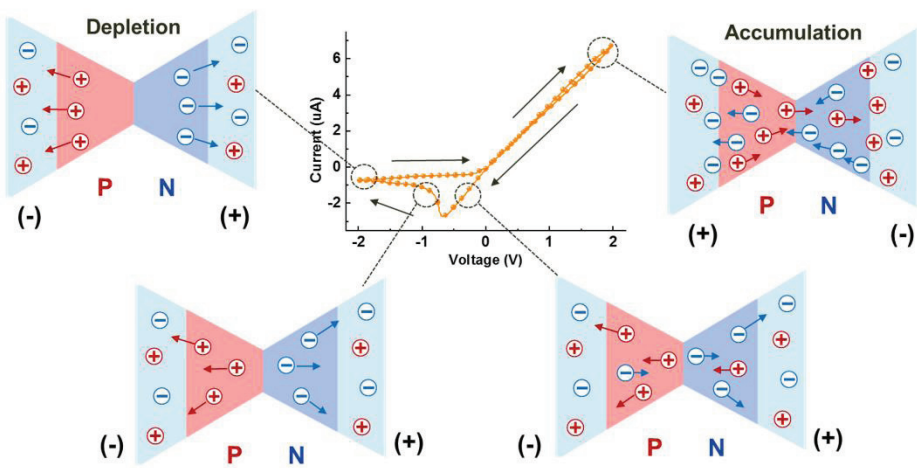

Figure 2.9 (a) *I-V* sweep curves and schematics for depicting rectification behavior of polyelectrolyte gel ionic diodes[2.43].

Based on the working mechanism of polyelectrolyte gel based ionic diodes, various case studies were conducted to characterize the effect of the rectification property of devices. **Figure 2.10a** shows the changes of *I-V* hysteresis curve of ionic diodes[2.43] as a function of the voltage scan rate. At a low scan rate of 10 mV/s, the small hysteresis area of *I-V* curves was shown because it takes a sufficient time to reach the equilibrium state of the devices with bias. However, as the voltage scan rate increased from 10 mV/s to 100 mV/s, the reverse current peak was also increased while the level of forward current was maintained, which clearly shows the hysteresis behavior of ionic devices caused by slow ion transportation. When the concentration of reservoir electrolyte solution increases, the rapid increase of current level at forward bias as well as hysteresis area under the reverse bias was observed (**Figure 2.10b**). This indicates that the transmittance of ionic signals in ionic diodes is highly related to ions in reservoir as well as the structural design of polyelectrolyte gels.

Through the recent advnaces in ionic devices, an effective processing of ionic signal such as rectification and switching has been well demonstrated. However, for the advanced applications such as an integration with the biological areas, the differences between the solid state electronics and ionic systems should be considered since most of the currently proposed ionic devices have been implemented in accordance with fundamentals of electronics. In this respect, it is now important to take advantage of the unique characteristics of ionic systems for designing ion-based signal transfer devices.

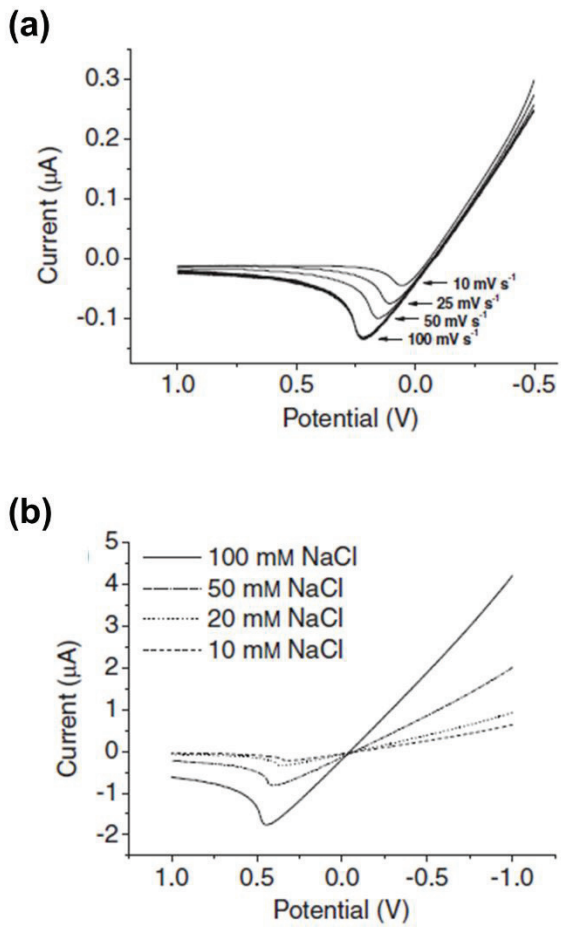

Figure 2.10. The change of hysteresis curve of ionic diodes with respect to the (a) voltage scan rate and (b) concentration of reservoir solution[2.36, 2.43].

References

[2.1] Soft materials - Latest research and news, Nature, <https://www.nature.com/subjects/soft-materials>

[2.2] Kim, D. H. & Rogers, J. A. Stretchable Electronics: Materials Strategies and Devices. *Advanced Materials* **20**, 4887-4892, doi:10.1002/adma.200801788 (2008).

[2.3] Kim, R. H. *et al.* Waterproof AlInGaP optoelectronics on stretchable substrates with applications in biomedicine and robotics. *Nat Mater* **9**, 929-937, doi:10.1038/nmat2879 (2010).

[2.4] Xu, F. & Zhu, Y. Highly conductive and stretchable silver nanowire conductors. *Adv Mater* **24**, 5117-5122, doi:10.1002/adma.201201886 (2012).

[2.5] Hyun, D. C. *et al.* Ordered zigzag stripes of polymer gel/metal nanoparticle composites for highly stretchable conductive electrodes. *Adv Mater* **23**, 2946-2950, doi:10.1002/adma.201100639 (2011).

[2.6] Lee, P. *et al.* Highly Stretchable or Transparent Conductor Fabrication by a Hierarchical Multiscale Hybrid Nanocomposite. *Advanced Functional Materials* **24**, 5671-5678, doi:10.1002/adfm.201400972 (2014).

[2.7] 이유용. A Study on the Mechanical Deformation dependent Electrical Property Change in PEDOT:PSS Conductive Polymer for Stretchable Electronic Conductor. (2016).

[2.8] Dickey, M. D. Stretchable and Soft Electronics using Liquid Metals. *Adv Mater* **29**, doi:10.1002/adma.201606425 (2017).

[2.9] Sun, J. Y., Keplinger, C., Whitesides, G. M. & Suo, Z. Ionic skin. *Adv Mater* **26**, 7608-7614, doi:10.1002/adma.201403441 (2014).

[2.10] Wehner, M. *et al.* An integrated design and fabrication strategy for entirely soft,

autonomous robots. *Nature* **536**, 451-455, doi:10.1038/nature19100 (2016).

[2.11] Yong-Lae, P., Bor-Rong, C. & Wood, R. J. Design and Fabrication of Soft Artificial Skin Using Embedded Microchannels and Liquid Conductors. *IEEE Sensors Journal* **12**, 2711-2718, doi:10.1109/jsen.2012.2200790 (2012).

[2.12] Lee, Y. Y. *et al.* A Strain-Insensitive Stretchable Electronic Conductor: PEDOT:PSS/Acrylamide Organogels. *Adv Mater* **28**, 1636-1643, doi:10.1002/adma.201504606 (2016).

[2.13] Choi, G. M. *et al.* PEDOT:PSS/Polyacrylamide Nanoweb: Highly Reliable Soft Conductors with Swelling Resistance. *ACS Appl Mater Interfaces* **11**, 10099-10107, doi:10.1021/acsami.9b00314 (2019).

[2.14] Park, J., You, I., Shin, S. & Jeong, U. Material approaches to stretchable strain sensors. *Chemphyschem* **16**, 1155-1163, doi:10.1002/cphc.201402810 (2015).

[2.15] Amjadi, M., Kyung, K.-U., Park, I. & Sitti, M. Stretchable, Skin-Mountable, and Wearable Strain Sensors and Their Potential Applications: A Review. *Advanced Functional Materials* **26**, 1678-1698, doi:10.1002/adfm.201504755 (2016).

[2.16] Cohen, D. J., Mitra, D., Peterson, K. & Maharbiz, M. M. A highly elastic, capacitive strain gauge based on percolating nanotube networks. *Nano Lett* **12**, 1821-1825, doi:10.1021/nl204052z (2012).

[2.17] 이영주. Engineering the Deformation Characteristics of Soft Materials through Geometric Design of Auxetics for Flexible Electronics Application. (2017).

[2.18] Kong, J.-H., Jang, N.-S., Kim, S.-H. & Kim, J.-M. Simple and rapid micropatterning of conductive carbon composites and its application to elastic strain sensors. *Carbon* **77**, 199-207, doi:10.1016/j.carbon.2014.05.022 (2014).

[2.19] Kang, D. *et al.* Ultrasensitive mechanical crack-based sensor inspired by the spider sensory system. *Nature* **516**, 222-226, doi:10.1038/nature14002 (2014).

[2.20] Gong, S. *et al.* Tattoolike Polyaniline Microparticle-Doped Gold Nanowire Patches as Highly Durable Wearable Sensors. *ACS Appl Mater Interfaces* **7**, 19700-19708, doi:10.1021/acsami.5b05001 (2015).

[2.21] Roh, E., Hwang, B. U., Kim, D., Kim, B. Y. & Lee, N. E. Stretchable, Transparent, Ultrasensitive, and Patchable Strain Sensor for Human-Machine Interfaces Comprising a Nanohybrid of Carbon Nanotubes and Conductive Elastomers. *ACS Nano* **9**, 6252-6261, doi:10.1021/acsnano.5b01613 (2015).

[2.22] Li, Y. *et al.* Highly Flexible Strain Sensor from Tissue Paper for Wearable Electronics. *ACS Sustainable Chemistry & Engineering* **4**, 4288-4295, doi:10.1021/acssuschemeng.6b00783 (2016).

[2.23] Shi, G. *et al.* Highly Sensitive, Wearable, Durable Strain Sensors and Stretchable Conductors Using Graphene/Silicon Rubber Composites. *Advanced Functional Materials* **26**, 7614-7625, doi:10.1002/adfm.201602619 (2016).

[2.24] Shin, U.-H. *et al.* Highly stretchable conductors and piezocapacitive strain gauges based on simple contact-transfer patterning of carbon nanotube forests. *Carbon* **80**, 396-404, doi:10.1016/j.carbon.2014.08.079 (2014).

[2.25] Lee, G. *et al.* Omnidirectionally and Highly Stretchable Conductive Electrodes Based on Noncoplanar Zigzag Mesh Silver Nanowire Arrays. *Advanced Electronic Materials* **2**, doi:10.1002/aelm.201600158 (2016).

[2.26] Gerlach, G. & Arndt, K.-F. *Hydrogel sensors and actuators*. (Springer, 2009).

[2.27] Lin, S. *et al.* Stretchable Hydrogel Electronics and Devices. *Adv Mater* **28**, 4497-4505, doi:10.1002/adma.201504152 (2016).

[2.28] Ono, T., Sugimoto, T., Shinkai, S. & Sada, K. Lipophilic polyelectrolyte gels as super-absorbent polymers for nonpolar organic solvents. *Nat Mater* **6**, 429-433, doi:10.1038/nmat1904 (2007).

[2.29] Takahashi, H., Itoga, K., Shimizu, T., Yamato, M. & Okano, T. Human Neural Tissue Construct Fabrication Based on Scaffold-Free Tissue Engineering. *Adv Healthc Mater* **5**, 1931-1938, doi:10.1002/adhm.201600197 (2016).

[2.30] Darnell, M. C. *et al.* Performance and biocompatibility of extremely tough alginate/polyacrylamide hydrogels. *Biomaterials* **34**, 8042-8048, doi:10.1016/j.biomaterials.2013.06.061 (2013).

[2.31] Lee, H. R., Kim, C. C. & Sun, J. Y. Stretchable Ionics - A Promising Candidate for Upcoming Wearable Devices. *Adv Mater* **30**, e1704403, doi:10.1002/adma.201704403 (2018).

[2.32] Viventi, J. *et al.* Flexible, foldable, actively multiplexed, high-density electrode array for mapping brain activity in vivo. *Nat Neurosci* **14**, 1599-1605, doi:10.1038/nn.2973 (2011).

[2.33] Peppas, N. A., Hilt, J. Z., Khademhosseini, A. & Langer, R. Hydrogels in biology and medicine: From molecular principles to bionanotechnology. *Advanced Materials* **18**, 1345-1360, doi:10.1002/adma.200501612 (2006).

[2.34] Harland, R. S., Prud'homme, R. K. & National Meeting of, A. *Polyelectrolyte gels : properties, preparation, and applications / Ronald S. Harland, editor, Robert K. Prud'homme, editor*. (Washington, DC : American Chemical Society, 1992).

[2.35] Sjostrom, T. A. *et al.* A Decade of Iontronic Delivery Devices. *Adv Mater Technol-Us* **3**, doi:ARTN 170036010.1002/admt.201700360 (2018).

[2.36] Chun, H. & Chung, T. D. Iontronics. *Annu Rev Anal Chem (Palo Alto Calif)* **8**, 441-462, doi:10.1146/annurev-anchem-071114-040202 (2015).

[2.37] Yan, R., Liang, W., Fan, R. & Yang, P. Nanofluidic diodes based on nanotube heterojunctions. *Nano Lett* **9**, 3820-3825, doi:10.1021/nl9020123 (2009).

[2.38] So, J.-H., Koo, H.-J., Dickey, M. D. & Velev, O. D. Ionic Current Rectification in Soft-

Matter Diodes with Liquid-Metal Electrodes. *Advanced Functional Materials* **22**, 625-631, doi:10.1002/adfm.201101967 (2012).

[2.39] Gabrielsson, E. O. & Berggren, M. Polyphosphonium-based bipolar membranes for rectification of ionic currents. *Biomicrofluidics* **7**, 64117, doi:10.1063/1.4850795 (2013).

[2.40] Cayre, O. J., Chang, S. T. & Velev, O. D. Polyelectrolyte diode: Nonlinear current response of a junction between aqueous ionic gels. *J Am Chem Soc* **129**, 10801-10806, doi:10.1021/ja072449z (2007).

[2.41] Han, J. H., Kim, K. B., Kim, H. C. & Chung, T. D. Ionic circuits based on polyelectrolyte diodes on a microchip. *Angew Chem Int Ed Engl* **48**, 3830-3833, doi:10.1002/anie.200900045 (2009).

[2.42] Kim, K. B., Han, J.-H., Kim, H. C. & Chung, T. D. Polyelectrolyte junction field effect transistor based on microfluidic chip. *Applied Physics Letters* **96**, doi:10.1063/1.3389492 (2010).

[2.43] Han, J. H. *et al.* Ion flow crossing over a polyelectrolyte diode on a microfluidic chip. *Small* **7**, 2629-2639, doi:10.1002/smll.201100827 (2011).

[2.44] Yamamoto, T. & Doi, M. Electrochemical mechanism of ion current rectification of polyelectrolyte gel diodes. *Nat Commun* **5**, 4162, doi:10.1038/ncomms5162 (2014).

CHAPTER 3

Soft Conductive Gel based Stretchable Strain Sensor for Epidermal Applications

3.1. Introduction

With a recent advance of flexible electronics, wearable devices have been widely developed for the intimate communications with humans. In particular, wearable stretchable strain sensors, which convert mechanical deformations to electrical signals in a skin-mountable form, can be utilized to broad applications such as real-time health monitoring[3.1,2] in a medical industry, human-machine interfaces controllers for soft robotics[3.3,4] and motion capturing[3.5] for entertainment device systems[3.6].

For the practical use of stretchable strain sensors for wearable applications, it is required to improve the reliability of devices (*e.g.* maximum stretchability and

endurance with cyclic deformation) as well as their sensing performance. Therefore, it is required to consider the mechanical stability between electrical components (active elements and interconnects) and flexible supporting materials. However, as the most of electrical components of stretchable strain sensors are designed by using metal-based conductors, the mechanical failure between the conductor and the substrate is inevitable. For the fundamental solution of the mechanical instability issues in currently reported wearable sensors, it is essential to introduce soft-electronic materials for an active element of devices as well as supporting materials.

In this respect, gel-based conducting materials, which called conductive gels, have recently attracted a great interest for the application to stretchable electronic devices. Conductive gels are polymeric materials that contain conductive polymers as a conducting element in highly cross-linkable matrix polymers[3.7,8]. Due to their inherent softness with a large stretchability (up to 300~ 400 %), conductive gels have a high potential for application to epidermal electronics[3.9,10]. Furthermore, as their entangled polymeric conduction paths lead to invariant resistance change under stretch[3.9], the conductive gels are compatible for electrodes of capacitive type wearable sensors.

Here, we fabricated a soft material-based capacitive strain sensor by using conductive gels as an electrode material. Due to the mechanical compliance between conducting components and supporting materials, the fabricated device shows an excellent stretchability with a high endurance and it can be successfully utilized to epidermal applications such as finger and elbow motion sensing. Subsequently, a method for improving gauge factors of capacitive type strain sensor was suggested by incorporating a re-entrant auxetic frame within Ecoflex™ dielectric layer.

3.2. Experiments

3.2.1. Preparation of conductive gel

For the soft electrical component for wearable application, poly(3,4-ethylene-dioxythiophene) poly(4-styrenesulphonate) (PEDOT:PSS)/Polyacrylamide (PAAm) conductive organo-gel was synthesized, followed by the previous work[3.9]. In detail, freeze dried PEDOT:PSS solute (Clevios P, Heraeus), acrylamide monomer (Sigma-Aldrich) and N,N`-methylenebisacrylamide crosslinker were dissolved in mixture of de-ionized water ethylene glycol (Sigma-Aldrich). In this work, weight percent of PEDOT:PSS solute to Acrylamide was 11 wt%. For the gelation, ammonium persulfate initiator and N,N,N′,N′-Tetramethyl-ethylenediamine accerlerator were added to pre-gel solution and heated on 90 °C for 2 h in a glass mold. Fabricated gels were washed into mixture solution of de-ionized water and ethylene glycol for the purification. Subsquently, an aqueous component in gels was selectively evaporated by heating on 60 °C for 4 h in dry oven to prevent electrochemical reaction when electrically biased.

3.2.2. Fabrication of stretchable strain sensor

The capacitive type stretchable strain sensor was implemented by attaching the PEDOT:PSS organo-gel based electrodes on the Ecoflex™ 0010 dielectric layer, as presented in **Figure 3.1**. 0.5 mm thick PEDOT:PSS organo-gel plate was cut into rectangular shape (0.5 cm×1.5 cm) by CO_2 laser cutter and heated on 60 °C for 15 min in dry oven to remove the moisture at gel surface for the stable electrical contact. The

electrical contact of sensors was formed by Ni wire with the Ag paste, and subsequently coated by Ecoflex™ to prevent from drying of organo-gel. After encapsulation, devices were turned upside down and the same process was repeated at the opposite surface of Ecoflex™ dielectric layer.

3.2.3. Device characterization

For the *in-situ* measurement of change in capacitance under tensile and compressive strain, fabricated strain sensors were loaded on tensile machine (Instron 3343) which is fixed with acryl clamps and electrically contacted with precision LCR meter (Keysight, E4980AL) (**Figure 3.2**). The measuring voltage and frequency were 1 V and 10 kHz, respectively. Each sample was uniaxially deformed until 100 % of strain with a displacement rate of 3 mm/min. The change of capacitance was measured once per second. To confirm the endurance performance of device, cyclic tensile fatigue test was performed by using a tensile machine. (MMT-500N, Shimadzu) The range of stretch was 30 % and repeated for 5000 times with a 0.05 Hz of rate.

3.2.4. Preparation of the auxetic elastomer

A 0.5-mm-thick polyurethane (PU) sheet was cut into a re-entrant auxetic pattern using a cutting plotter machine (Silhouette America, Inc.). After cutting, the pre-cured Ecoflex™ solution was molded into the auxetic-patterned PU sheet, filling the porous region of the auxetic frame (**Figure 3.3**). Then, the assembly was cured at room temperature for 1 day.

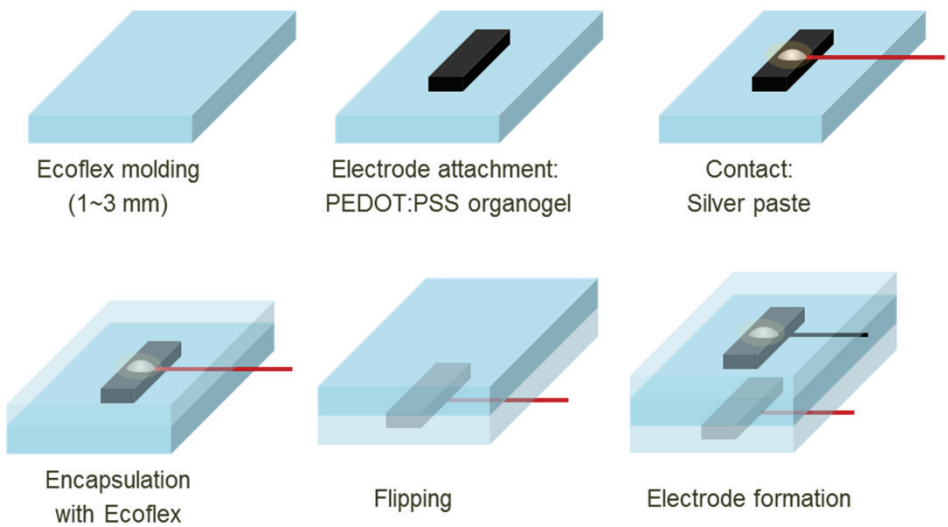

Figure 3.1 (a) Fabrication process of stretchable strain sensor by using PEDOT:PSS/PAAm gel conductor and Ecoflex™ dielectric layer.

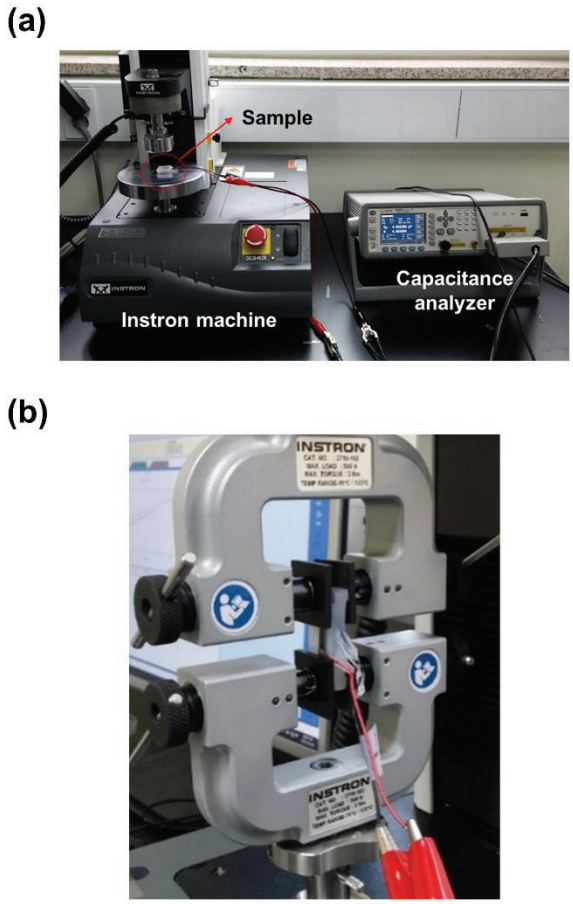

Figure 3.2 Device configuration for characterization of sensing performance of PEDOT:PSS conductive gel/Ecoflex™ capacitive strain sensors under (a) compressive and (b) tensile deformation.

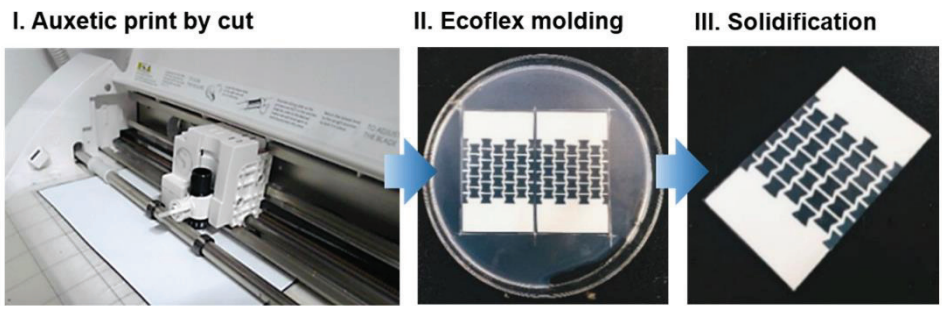

Figure 3.3 (a) Fabrication procedure of auxetic elastomers. (Step I) A 0.5-mm-thick PU sheet was patterned for a specific auxetic design using a cutting plotter (CAMEO; Silhouette). (Step II) Ecoflex™ was molded into the auxetic-patterned PU sheet, filling the porous region of the auxetic structure. (Step III) The auxetic elastomer after the Ecoflex™ had solidified.

3.3. Performance of PEDOT:PSS/PAAm gel-based strain sensor

3.3.1. The change of capacitance with tensile strain

To characterize the performance of conductive gel-based capacitive strain sensors, the changes in electrical signal of fabricated devices were measured during stretch. **Figure 3.4a** presents the absolute capacitance changes of devices under the tensile strain with varying the thickness of inter-dielectric Ecoflex™ layers from 1 mm to 3 mm. The capacitance of all devices was linearly increased with the tensile strain, which can be caused by geometrical change of the dielectric layer between gel electrodes. Although the absolute value of capacitance increased with the decrease of thickness of inter-dielectric layers, the relative change of capacitance was nearly unchanged regardless of the dimension of devices (**Figure 3.4b**).

However, the initially fabricated sensors have a relatively low gauge factor (below to 0.8) compared to the theoretical value (= 1), also showing the fluctuation in capacitance-strain curves during the measurement. This issue comes from the slipping of conductive gels embedded in Ecoflex™ under the stretch (**Figure 3.5a**). To enhance the weak adhesion between gel and elastomers, pre-cured Ecoflex™ was additionally coated on the dielectric layer before locating gel and subsequently cured at 60 °C for 30 min together (**Figure 3.5b**). By introducing the blade-coting process before gel attachment, the gauge factor of devices were highly increased, which can be approached to the theoretical results (**Figure 3.5c**).

Furthermore, the fluctuation issue during the initial measurement also can be caused by slipping of zigs due to the low adhesion property of Loctite 401 adhesive with silicon-

based rubber, which also leads to limiting range of measurement. The adhesion issue in zigs can be solved by combining Loctite 406 and Primer SF 700 adhesives, which guarantees a high measurement range until 400 % stretch. Through the modification of fabrication process, we developed the highly stretchable capacitive strain sensor by using the soft electronic conductors.

3.3.2. The change of capacitance with compressive stress

Along with the stretch, pressure also can be detected through the fabricated sensors. **Figure 3.6** shows the change of capacitance under the compressive stress with varying the thickness of inter-dielectric layers from 1 mm to 3 mm. Due to the pressure applied to the dielectric elastomer layer, the area of gel conductor was increased and the distance between electrodes was decreased, which leads to the increase of capacitance. The capacitance change under pressure shows two-step responsive behavior, which is independent to the thickness of inter-dielectric layers. Although our devices have a wide sensing range, they show low sensitivity (about 10^2~10^3 times) compared to the previously reported pressure sensors[3.11-14]. For further enhancement of sensing performance, advanced material designs in dielectric elastomer layer should be considered such as introducing highly porous structure.

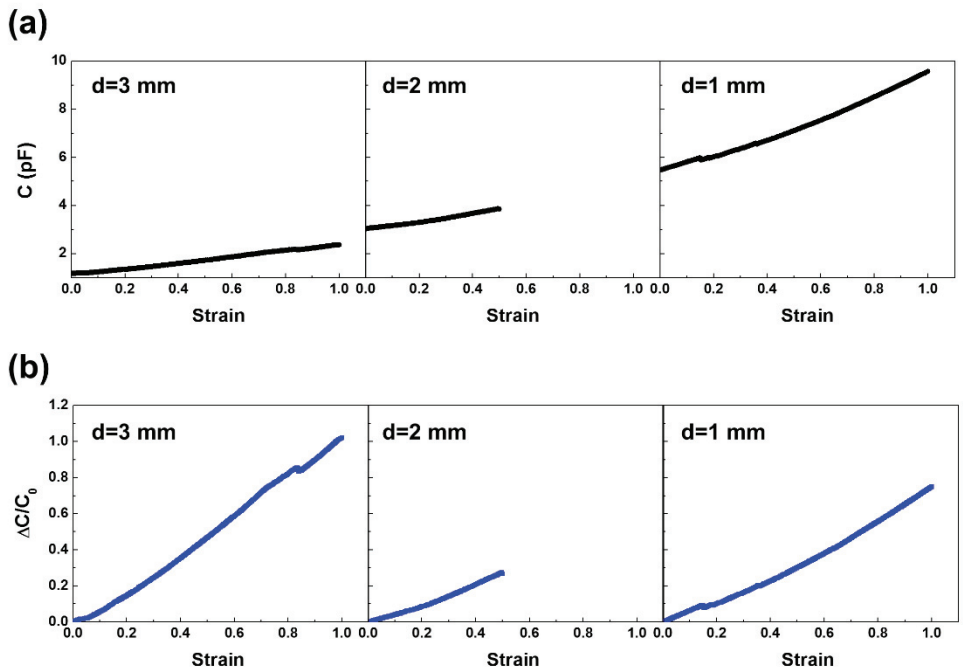

Figure 3.4 The change of (a) absolute and (b) relative capacitance of conductive gel-based capacitive strain sensors under tensile strain. The thickness of inter-dielectric layer varied from 1 mm to 3 mm.

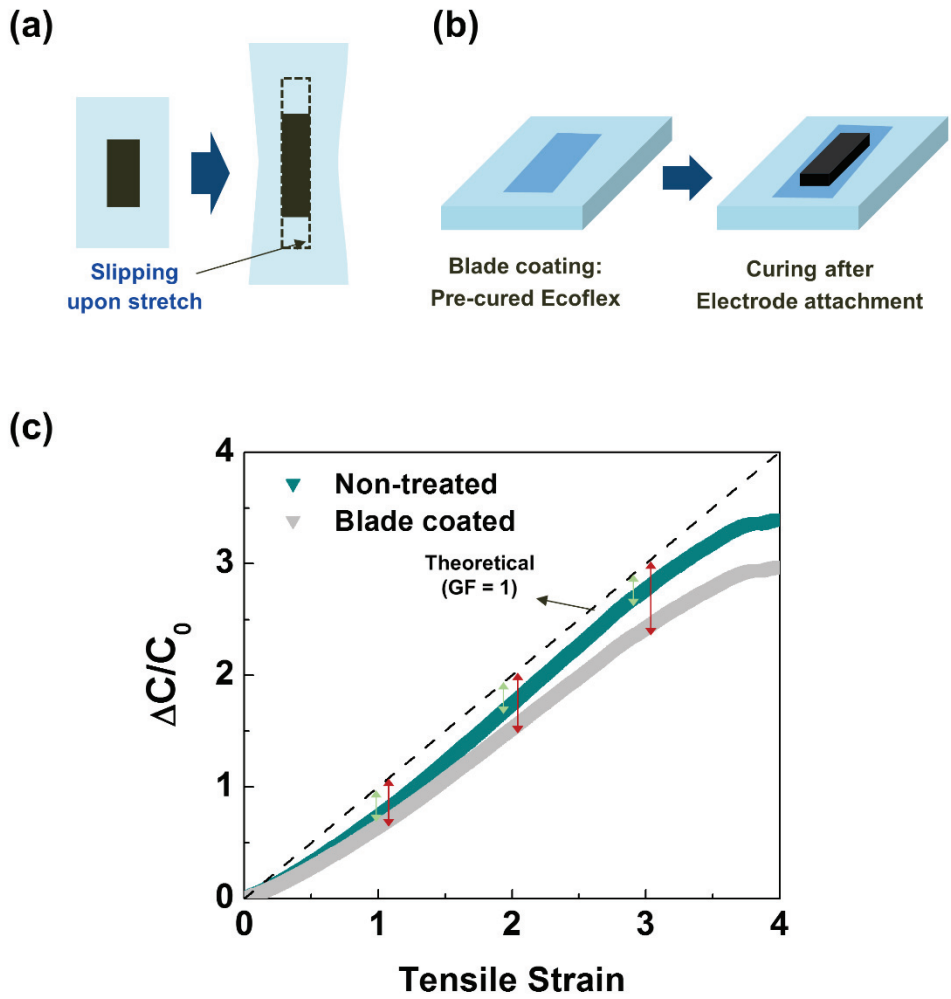

Figure 3.5 (a) Schematics for slipping of gel conductors embedded in Ecoflex™ during stretch. (b) Illustrations for showing blade coating process before attachment of gel conductor. (c) The change of strain-responsive behavior of sensors with blade coated process. The increase of gauge factor was observed by solving slipping issues in gel/elastomer interfaces.

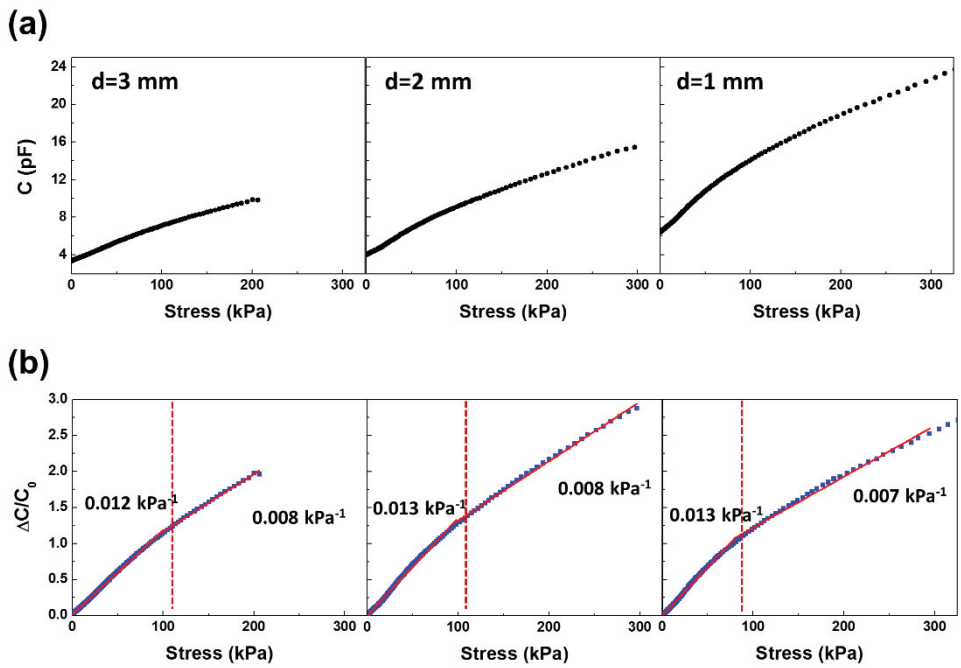

Figure 3.6 The change of (a) absolute and (b) relative capacitance of fabricated sensors under compressive stress with varying the thickness of inter dielectric layers.

3.3.3. Correlation between compressive and tensile strain

The strain-responsive behavior of fabricated strain sensors was compared with theoretical models to evaluate the sensing performance of devices. Considering the isotropic mechanical property of dielectric elastomers, the relative change of capacitance with tensile strain (x direction) can be derived by **Eq 2.5**, which was shown in **Chapter 2**.

$$\frac{\Delta C}{C_0} = \frac{C - C_0}{C_0} = \epsilon_x \qquad (Eq. 2.5)$$

Likewise, the relative capacitance change of devices under compressive strain (z direction) can be expressed as **Eq. 3.1** (We assume that the Poisson's ratio of gel and elastomer is 0.5).

$$\frac{\Delta C}{C_0} = \frac{v^2\epsilon_z^2 + 2v\epsilon_z + \epsilon_z}{1 - \epsilon_z} = \frac{0.25\epsilon_z^2 + 2\epsilon_z}{1 - \epsilon_z} \qquad (Eq. 3.1)$$

Figure 3.7 shows the capacitance change of fabricated sensors under tensile and compressive strain compared with their theoretical models. We can find that the behavior of capacitance changes of our devices under tensile and compressive strain is well matched to the theoretical models. Furthermore, the tensile strain can be detected under extreme deformation conditions even at 400 % of strain, which shows excellent mechanical stretchability of devices.

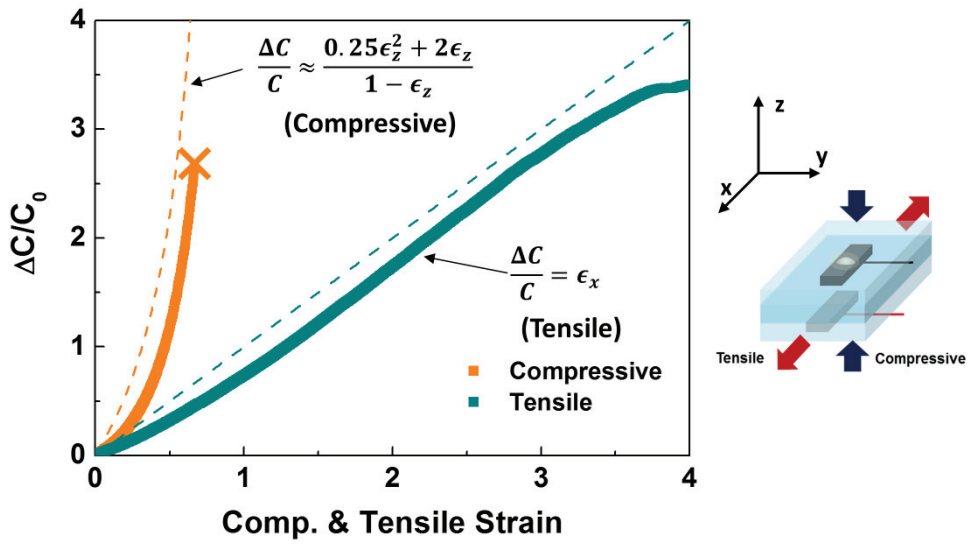

Figure 3.7 The relative capacitance change of conductive gel-based strain sensors under compressive and tensile strain. The dashed lines in graph show theoretical capacitance change behaviors at each strain mode.

3.4. Application to epidermal sensor

3.4.1. Improvement of stability at hard/soft contact region

After measurement of sensing performance, the conductive gel-based strains sensors were fabricated for the epidermal applications. However, when the devices were worn to skins, the mechanical instability in electrical contact region between hard Ag paste layer and soft gel leads to large noise signals under the both static and dynamic conditions (**Figure 3.8a, c and e**). For the improvement of contact stability, we attahced the nylon sheet layer on the Ag pasted layer with adhesive as shown in **Figure 3.8b**. By using non-stretchable nylon sheet layer, the contact region was mechanically fixed and the electrical signals were significantly stabilized under large deformation (**Figure 3.8d, f**), which can be an effective process for the further epidermal applications.

3.4.2. Fabrication of finger motion sensor

The developed sensors were applied to skin mountable devices for detecting human activities. For the comfortable fit to finger, overall thickness of devices was decreased compared to that of test samples. By reducing a thickness of inter-dielectric layer (1 mm→0.3 mm), encapsulation layer (1 mm→0.3 mm) and gel electrode (1 mm→0.5 mm), the devices can be wearable on fingers with minimizing mechanical discomfort (**Figure 3.9a, b**).

Figure 3.9c shows the output performance of the fabricated wearable sensors during the finger motion. The folding and unfolding motions of fingers can be detected by the increase and decrease (recovery) of output capacitance and their sensing performance were maintained at the high speed of motion. Considering that 50 ~ 60 % of tensile strain is applied by folding of fingers, the output capacitance characteristics of devices were well matched to the motions.

From the above results, a fully soft material based strain sensor was developed by using polymeric gel-based conductors for electrode materials. Due to the mechanical compliance between electronic components and flexible supporting materials, our devices have a great potential for application to skin attachable devices.

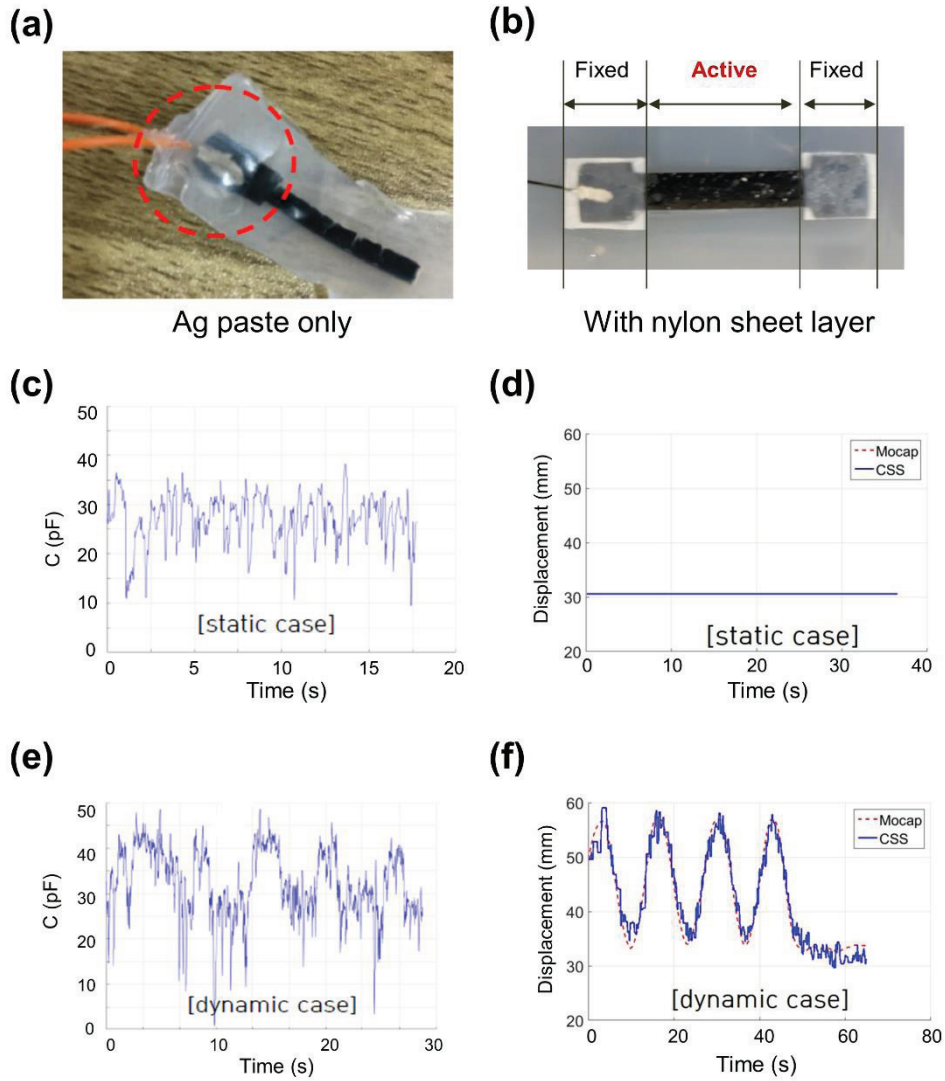

Figure 3.8 The images for formation of contact of devices with (a) only Ag paste and (b) additional nylon sheet layer. (c-f) Due to the fixed contact regions by non-stretchable nylon sheet layers, the output signals of devices can be stabilized when worn to skins.

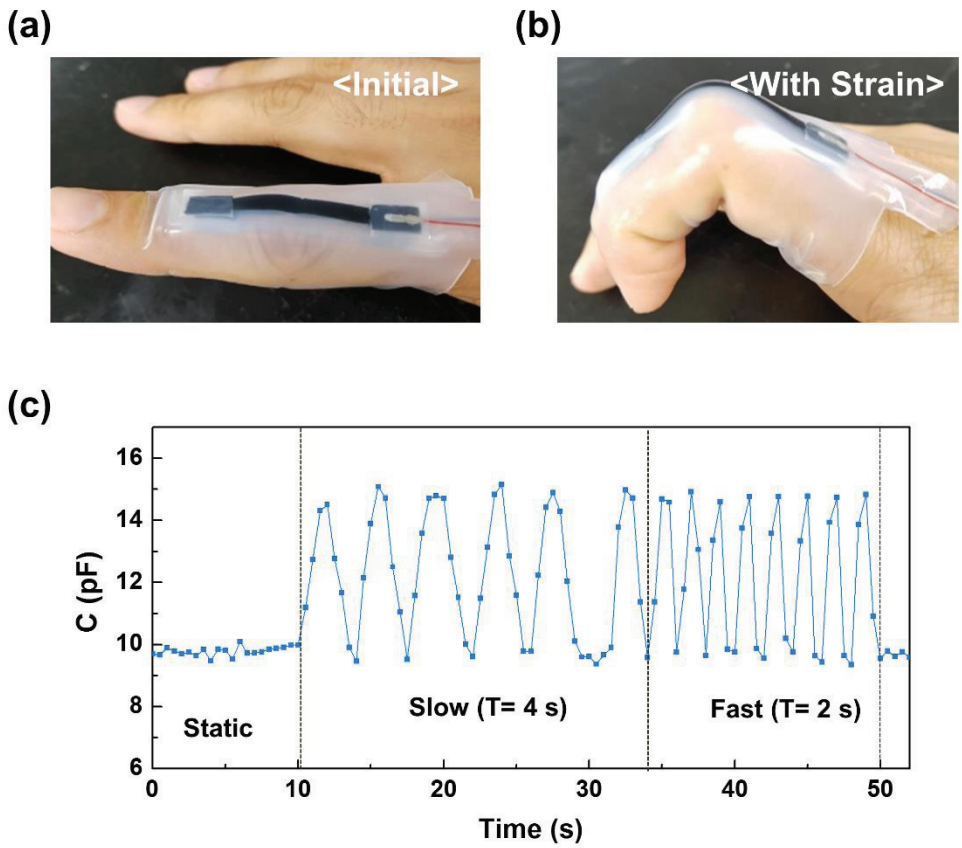

Figure 3.9 (a), (b) The images of thin type gel-based strain sensors for epidermal applications. (c) The output characteristics of fabricated epidermal-type sensors with the finger motion.

3.5. Improvement of gauge factor of capacitive type stretchable strain sensors by using auxetic elastomer[3.15]

3.5.1. Deformation behavior of auxetic elastomer

The capacitive-type strain sensors have a merit for stable sensing performance compared to the resistive-type strain sensors due to their linear and non-hysteresis signal characteristics as well as mechanical durability. However, the use of conventional capacitive strain sensors are limited due to their low gauge factor as their strain-responsive mechanism only depends on the geometrical change of dielectric layer. Due to the isotropic property of dielectric elastomers, the terms of in-plane and out-of-plane deformation can be canceled ($\mathbf{1} + \epsilon_y = \mathbf{1} + \epsilon_z$), which was shown in **Eq. 2.3-5**, the gauge factor of devices is restricted to 1.

To overcome the fundamental limitation of the capacitive type strain sensor, we introduce the composite elastomers, which called auxetic elastomers. Auxetic elastomers are composed of a re-entrant structured 2D scaffold elastomer embedded in a soft matrix elastomer (**Figure 3.10a**). Since the embedded stiff auxetic frame materials mainly affect the mechanical behavior of overall composites, the auxetic elastomers show an in-plane negative Poisson's ratio when stretched. Moreover, due to the volume conservation of soft matrix elastomers, the thickness of the auxetic elastomers can be decreased more severely than that of conventional elastomers during deformation (**Figure 3.10b, c**). By using an anisotropic mechanical behavior of auxetic elastomers as a dielectric layer of capacitive type strain sensors, the additional improvement of gauge factor of devices can be expected.

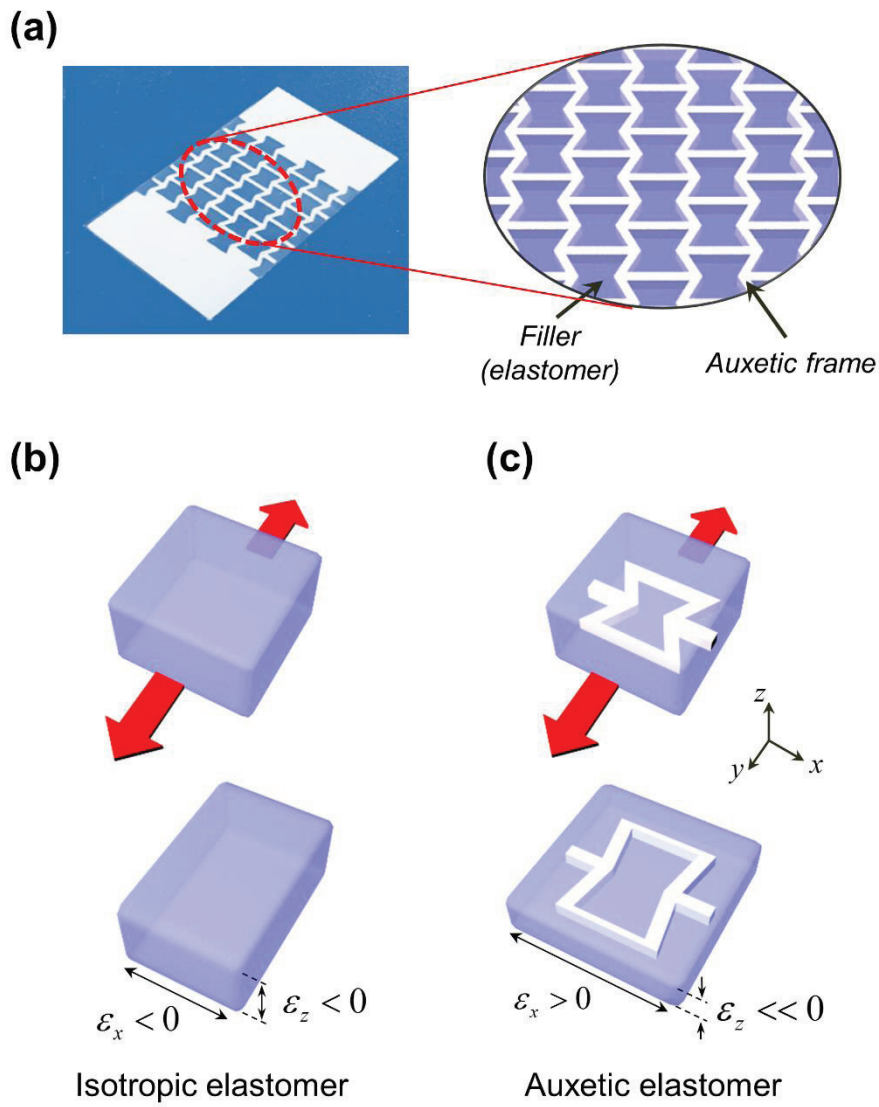

Figure 3.10 (a) Representative schematics of the auxetic elastomer composed of re-entrant structured auxetic frame filled by the soft elastomers. The deformation characteristics of the (b) pristine elastomer and (c) auxetic elastomer were shown.

For the fabrication of the auxetic elastomers, it is required to use an auxetic frame with a relatively higher modulus than that of the matrix elastomers. In this work, we chose a thermoplastic polyurethane (TPU) elastomer (7.5 MPa) as an auxetic frame material and embedded into Ecoflex™ 0010 matrix (0.006 MPa) (Details for fabrication methods are provided in **Section 3.2**). The geometry factor of auxetic frame was presented in **Figure 3.11a**.

To characterize the elastic behavior of an auxetic alstomer, uniaxial tensile test was performed. **Figure 3.11b and c** show the deformation morphologies of reference pristine Ecoflex™ sheets and auxetic elastomers after 20 % of stretch. As expected, the pristine Ecoflex™ sheet showed lateral shrinkage when stretched. On the other hand, the auxetic elastomers expanded in lateral direction during the stretch, which shows the characteristic behavior of an in plane negative Poisson's ratio.

Along with the morphology changes, we quantified the Poisson's ratio of auxetic elastomers by using an optical image analysis and calculating the ratio of the longitudinal and transverse strain from four reference points located in the middle of the tensile specimen. The thickness displacement u_z was measured by the instrumented depth-sensing technique (PI-85 SEM Picoindenter®; Hysitron). Since the auxetic elastomers exhibited anisotropic deformation, Poisson's ratio of the transverse and thickness directions should be considered separately as follows

$$v_{yx} = -\frac{\varepsilon_x}{\varepsilon_y}, \qquad v_{yz} = -\frac{\varepsilon_z}{\varepsilon_y} \qquad (\boldsymbol{Eq.3.2})$$

where the y-axis is the tensile direction and ε_x, ε_y, and ε_z are the strains in the x-, y-, and z- directions respectively. Considering the large deformability of elastomers, the Poisson's ratio was calculated by using Hencky's Poisson function, which is based on the true strain terms[3.16]. The true strain can be defined as

$$\varepsilon_i = \ln \frac{d_i}{d_{i,0}} \quad (i = x, y, z) \qquad (\boldsymbol{Eq.3.3})$$

where $d_{i,0}$ and d_i is the undeformed and the deformed unit scales in *i*-direction. The plot of ε_x and ε_y in **Figure 3.12a** shows the in-plane Poisson's ratio of pristine Ecoflex™ sheets and auxetic elastomers. Due to the lateral contraction during stretch, Poisson's ratio on the plane (v_{yx}) of pristine Ecoflex™ was measured to be 0.5. Meanwhile, the v_{yx} of auxetic elastomers was approximately -0.4, which indicates the lateral expansion by the structural opening of re-entrant auxetic frames.

Poisson's ratio in vertical direction (v_{yz}) of pristine Ecoflex™ sheet in the thickness direction can be measured to 0.5, which means that the isotropic property of conventional elastomers. Unlike pristine Ecoflex™, v_{yz} of auxetic elastomers was calculated to 0.7, indicating that auxetic elastomers showed 1.4 times larger thickness shrinkage compared to the pristine Ecoflex™ (**Figure 3.12b**). The negative Poisson's ratio behavior in a two-dimensional plane of auxetic elastomers induced the large thickness reduction at the same tensile level compared to conventional elastomers in order to keep the volume of matrix constant during deformation.

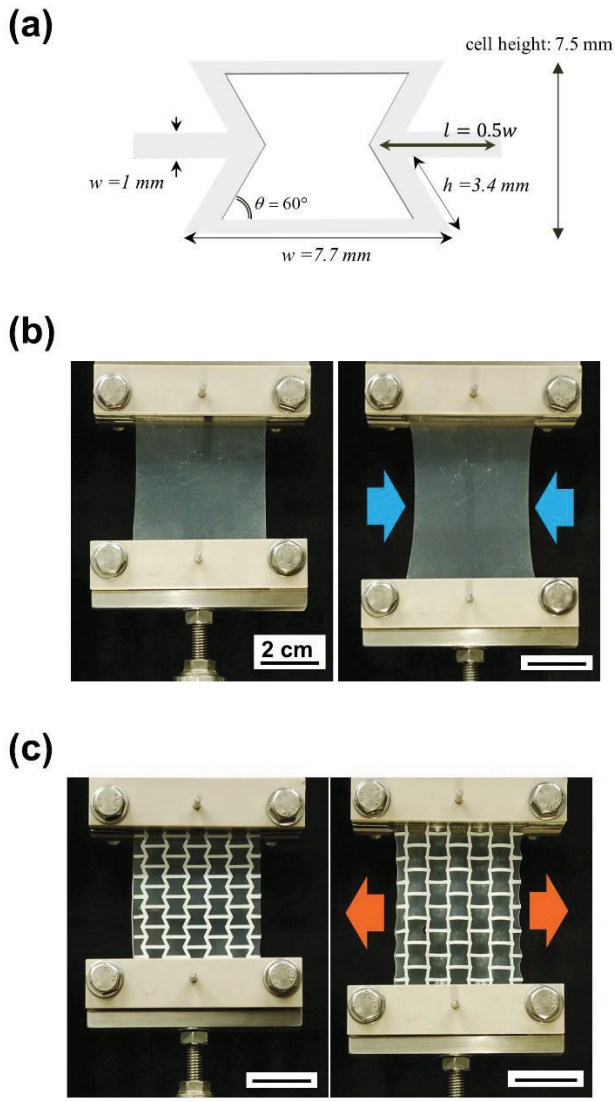

Figure 3.11 (a) The geometry of unit cell of re-entrant structured auxetic frame. The morphology of the pristine Ecoflex™ sheet and auxetic elastomer under 20 % stretch. Unlike Ecoflex™, the auxetic elastomers displayed lateral expansion when stretched.

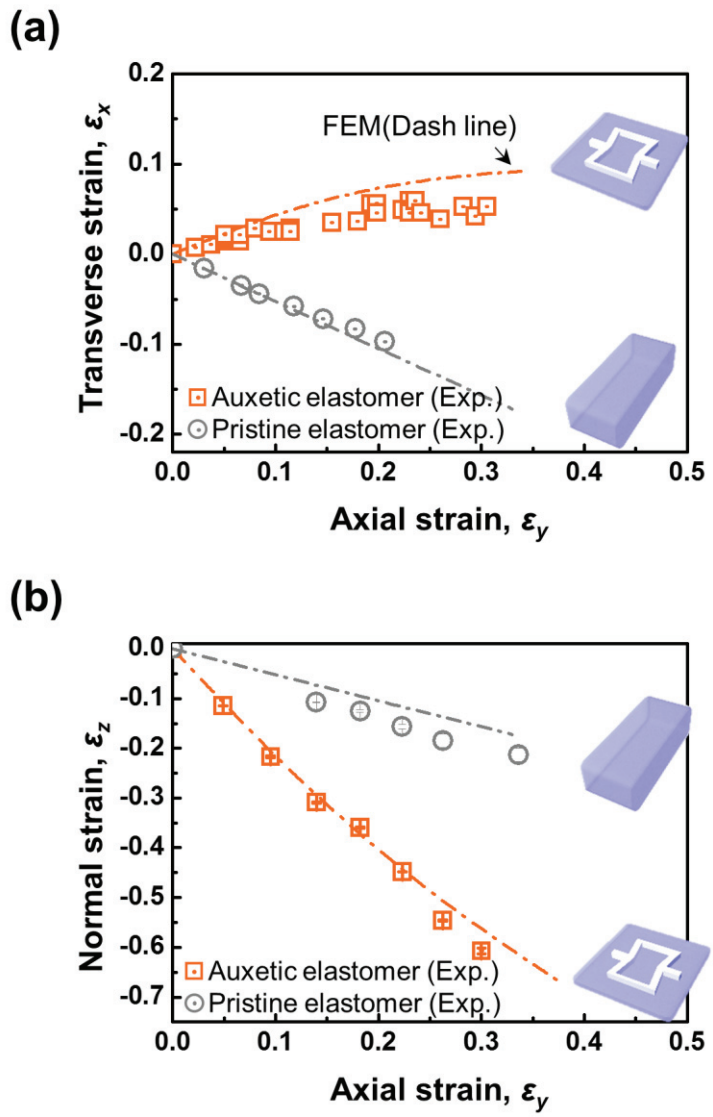

Figure 3.12 (a) Transverse strain curve and (b) normal strain curve versus axial strain of Ecoflex™ sheets and auxetic elastomers. The same sign of axial strain and transverse strain indicates the negative Poisson's ratio of auxetic elastomers.

3.5.2. Application of auxetic elastomers to capacitive type strain sensor

Through the development of the auxetic elastomers, we have suggested a new type of structural materials with a negative in-plane Poisson's ratio and found that their elastic properties also can be modulated. Moreover, as the 2-dimensional auxetic components have an anisotropic deformation behavior under stretch, the area of auxetic elastomer layers can be increased due to the negative Poisson's effect and their thickness can be much reduced for the volume conservation. By using these unique mechanical characteristics, we introduced an auxetic elastomer as a dielectric layer of the capacitive type strain sensors to improve the gauge factor of devices.

The normalized capacitance changes of the auxetic strain sensors as a function of stretch were shown in **Figure 3.13**. Gauge factor, which is a parameter for showing the sensitivity of stretchable strain sensors, could be determined by the slope of the curve. The gauge factor of the pristine Ecoflex™ dielectric layer-based sensor was 1, which corresponds to the basic characteristics of capacitive type strain sensors. However, when the auxetic elastomers were incorporated to the dielectric layer, the capacitance of devices increased more steeply, which is well matched to the our previous results of deformation behavior of auxetic elastomers. The following gauge factor resulted in beyond 3, which is the unprecedented highest value among the capacitive type stretchable strain sensors. Interestingly, the linear output signal characteristics still remained even with the sharp capacitance change. It might be related to that the dominant thickness reduction occurs in a soft Ecoflex™ matrix rather than a rigid TPU frame.

Moreover, the fabricated stretchable strain sensors also exhibited an excellent mechanical reliability. The developed strain sensors could endure the repeated deformation up to 5,000

cycles under 30% strain, also showing the excellent behavior in terms of hysteresis and recovery (**Figure 3.14**).

Furthermore, the gauge factor of strain sensors can be further improved by considering the electrode coverage region. Since the auxetic elastomers are composed of Ecoflex™ filler and TPU frame with different dielectric constants, the capacitance should be calculated separately for each constituent material. The capacitance of auxetic elastomers can be considered as the parallel capacitor series of filler and frame materials and expressed as

$$C_{total} = C_{fill} + C_{aux} = \varepsilon_0 \varepsilon_{r,fill} \frac{A_{fill}}{d_{fill}} + \varepsilon_0 \varepsilon_{r,aux} \frac{A_{aux}}{d_{aux}} \qquad (\boldsymbol{Eq.3.4})$$

where A_{fill} and A_{aux} denotes the area of filler and auxetic frame, and d_{fill}, d_{aux} denotes the thickness of filler and auxetic frame. **Figure 3.15 a and b** show the dimensional changes of Ecoflex™ filler and TPU frame obtained by finite element method simulations using the ABAQUS CAE software. We found that the Ecoflex™, which is the filler material of auxetic elastomer, showed significant areal and thickness change compared to the TPU. Therefore, additional improvement of gauge factor of devices can be achieved up to 3.96 by placing the gel electrodes within the expanded unit cell of auxetic frame (**Figure 3.15c,d**).

Lastly, the developed sensors were applied to the skin-mountable wearable devices for detecting elbow motion (**Figure 3.16a**). Due to the negative Poisson's ratio characteristics, the developed sensor can form a conformal contact on the non-Gaussian plane. The normalized capacitance change of the auxetic elastomer based strain sensor with the elbow motion was presented in **Figure 3.16b**. The output signal change of auxetic elastomer based strain sensors (solid circles) were three times stronger that of the conventional strain sensors (open circles) during the bending of elbow without any other degradations of devices.

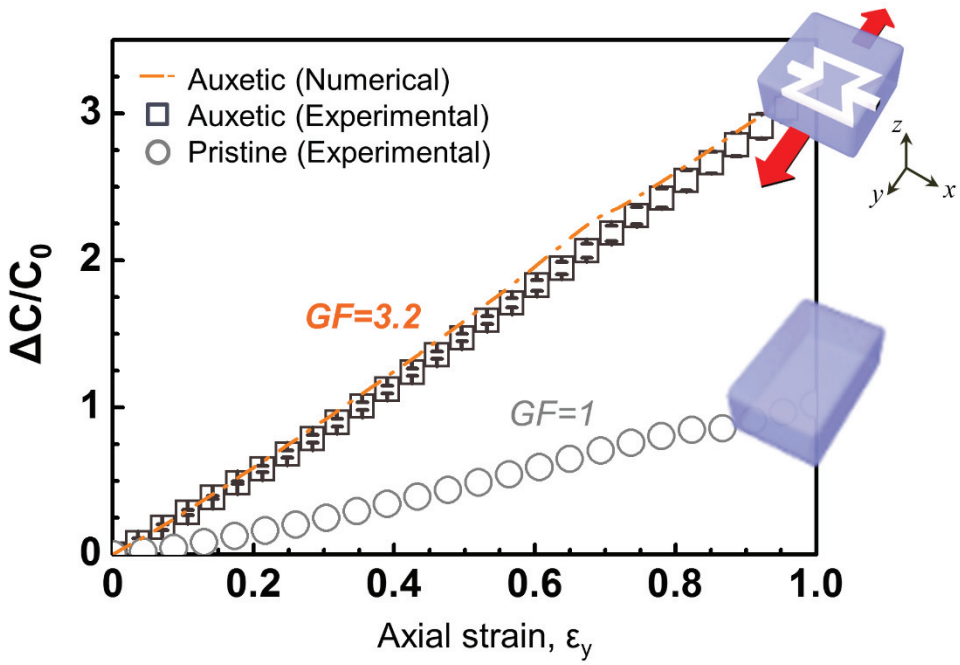

Figure 3.13 The normalized capacitance change of strain sensor under stretch. Both pristine Ecoflex™ dielectric and auxetic elastomer dielectric based strain sensors showed linear relationship between stretch and normalized capacitance.

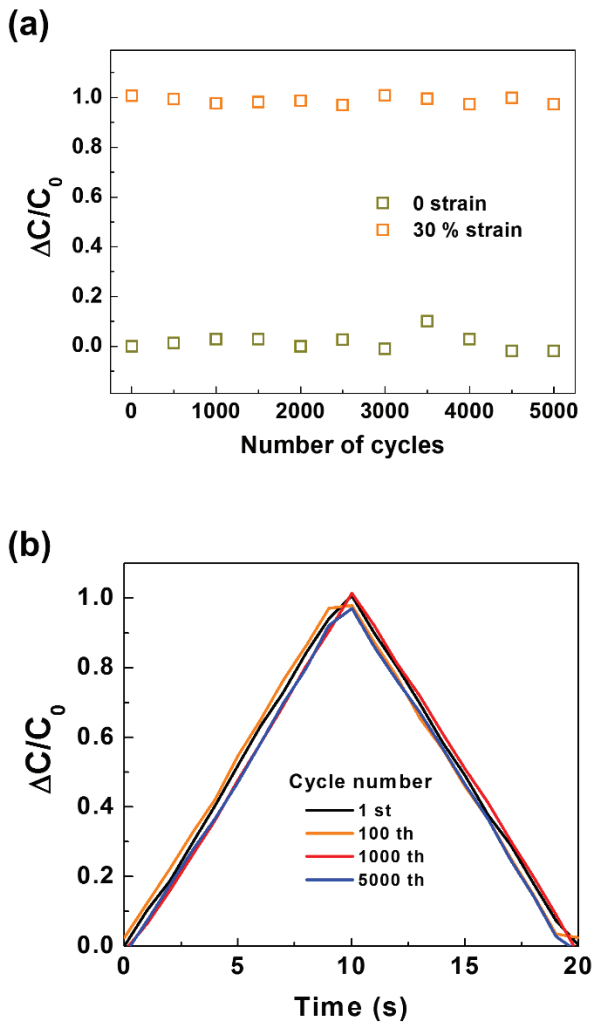

Figure 3.14 (a) The change of output characteristics of auxetic elastomer based strain sensors during the repeated deformations with 30 % strain. (b) Response curve at the specific cycles during stretch and release.

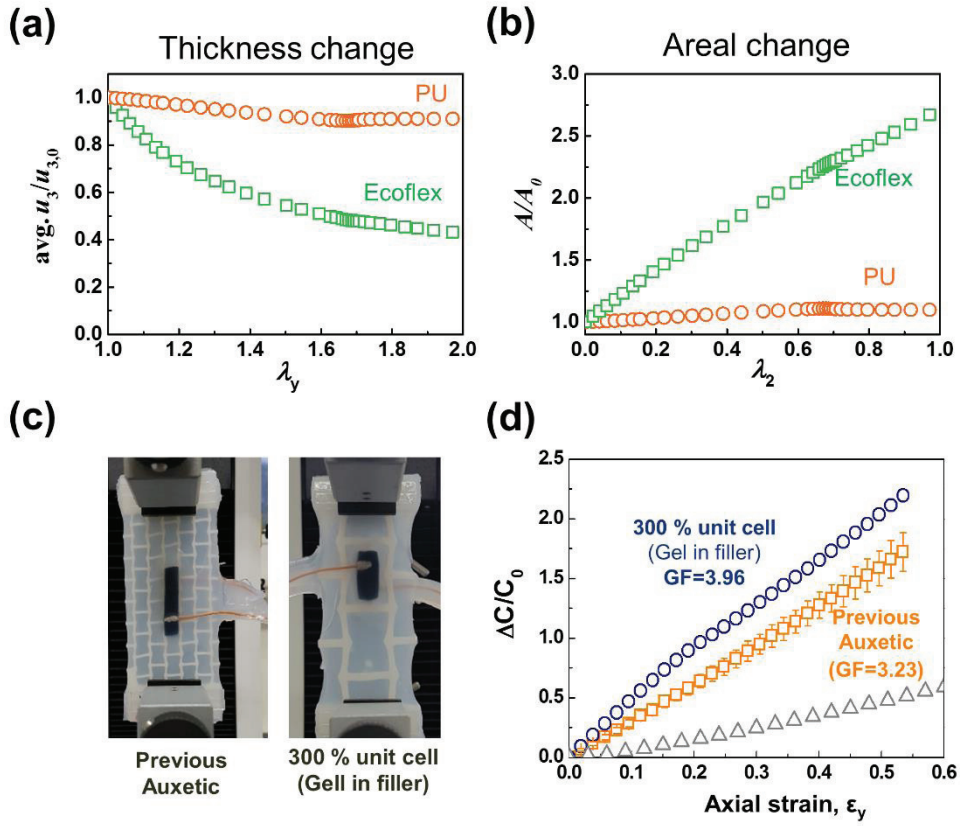

Figure 3.15 (a) Areal and (b) thickness change of Ecoflex™ filler and TPU frame in auxetic elastomers by using ABAQUS computational simulations. (c) The morphologies and (b) following output signal characteristics considering the placement of gel electrodes.

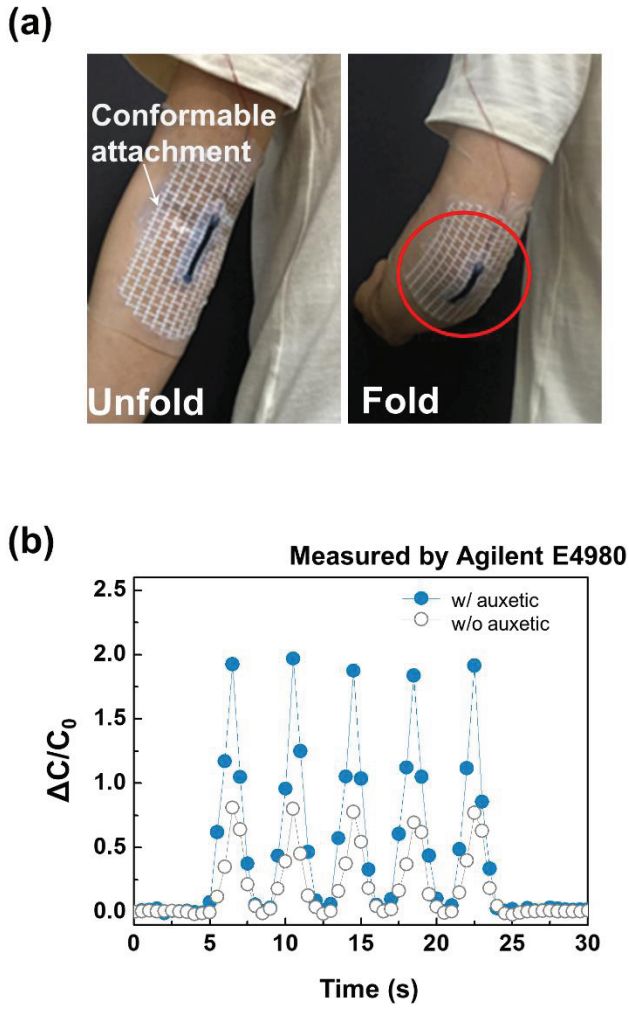

Figure 3.16 (a) Images showing conformable attachment of the an auxetic elastomer-based strain sensor on the elbow. (b) The output signal characteristics of strain sensors using conventional dielectric and auxetic dielectric layer. The signal intensity of sensors can be improved by introducing auxetic elastomers.

3.6. Summary

In this study, we developed a highly stretchable and reliable capacitive type strain sensor by introducing PEDOT:PSS based gel conductors as an electrode material and Ecoflex™ as a dielectric elastomer layer. Since PEDOT:PSS conductive gels have a high strechability with a strain insensitive property, the capacitance change behavior of fabricated devices can be detected under extreme deformation conditions, which is also well matched to the theoretical models. As all elements of the device are composed of inherently soft materials, it shows an excellent mechanical compliance when worn to skins and effective sensing of finger and elbow motion can be demonstrated.

Furthermore, we utilized auxetic elastomers as a soft dielectric material to enhance the sensing performance of capacitive type stretchable strain sensors. As the 2-dimensional auxetic elastomers have an anisotropic deformation behavior under stretch, the area of dielectric layers can be increased due to the negative Poisson's effect and the thickness of layers can be much reduced for the volume conservation, which leads to the improvement of gauge factor of the capacitance type strain sensors up to 3.2 fold. Moreover, a way to optimize the sensing performance of devices was suggested by using computational simulations. Our findings will be applicable to engineering wearable and skin-attachable devices and will stimulate researchers to extend other soft electronic devices in various directions.

References

[3.1] Amjadi, M., Pichitpajongkit, A., Lee, S., Ryu, S. & Park, I. Highly stretchable and sensitive strain sensor based on silver nanowire-elastomer nanocomposite. *ACS Nano* **8**, 5154-5163, doi:10.1021/nn501204t (2014).

[3.2] Trung, T. Q. & Lee, N. E. Recent Progress on Stretchable Electronic Devices with Intrinsically Stretchable Components. *Adv Mater* **29**, doi:10.1002/adma.201603167 (2017).

[3.3] Roh, E., Hwang, B. U., Kim, D., Kim, B. Y. & Lee, N. E. Stretchable, Transparent, Ultrasensitive, and Patchable Strain Sensor for Human-Machine Interfaces Comprising a Nanohybrid of Carbon Nanotubes and Conductive Elastomers. *ACS Nano* **9**, 6252-6261, doi:10.1021/acsnano.5b01613 (2015).

[3.4] Lim, S. *et al.* Transparent and Stretchable Interactive Human Machine Interface Based on Patterned Graphene Heterostructures. *Advanced Functional Materials* **25**, 375-383, doi:10.1002/adfm.201402987 (2015).

[3.5] Jeong, J. W. *et al.* Materials and optimized designs for human-machine interfaces via epidermal electronics. *Adv Mater* **25**, 6839-6846, doi:10.1002/adma.201301921 (2013).

[3.6] Shi, G. *et al.* Highly Sensitive, Wearable, Durable Strain Sensors and Stretchable Conductors Using Graphene/Silicon Rubber Composites. *Advanced Functional Materials* **26**, 7614-7625, doi:10.1002/adfm.201602619 (2016).

[3.7] Hur, J. *et al.* Polypyrrole/Agarose-based electronically conductive and reversibly restorable hydrogel. *ACS Nano* **8**, 10066-10076, doi:10.1021/nn502704g (2014).

[3.8] Green, R. A., Baek, S., Poole-Warren, L. A. & Martens, P. J. Conducting polymer-hydrogels for medical electrode applications. *Sci Technol Adv Mater* **11**, 014107,

doi:10.1088/1468-6996/11/1/014107 (2010).

[3.9] Lee, Y. Y. *et al.* A Strain-Insensitive Stretchable Electronic Conductor: PEDOT:PSS/Acrylamide Organogels. *Adv Mater* **28**, 1636-1643, doi:10.1002/adma.201504606 (2016).

[3.10] Choi, G. M. *et al.* PEDOT:PSS/Polyacrylamide Nanoweb: Highly Reliable Soft Conductors with Swelling Resistance. *ACS Appl Mater Interfaces* **11**, 10099-10107, doi:10.1021/acsami.9b00314 (2019).

[3.11] Chen, Y. S., Hsieh, G. W., Chen, S. P., Tseng, P. Y. & Wang, C. W. Zinc oxide nanowire-poly(methyl methacrylate) dielectric layers for polymer capacitive pressure sensors. *ACS Appl Mater Interfaces* **7**, 45-50, doi:10.1021/am505880f (2015).

[3.12] Gerratt, A. P., Michaud, H. O. & Lacour, S. P. Elastomeric Electronic Skin for Prosthetic Tactile Sensation. *Advanced Functional Materials* **25**, 2287-2295, doi:10.1002/adfm.201404365 (2015).

[3.13] Tee, B. C. K. *et al.* Tunable Flexible Pressure Sensors using Microstructured Elastomer Geometries for Intuitive Electronics. *Advanced Functional Materials* **24**, 5427-5434, doi:10.1002/adfm.201400712 (2014).

[3.14] Park, S. *et al.* Stretchable energy-harvesting tactile electronic skin capable of differentiating multiple mechanical stimuli modes. *Adv Mater* **26**, 7324-7332, doi:10.1002/adma.201402574 (2014).

[3.15] 이영주. Engineering the Deformation Characteristics of Soft Materials through Geometric Design of Auxetics for Flexible Electronics Application. (2017).

[3.16] Mihai, L. A. & Goriely, A. How to characterize a nonlinear elastic material? A review on nonlinear constitutive parameters in isotropic finite elasticity. *P Roy Soc a-Math Phy* **473**, doi:ARTN 2017060710.1098/rspa.2017.0607 (2017).

CHAPTER 4

Development of Open Junction Ionic Diode for Direct Ionic Signal Sensing[4.1]

4.1. Introduction

Beyond the wearable devices inspired by current stretchable electronics, more interactive devices are being incorporated into human bodies. In particular, the implementation of biointegrated devices[4.2-7] which can sense and transmit signals from biological systems has resulted in their use in a wide range of applications, such as monitoring neural[4.8-11] or cardiac[4.12,13] activities and delivering drugs[4.14-16] for medical care.

To date, biological signals have been acquired by electronic devices which are using metal electrodes[4.17,18] or conjugated electroactive polymers[4.19-21]. However, since the signals from a biological system are mainly based on transportation of ions (*i.e.*, K^+,

Ca^{2+}, neurotransmitters, etc), a fundamental mismatch of signal carriers between electrical devices and biological system has made direct communication persistently difficult due to the high impedance created at the interfaces[4.17,19]. Therefore, an ion-based signal sensing system which can directly interpret ion signals from a biological system is required to promote the human-machine interfaces (HMIs)[4.22-24].

Considering the abovementioned issues, hydrogels have been extensively studied as a promising candidate of ionic conductors[4.22,24-26] due to their inherent mechanical flexibility[4.16,27] and excellent biocompatibility[4.28,29]. Moreover, by introducing cross-linked polyelectrolyte gels[4.22,24] composed of fixed charges on their polymeric chains, it is possible to mimic the behavior of p-type or n-type semiconductors because only counter ions that are oppositely charged on the polyanionic or polycationic backbones are mobile due to Donnan exclusion. More recently, by combining different types of polyelectrolyte gels, the operation of ion p-n junction diodes[4.30-32] and transistors[4.33-35] has been demonstrated.

Despite the many advances in developing ionic devices, obtaining an ionic signal directly without changing signal carriers has remained problematic for the following reasons. In previously reported ionic devices, diodes or transistors were developed to be operated via an external electrical bias[4.20,23,36] with mimicking the functions of electrical semiconductor devices. For example, ionic transistors were successfully operated to transmit a signal by applying external voltages to the gate[4.35,37]. However, because the devices were designed for an external bias, it was very difficult to apply external ion signals to the devices. Moreover, as the transmittance of ionic signals is controlled by the gate voltage on an additional electrode[4.20,23,36], the cells in biological media can also be exposed to unwanted electrical stimulation when such electrodes are activated. Therefore, a new design is required to attract external ion signals to an ionic device.

Chapter 4: Development of Open Junction Ionic Diode for Direct Ionic Signal Sensing

In this study, we developed a method for direct sensing of ionic signals through the modified design of ionic devices. By designing a micro hole at the encapsulation layer of microfluidic chip-based polyelectrolyte gel diodes, which can be referred to as open junction ionic diodes (OJIDs), ionic signals from the external environment can be directly transmitted to active elements of ionic devices. Through the visualization of the ionic distribution after injecting fluorescent ions, we verified that ionic solutions can be well injected into the devices without loss. By investigating the changes in ionic currents through the electrochemical characterization, the mechanisms of ionic signal sensing in the OJIDs were suggested.

4.2. Experiments

4.2.1. Materials

All chemical reagents were used without further purification. 3-sulfopropyl acrylate potassium salt (SPA), 2-acrylamide-2-methyl-1-propanesulfonic acid (AMPSA), acrylamide (AAm), acrylic acid, styrene sulfonic acid (SS), vinylsulfonic acid (VSA), N-(3-(N,N-dimethylamino)propyl) acrylamide methyl chloride quarternary (DMAPAAQ), 2-(acryloyloxy ethyl)trimethyl ammonium chloride) (AETMAC) diallyldimethylammonium chloride (DADMAC), N'-methylenebisacrylamide (crosslinker, MBAAm), 3-(trimethoxysilyl)propyl metha-crylate (TMSMA), methanol, acetic acid, fluorescein sodium salt, rhodamine 6G, sodium chloride, potassium chloride, sodium chloride and lithium chloride were purchased from Aldrich. Lithium phenyl-2,4,6-trimethylbenzoylphosphinate (LAP) photoinitiator and Ag/AgCl electrodes were purchased from Tokyo Chemical Industry and CHI Instruments, respectively.

4.2.2. Measurement of ionic transport properties in polyelectrolyte gels

To characterize the ion conductive and selective properties in polyelectrolyte gels, a salt bridge model[4.38,39] was introduced for the test module. Representative schematics of the salt bridge model are shown in **Figure 4.1**. To concentrate the voltage drops applied to the polyelectrolyte gels rather than the reservoir regions, the polyelectrolyte gels were filled in capillary glass tubes (inner diameter: 0.8 mm, length: 5 cm, Omega glass) by photopolymerization and connected to both sides of the reservoir. After

forming electrochemical contact with the Ag/AgCl electrode, the current-voltage *I-V* sweep characteristics of the polyelectrolyte gels were measured by a multichannel potentiostat (ZIVE MP2A, Wonatech).

4.2.3. Fabrication of microfluidic chips with open structure

Figure 4.2 shows the fabrication process of microfluidic chip-based OJIDs. To design the open junction structure for the injection of an ionic solution into the channel of the microfluidic chip, a microhole was formed at the p-n junction interface by laser hole drilling (KOS-SF1000RBS picosecond UV laser system, KORtherm Science), and openings for the reservoir were formed in the encapsulation glass layer (D263 ultrathin glass (=30 μm), Schott). The channels in the glass substrate were patterned using photolithography and a wet etching process following a previously reported procedure. Soda lime glass slides of hydrolytic class 3 with a thickness of 1 mm (Marienfeld) were used as substrates. After being cleaned with a piranha solution (H_2SO_4: H_2O = 3:1, J. T. Baker) to remove organic residues from the surfaces, the glass slides were rinsed with deionized (DI) water and then dehydrated on a hot plate at 175 °C for 10 min. The cleaned glass substrates were spin-coated (ACE-200, DongAh Trade Corp.) with hexamethyl-disilazane (HMDS, Clariant) and AZ4620 photoresist (PR, Clariant), and soft baking was performed at 110 °C and 100 °C for 1 min 30 s. After alignment with a channel-patterned mask, the PR layer was exposed to UV light with an intensity of 21 $mWcm^{-2}$ for 20 s (MDE-4000, Midas) and then developed with an AZ 400 K developer (Clariant) for 1 min 30 s. The PR-patterned glasses were annealed on a hot plate at 180 °C for 15 min for hard baking and then etched with a 6:1 buffered oxide etch

solution (J. T Baker). As the rate of glass etching was confirmed to be 0.8 μm/min, channels in the glass with a highly uniform depth of 50 μm depth could be achieved. After alignment of the microholes in D263 glass and the center of the channel in patterned slide glass, the two glass surfaces were thermally bonded (595 °C for 18 h) under a 200 g load for encapsulation.

4.2.4. Formation of ionic p-n junction in microfluidic chip

To form a polyelectrolyte gel-based junction in the microfluidic chip, the channel was treated with a mixture of TMSMA, acetic acid and methanol (the ratio of the solution mixture was 1:2:2) for 1 h to enable stable adhesion between the polyelectrolyte gel and glass and then cleaned with methanol. After treatment, the whole channels in a microchip were filled with the precursor solution of the pDADMAC gel by using micropipette. The channel in the microfluidic chip was aligned with the photomask and exposed to UV light with an intensity of 21 $mWcm^{-2}$ for 2.5 s (MDE-4000, Midas) and then the uncured precursor solution was removed through the suction tube. Subsequently, photopolymerization of the pSPA gel was performed using the same method, except that the exposure time under UV light was 3 s. As the both pDADMAC and pSPA precursor solutions includes the same initiator and crosslinker, the pSPA gel was well formed adjacent to the pDADMAC gel through the sequential photo-polymerization without generating gaps at junction. (Detailed information for sequential patterning process used in OJIDs was presented in **Figure 4.3**) After being washed with KCl solution several times, the fabricated ionic diodes were stored in 0.1 M KCl solution for over 1 day before characterization.

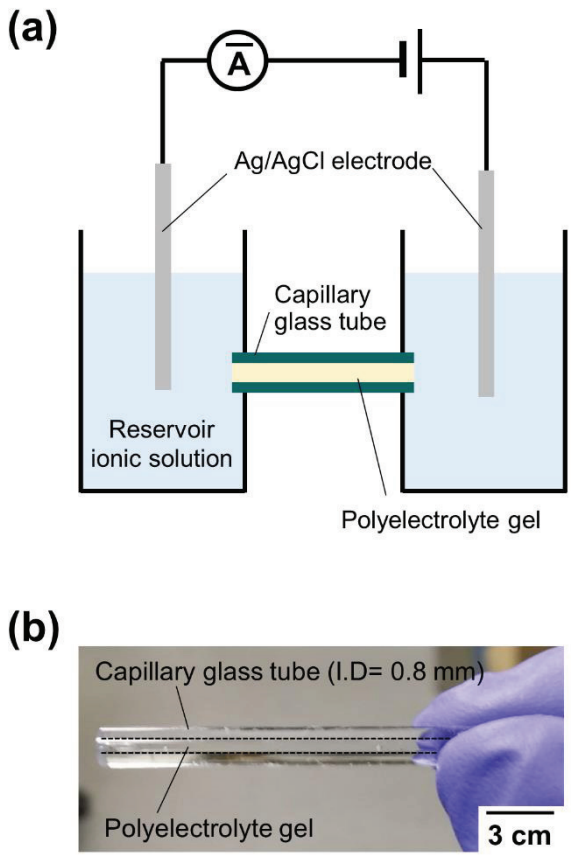

Figure 4.1 (a) Scheme of the salt bridge model for measuring the ion conductivity of polyelectrolyte gels. (b) Image of polyelectrolyte gel formed in capillary glass tube.

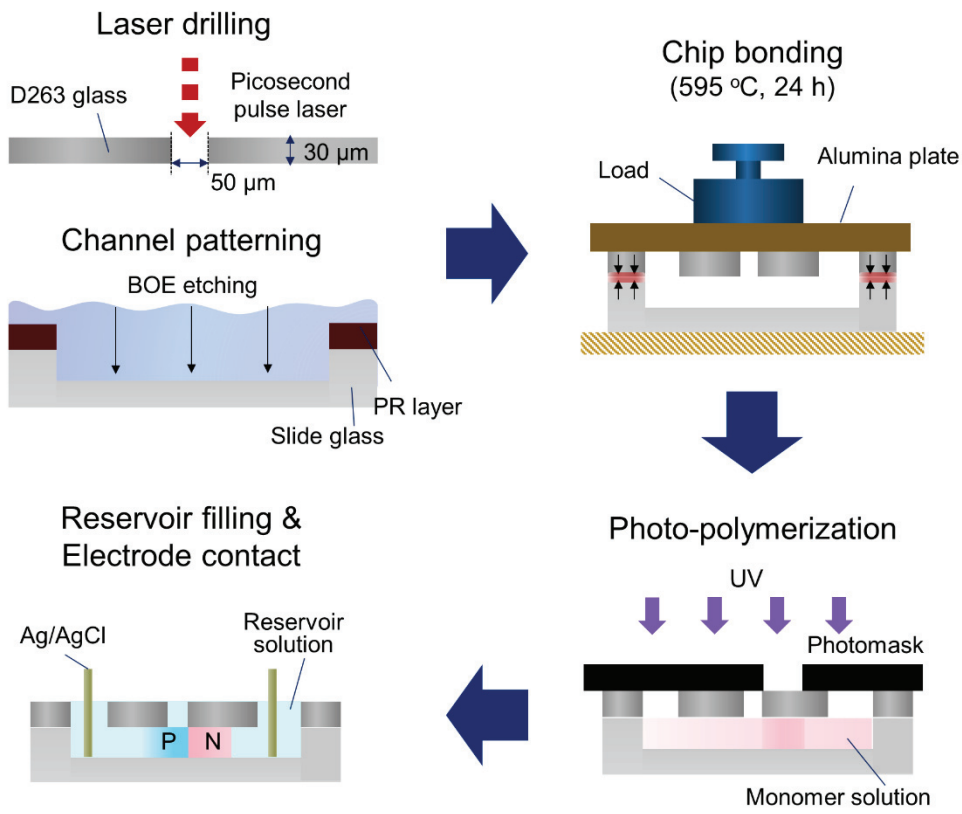

Figure 4.2 Fabrication process of an OJID in a microfluidic chip. By introducing thin glass (~30 μm) as an encapsulation layer, an ion-injectable microhole can be patterned on the devices.

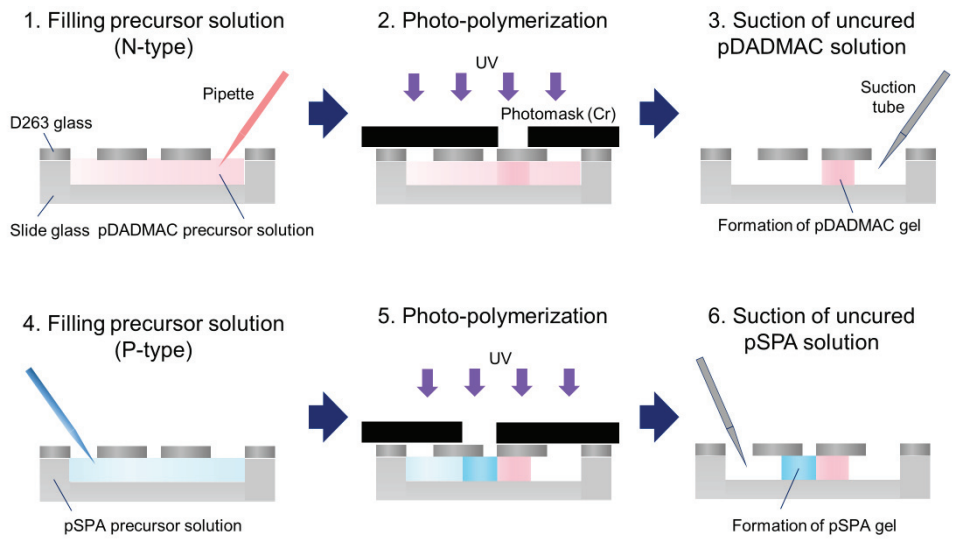

Figure 4.3 Schematic illustrating the photo-polymerization process. After forming pDADMAC gels in channels, the uncured precursor solution was removed through a suction tube, and then, the pSPA gels were patterned next to the pDADMAC gel.

4.3. Characterization of ionic transport properties in poly-electrolyte gels for device application

To select the polyelectrolyte gels as ionic active materials for ionic diodes, their ionic transport properties were characterized by using a salt bridge test model, which was introduced in **Section 4.2.2** and **Figure 4.1**. As a candidate of the constituent materials for device application, various polyanionic (p-type) and polycationic (n-type) hydrogels were synthesized (**Figure 4.4**). To control the concentration of the fixed charges in polyelectrolyte gels, the monomer concentration in precursor solutions was fixed to 2 M and polymerized by using the same crosslinker (MBAAm) and photoinitiator (LAP).

For the evaluation criteria of the ionic transport properties of polyelectrolyte gels, ion conductivity and ion selectivity were suggested (**Figure 4.5**). The ion conductivity refers to the degree of movement of ions within gels due to the electrical field, which determines the speed of devices. After measuring the slope of the *I-V* characteristics through the salt bridge test module, the ion conductivity of polyelectrolyte gels was calculated by considering the dimension of the polyelectrolyte gels in the capillary glass tube (**Figure 4.6a, c**). In addition, ion selectivity refers to the degree of charge-selective ionic transportation, which can be related to the rectification property of ionic pn junction diodes. In this work, the ion selectivity parameter was determined by comparing open circuit voltages (OCVs) between the two reservoirs with different concentration (0.1 M and 0.01 M) of KCl ionic solutions (**Figure 4.6b, d**). According to the Nernst equation, theoretical values of OCV can be expressed as

$$\Delta \mathbf{E} = \frac{\boldsymbol{RT}}{\boldsymbol{nF}} \ln \frac{\boldsymbol{C_1}}{\boldsymbol{C_2}} \qquad (\boldsymbol{Eq.4.1})$$

where R is the universal gas constant (8.314 $J \cdot K^{-1}mol^{-1}$), T is the temperature (~298 K), n is the charge valence number and F is the Faraday constant (96485 $C \cdot mol^{-1}$), respectively. If a polyelectrolyte gel have an ideal ion-selective property, the theoretical value of OCV can be calculated to 59 mV since only counter ions which are oppositely charged on the polymeric chains are mobile. However, in case of the real polyelectrolyte gels, some of the co-ions can transport into the gels, which leads to the decrease of OCV less than 59 mV[4.39]. In this study, we evaluate the ion selectivity of polyelectrolyte gels by comparison of OCVs between the theoretical value (59 mV) and the measured results.

Figure 4.7 shows the measured ion conductivities and OCVs of various poly-electrolyte gels. As a result of the characterization of p-type polyelectrolyte gels, pSPA gels, which are based on K^+ ions, exhibited excellent performances in terms of both ion conductivity and selectivity, indicating that they could be suitable for practical applications. Among the Na^+ ion-based p-type polyelectrolyte gels, pVSA gels show high ion conductivities and their OCV was close to that of the theoretical value (**Figure 4.7a**). In case of n-type polyelectrolyte gels, pDADMAC gels show the highest ion conductivities compared to the other materials, while the pDMAPAAQ gels have a merit for ion selective properties (**Figure 4.7b**). In this study, we select the pSPA and pDADMAC gels for the p-type and n-type gels for the application to ionic diodes considering the both ion conductive and selective performance.

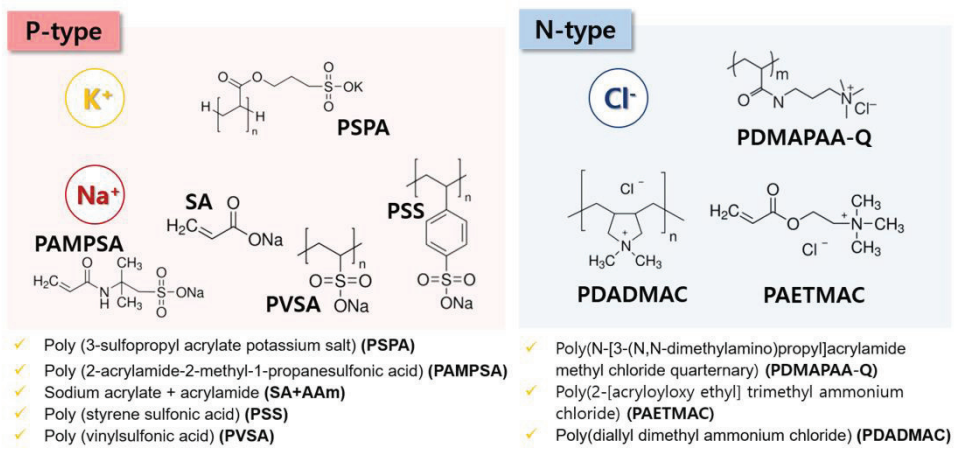

Figure 4.4 The formula and chemical structures of p-type and n-type polyelectrolyte gels characterized in this study.

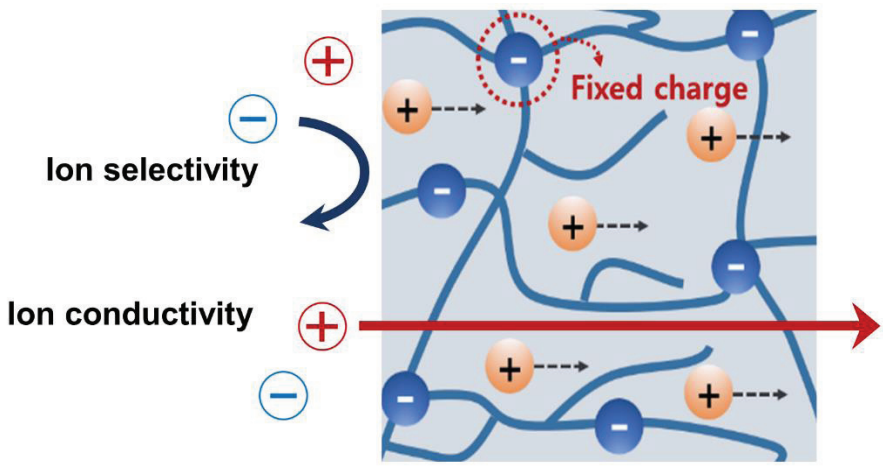

Figure 4.5 Illustrations for showing the ionic transport properties of polyelectrolyte gels. The ion conductivity of mobile ion and ion selectivity against the co-ions are the key parameters for characterizing the ionic transport properties of polyelectrolyte gels.

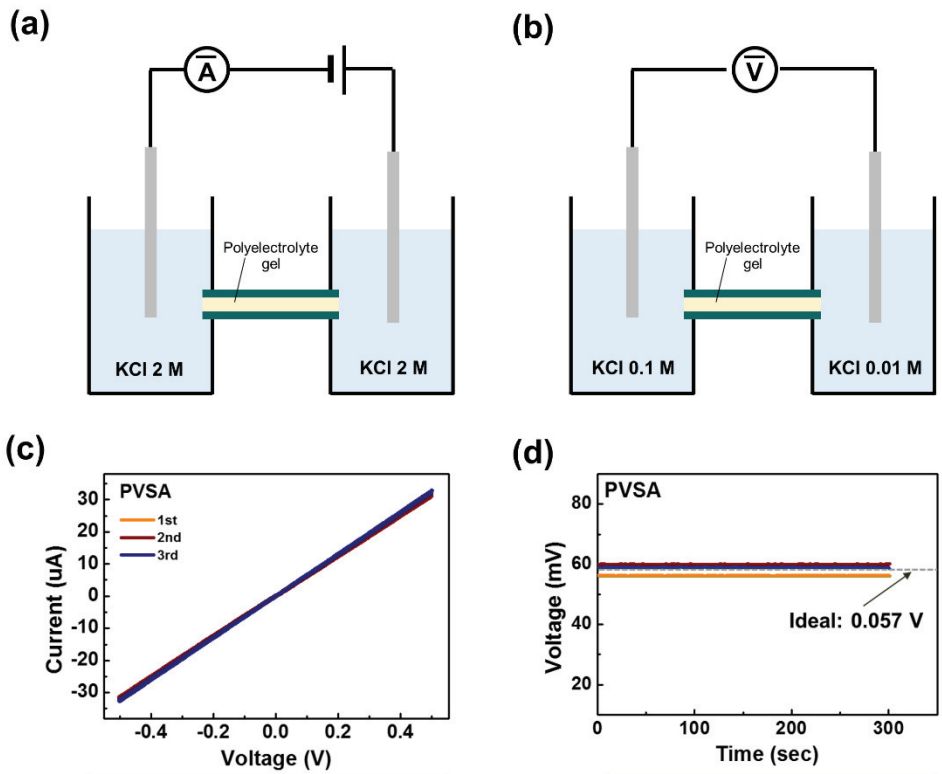

Sample #	Conductivity (Ω^{-1} cm^{-1})
1st	6.305 ± 0.060 X 10^{-2}
2nd	6.261 ± 0.067 X 10^{-2}
3rd	6.444 ± 0.066X 10^{-2}

Sample #	OCV (mV)
1st	56.23
2nd	59.98
3rd	58.92

Figure 4.6 The test modules for measuring (a) ion conductivity and (b) ion selectivity of polyelectrolyte gels by using salt bridge model. (c) *I-V* sweep characteristics and (d) OCVs of pVSA gels (p-type) were presented for example.

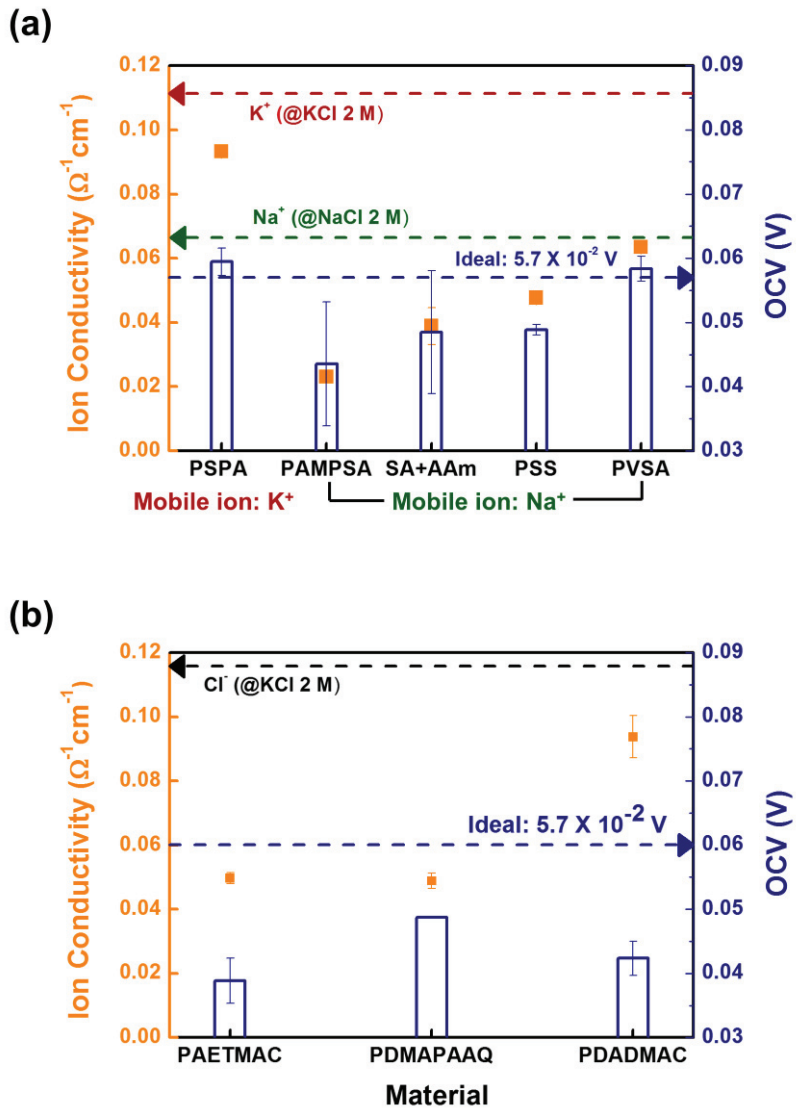

Figure 4.7 Measured ion conductivity and selectivity values of (a) p-type and (b) n-type polyelectrolyte gels.

4.4. Design of open junction ionic diode (OJID)

4.4.1. Fabrication of OJID and device configuration for ion injection

The representative architecture of OJIDs is illustrated in **Figure 4.8**. By introducing D263 ultrathin borosilicate glass (~30 μm, SCHOTT) as an encapsulation layer of microfluidic channels, which is amenable to laser hole drilling, an ion-injectable microhole (d~ 50 μm) could be formed and aligned with the p-n junction interface (**Figure 4.9**). After fabricating microfluidic glass chips, n-type poly(diallyl-dimethyl-ammonium chloride) (pDADMAC) and p-type poly(3-sulfopropyl acrylate potassium salt) (pSPA) polyelectrolyte gels were sequentially patterned on the microfluidic chip by UV photopolymerization. Due to the surface tension of the gel precursor solutions and mechanical instability of cured gels during suction, it is hard to form a gel in a half region of hole in the devices. In this study, we form the pDADMAC gel in the outer region of hole firstly and fill the other region including the hole with the pSPA gel. Subsequently, channels in the microfluidic chip were filled with reservoir ionic solution for the dialysis of polyelectrolyte gels and the formation of electrochemical contact. To apply a reverse bias to the OJIDs and measure the responsive ionic current signal without potential loss, nonpolarizable Ag/AgCl electrodes were connected to both sides of the reservoir.

Before ion injection, the *I-V* sweep characteristics of the devices were measured to confirm the rectification behavior of the OJIDs. **Figure 4.10** shows the representative *I-V* sweep curves of an OJID. The range of the voltage sweep was from –2 V to 2 V, and the scan rate was set to 25 mV/s. After a reverse voltage scan, the rectification of the

ionic current was commonly observed with hysteresis behavior, which was caused by the depletion of ions as previously reported[4.40]. The rectification ratio of devices (at ±2 V) was measured to around 10.

For ion injection, a picoliter microinjector (Warner instruments) was used to deliver ions locally to the microhole region (**Figure 4.11**). The microinjection needle was produced by pulling glass capillaries (GC100-10, Harvard Apparatus) with a dual-stage glass micropipette puller (PC-10, Narishige). In this work, the operation temperature at each stage was set to 85 °C and 80 °C, which results in an inner diameter of needle tip around 2.5 μm. To protect the tip of the microinjection needle during filling, which is vulnerable to high pressure, ionic solutions were back-filled by inserting a nonmetallic microsyringe (Microfil, World Precision Instruments) into the microinjection needles. By modulating injection parameters such as the injection pressure and time, as well as the inner diameter of the microneedle, the diameter of the injected ionic solution droplets was precisely controlled (inset of **Figure 4.11a**), and the amount of charge in the ionic input signal could also be quantified.

4.4.2. Visualization of ionic distribution after ion injection

To confirm whether both the positive and negative ions were injected into the OJIDs through the microhole, fluorescent ions[4.31] were injected into the devices to visualize the distribution of injected ions. **Figure 4.12a and b** shows fluorescence microscopy images of the ionic distribution of Rhodamine 6G cations (green) and fluorescein salt anions (red) after ion injection. Because the injected cationic and anionic fluorescent dyes were detected in the pSPA (p-type) and pDADMAC (n-type) regions, respectively, we verified that both the cations and anions were well injected into devices.

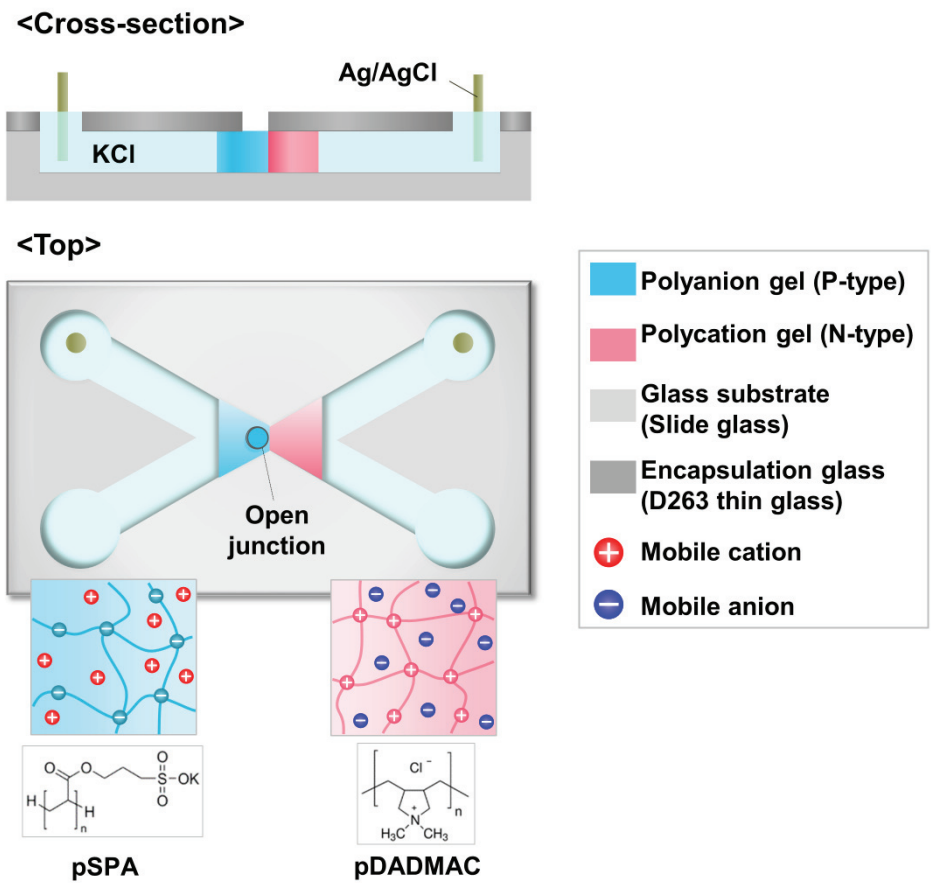

Figure 4.8 Schematic representation of an OJID. Through the ion-injectable hole structure formed on the polyelectrolyte gel region, ionic signals can be directly transmitted to the active element of devices.

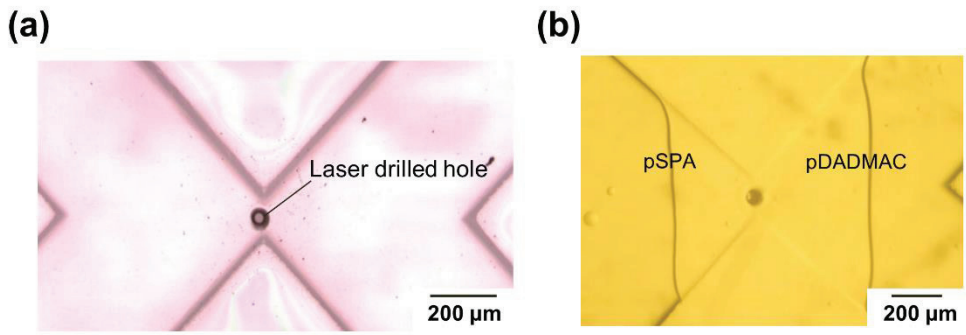

Figure 4.9 Images of microfluidic chips after (a) thermal bonding of the encapsulation layer and (b) photo-polymerization of the polyelectrolyte gel. The laser-drilled microhole was aligned with the intersection of the channel, and the polyelectrolyte gel on both sides was well formed in the OJIDs.

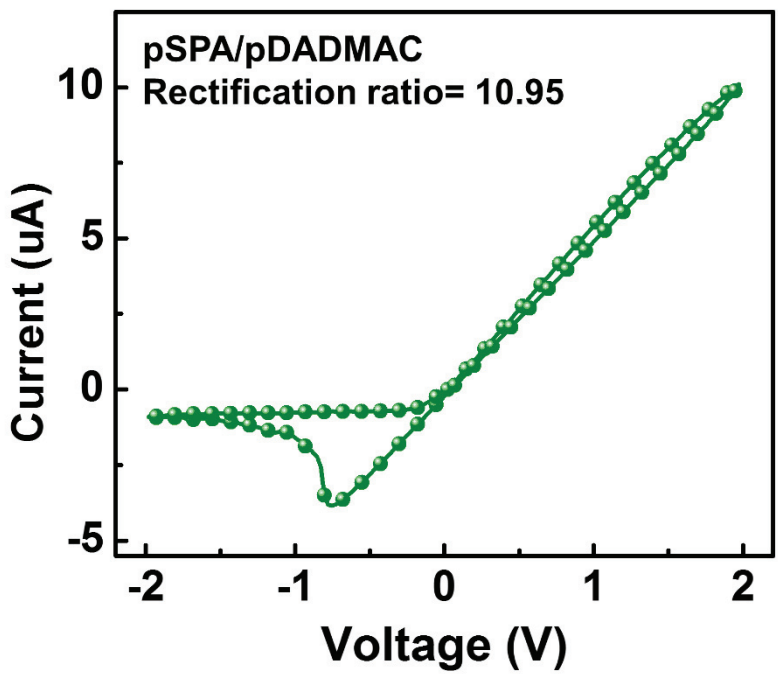

Figure 4.10 Representative *I-V* sweep curve of an OJID based on ionic junction between pSPA/pDADMAC polyelectrolyte gels.

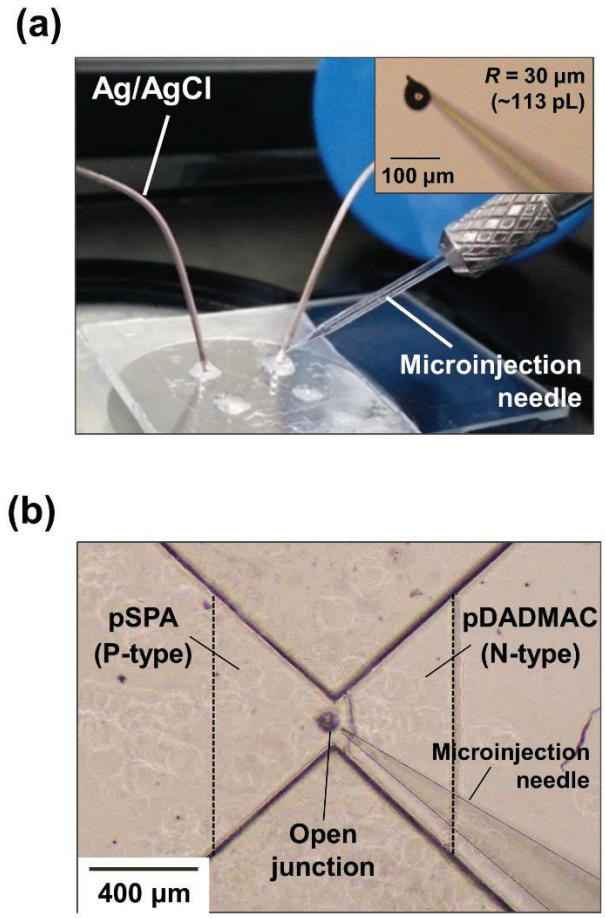

Figure 4.11 (a) Device configuration for ion injection. The volume of injected ionic solution was precisely controlled using a picoliter injector. Nonpolarizable Ag/AgCl electrodes were connected to the reservoir for in situ current measurement upon ion injection. (b) Microscopic images of open junction ionic diode before ion injection.

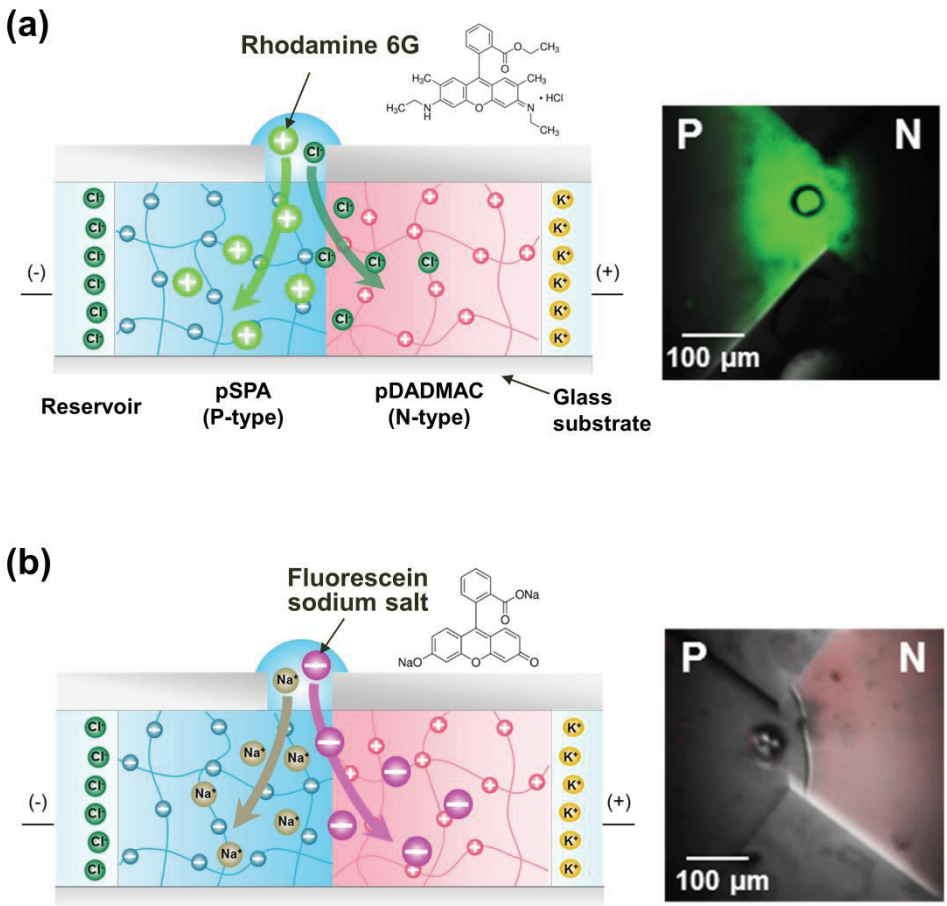

Figure 4.12 Schematic illustrations and fluorescence images indicating how the distribution of injected ions is monitored. (a) After the injection of the Rhodamine 6G fluorescent cations, most of the green fluorescence was observed in the pSPA region. (b) The injected fluorescent sodium salt anions were observed in the pDADMAC region, indicating ion injection into the devices through the open junction.

4.5. Ionic signal detection through OJID

The suggested mechanism of ionic signal detection through the OJIDs is presented in **Figure 4.13**. Initially, when the reverse bias voltages are applied to the OJIDs, mobile counter ions in polyelectrolyte gels are depleted and co-ions in reservoir cannot transported to the diodes due to the repulsive force with the fixed charges in polyelectrolyte chains, which leads to only small leakage currents in devices (**Figure 4.13a, b**). Then, in case that the minute ionic solutions are injected into the depleted state of OJID, ionic signals can be followed by the reverse current peak (**Figure 4.13c, d**).

To verify our suggested mechanism, we conducted the *in-situ* measurement of the ionic currents in OJIDs after ion injection. The amount of the injected ionic solution was fixed to KCl 0.01 M for 113 pL (Q~ 216 nC) and the concentration of KCl reservoir solution and applied reverse bias voltage were set to 0.01 M and -0.5 V, respectively. As the ionic solutions are injected into the opening of OJID after formation of sufficient depletion state in the ionic diode (-1 V for 3 min), the generation of the ionic current peak was observed (**Figure 4.14**). This result clearly shows that the minute ionic signal were well detected by using OJIDs.

Furthermore, the interesting point can be found by quantitative analysis of the responsive ionic signals. Through the integration of ionic current peak in the *i-t* curve, the detected charge amount was calculated to about 307 nC, which was even larger than that of injected ionic solutions. These findings indicate that the additional amplification phenomenon can occur in OJIDs as well as the sensing of the injected ion signal. In the next chapter, the ionic signal amplification effect in OJIDs will be discussed through the various case studies.

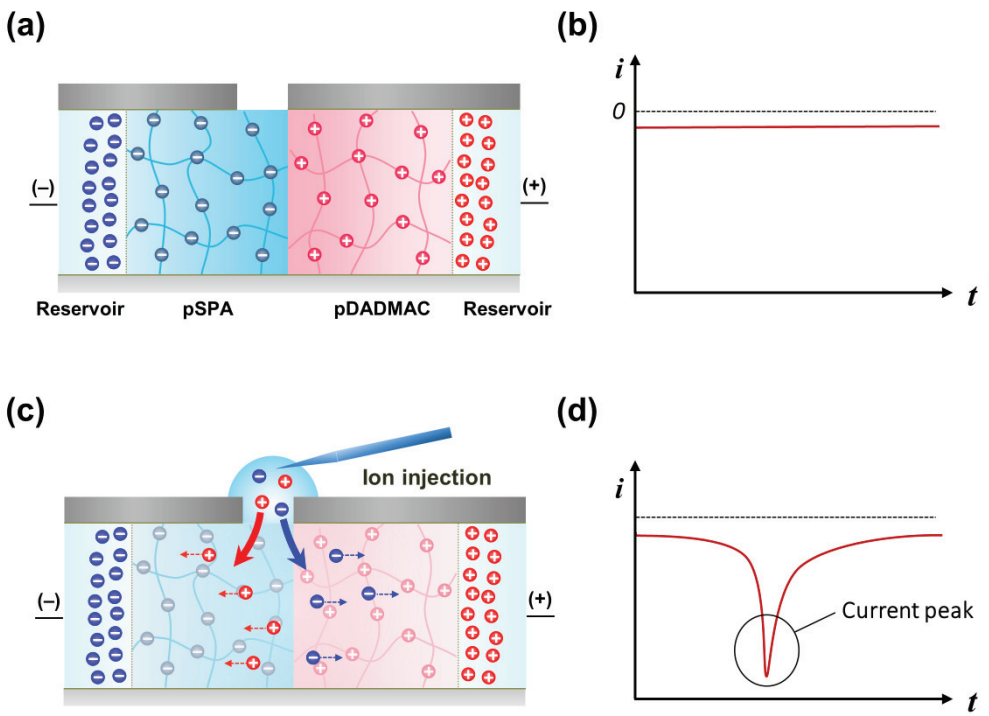

Figure 4.13 Schematics showing the expected behavior of ionic signal detection through an OJID. (a), (b) In the reverse biased state of devices, mobile counter ions in polyelectrolyte gels are depleted and only small leakage current can be measured. (c), (d) Through the ion injection to the open junction structure, ionic signals from external environment can be directly transmitted to active elements of devices and also detected by the ionic current peak.

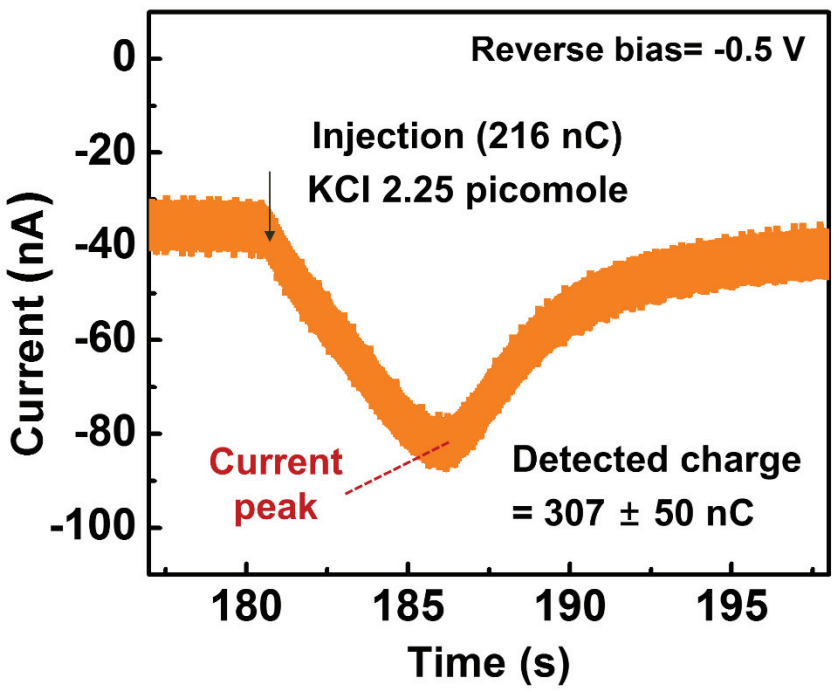

Figure 4.14 The change of ionic currents in the OJID during ion injection through the open structure of devices. The minute ionic signals can be detected in the form of reverse current peak.

4.6. Summary

In this chapter, we demonstrated the ionic signal sensing devices based on the inherent features in the ionic systems. By designing the ion injectable structure in microfluidic chip based ionic diodes, direct communications between ionic input signal and ionic devices were facilitated without the gate bias in medium. When the ionic solution is injected into the depletion state of ionic diodes, it can be observed by the form of ionic current peak. Furthermore, the possibility of the ionic signal amplification was found by electrochemical measurement, which will be discussed in the next chapter with the systematic case studies. We believe that our findings can point to future opportunities in ion-based signal processing devices such as ionic signal transmitters and converters as well as intimate communications with biological signals.

References

[4.1] Lim, S.-M. *et al.* Ion-to-ion amplification through an open junction ionic diode. *Proc Natl Acad Sci U S A,* online published, doi: 10.1073/pnas.1903900116 (2019).

[4.2] Kaltenbrunner, M. *et al.* An ultra-lightweight design for imperceptible plastic electronics. *Nature* **499**, 458-463, doi:10.1038/nature12314 (2013).

[4.3] Hammock, M. L., Chortos, A., Tee, B. C., Tok, J. B. & Bao, Z. 25th anniversary article: The evolution of electronic skin (e-skin): a brief history, design considerations, and recent progress. *Adv Mater* **25**, 5997-6038, doi:10.1002/adma.201302240 (2013).

[4.4] Kim, D. H. *et al.* Stretchable and foldable silicon integrated circuits. *Science* **320**, 507-511, doi:10.1126/science.1154367 (2008).

[4.5] Dagdeviren, C. *et al.* Conformal piezoelectric energy harvesting and storage from motions of the heart, lung, and diaphragm. *Proc Natl Acad Sci U S A* **111**, 1927-1932, doi:10.1073/pnas.1317233111 (2014).

[4.6] Kim, D. H., Ghaffari, R., Lu, N. & Rogers, J. A. Flexible and stretchable electronics for biointegrated devices. *Annu Rev Biomed Eng* **14**, 113-128, doi:10.1146/annurev-bioeng-071811-150018 (2012).

[4.7] Pang, C., Lee, C. & Suh, K. Y. Recent advances in flexible sensors for wearable and implantable devices. *Journal of Applied Polymer Science* **130**, 1429-1441, doi:10.1002/app.39461 (2013).

[4.8] Kim, D. H. *et al.* Dissolvable films of silk fibroin for ultrathin conformal bio-integrated electronics. *Nat Mater* **9**, 511-517, doi:10.1038/nmat2745 (2010).

[4.9] Viventi, J. *et al.* Flexible, foldable, actively multiplexed, high-density electrode array for mapping brain activity in vivo. *Nat Neurosci* **14**, 1599-1605, doi:10.1038/nn.2973 (2011).

[4.10] Sinha, N. *et al.* Predicting neurosurgical outcomes in focal epilepsy patients using computational modelling. *Brain* **140**, 319-332, doi:10.1093/brain/aww299 (2017).

[4.11] Kipke, D. R. *et al.* Advanced neurotechnologies for chronic neural interfaces: new horizons and clinical opportunities. *J Neurosci* **28**, 11830-11838, doi:10.1523/JNEUROSCI.3879-08.2008 (2008).

[4.12] Timko, B. P. *et al.* Electrical recording from hearts with flexible nanowire device arrays. *Nano Lett* **9**, 914-918, doi:10.1021/nl900096z (2009).

[4.13] Kim, D. H. *et al.* Materials for multifunctional balloon catheters with capabilities in cardiac electrophysiological mapping and ablation therapy. *Nat Mater* **10**, 316-323, doi:10.1038/nmat2971 (2011).

[4.14] Peppas, N. A., Hilt, J. Z., Khademhosseini, A. & Langer, R. Hydrogels in biology and medicine: From molecular principles to bionanotechnology. *Advanced Materials* **18**, 1345-1360, doi:10.1002/adma.200501612 (2006).

[4.15] Zhang, H. B., Jackson, J. K. & Chiao, M. Microfabricated Drug Delivery Devices: Design, Fabrication, and Applications. *Advanced Functional Materials* **27**, 1703606, doi:ARTN 170360610.1002/adfm.201703688 (2017).

[4.16] Lin, S. *et al.* Stretchable Hydrogel Electronics and Devices. *Adv Mater* **28**, 4497-4505, doi:10.1002/adma.201504152 (2016).

[4.17] Fattahi, P., Yang, G., Kim, G. & Abidian, M. R. A review of organic and inorganic biomaterials for neural interfaces. *Adv Mater* **26**, 1846-1885, doi:10.1002/adma.201304496 (2014).

[4.18] Jiang, Y. W. & Tian, B. Z. Inorganic semiconductor biointerfaces. *Nat Rev Mater* **3**, 473-490, doi:10.1038/s41578-018-0062-3 (2018).

[4.19] Jeong, J. W. *et al.* Soft materials in neuroengineering for hard problems in neuroscience. *Neuron* **86**, 175-186, doi:10.1016/j.neuron.2014.12.035 (2015).

[4.20] Simon, D. T., Gabrielsson, E. O., Tybrandt, K. & Berggren, M. Organic Bioelectronics: Bridging the Signaling Gap between Biology and Technology. *Chem Rev* **116**, 13009-13041, doi:10.1021/acs.chemrev.6b00146 (2016).

[4.21] Asplund, M., Nyberg, T. & Inganas, O. Electroactive polymers for neural interfaces. *Polym Chem-Uk* **1**, 1374-1391, doi:10.1039/c0py00077a (2010).

[4.22] Lee, H. R., Kim, C. C. & Sun, J. Y. Stretchable Ionics - A Promising Candidate for Upcoming Wearable Devices. *Adv Mater* **30**, e1704403, doi:10.1002/adma.201704403 (2018).

[4.23] Sjostrom, T. A. *et al.* A Decade of Iontronic Delivery Devices. *Adv Mater Technol-Us* **3**, 1700360, doi:ARTN 170036010.1002/admt.201700360 (2018).

[4.24] Chun, H. & Chung, T. D. Iontronics. *Annu Rev Anal Chem (Palo Alto Calif)* **8**, 441-462, doi:10.1146/annurev-anchem-071114-040202 (2015).

[4.25] Sun, J. Y. *et al.* Highly stretchable and tough hydrogels. *Nature* **489**, 133-136, doi:10.1038/nature11409 (2012).

[4.26] Keplinger, C. *et al.* Stretchable, transparent, ionic conductors. *Science* **341**, 984-987, doi:10.1126/science.1240228 (2013).

[4.27] Ono, T., Sugimoto, T., Shinkai, S. & Sada, K. Lipophilic polyelectrolyte gels as super-absorbent polymers for nonpolar organic solvents. *Nat Mater* **6**, 429-433, doi:10.1038/nmat1904 (2007).

[4.28] Takahashi, H., Itoga, K., Shimizu, T., Yamato, M. & Okano, T. Human Neural Tissue Construct Fabrication Based on Scaffold-Free Tissue Engineering. *Adv Healthc Mater* **5**, 1931-1938, doi:10.1002/adhm.201600197 (2016).

[4.29] Darnell, M. C. *et al.* Performance and biocompatibility of extremely tough alginate/polyacrylamide hydrogels. *Biomaterials* **34**, 8042-8048, doi:10.1016/j.biomaterials.2013.06.061 (2013).

[4.30] Gabrielsson, E. O. & Berggren, M. Polyphosphonium-based bipolar membranes for rectification of ionic currents. *Biomicrofluidics* **7**, 64117, doi:10.1063/1.4850795 (2013).

[4.31] Han, J. H., Kim, K. B., Kim, H. C. & Chung, T. D. Ionic circuits based on polyelectrolyte diodes on a microchip. *Angew Chem Int Ed Engl* **48**, 3830-3833, doi:10.1002/anie.200900045 (2009).

[4.32] Cayre, O. J., Chang, S. T. & Velev, O. D. Polyelectrolyte diode: Nonlinear current response of a junction between aqueous ionic gels. *J Am Chem Soc* **129**, 10801-10806, doi:10.1021/ja072449z (2007).

[4.33] Tybrandt, K., Larsson, K. C., Richter-Dahlfors, A. & Berggren, M. Ion bipolar junction transistors. *Proc Natl Acad Sci U S A* **107**, 9929-9932, doi:10.1073/pnas.0913911107 (2010).

[4.34] Tybrandt, K., Gabrielsson, E. O. & Berggren, M. Toward complementary ionic circuits: the npn ion bipolar junction transistor. *J Am Chem Soc* **133**, 10141-10145, doi:10.1021/ja200492c (2011).

[4.35] Kim, K. B., Han, J.-H., Kim, H. C. & Chung, T. D. Polyelectrolyte junction field effect transistor based on microfluidic chip. *Applied Physics Letters* **96**, 143506, doi:10.1063/1.3389492 (2010).

[4.36] Rivnay, J. *et al.* Organic electrochemical transistors. *Nat Rev Mater* **3**, 17086, doi:10.1038/natrevmats.2017.86 (2018).

[4.37] Tybrandt, K., Forchheimer, R. & Berggren, M. Logic gates based on ion transistors. *Nat Commun* **3**, 871, doi:10.1038/ncomms1869 (2012).

[4.38] Kwak, S. H. *et al.* Densely charged polyelectrolyte-stuffed nanochannel arrays for power generation from salinity gradient. *Sci Rep* **6**, 26416, doi:10.1038/srep26416 (2016).

[4.39] Lee, H.-R. *et al.* A Stretchable Ionic Diode from Copolyelectrolyte Hydrogels with Methacrylated Polysaccharides. *Advanced Functional Materials*, doi:10.1002/adfm.201806909 (2018).

[4.40] Han, J. H. *et al.* Ion flow crossing over a polyelectrolyte diode on a microfluidic chip. *Small* **7**, 2629-2639, doi:10.1002/smll.201100827 (2011).

CHAPTER 5

Ion-to-Ion Amplification through Open Junction Ionic Diode[5.1]

5.1. Introduction

As biological signals are mainly based on ion transport, the differences in signal carriers have become a major issue for the intimate communication between electrical devices and biological areas[5.2-4]. Particularly, as the amount of ions acquired from biological systems is very small, it is also required to amplify the weak ionic signals for the effective signal processing. In this respect, there have been many researches to detect the ionic signals from biological areas by using ion-based signal processing devices such as ion p-n junction diodes[5.5-7] and ion bipolar junction transistors (IBJTs)[5.8-10].

However, the physics of signal amplification in an ionic system has not been

introduced yet, and it is very difficult to apply the mechanism of signal amplification for electrical semiconductors to an ionic system because ions are relatively heavier than electrons, so that they have low mobility. For instance, a bipolar junction transistor can be activated when the diffusion length of the minority carrier in the emitter is large enough to cross the base region[5.11]. However, such amplification is rather difficult to be achieved in ionic systems due to their low mobility. Additionally, because recombination of carriers does not occur in ionic systems, it takes time to reach the depletion state of devices under reverse bias[5.12]. In this respect, it is important to take advantage of the unique characteristics of ionic systems for designing ion-based signal transfer devices.

In this study, we report on ionic signal amplification as well as sensing through the open junction ionic diodes (OJIDs), which was presented in the previous chapter. By designing an open junction structure at microfluidic chip based-ionic diodes, ionic signals from the external environment can be directly transmitted to ionic devices. Furthermore, an amplification of ion signal was observed during an operation of an OJID. The mechanism of the ion-to-ion signal amplification was suggested and verified by revealing the generation of the breakdown ionic currents crossing over the diode during ion injections through experimental and computational studies. A method to enhance the amplification performance of OJIDs was suggested through the systematic parametric studies.

5.2. Experiments

5.2.1. Materials

For the fabrication of OJIDs, we used the same materials as covered in **Section 4.2.1**. In addition, Rhodamine B hydrazide (RBH), HEPES, acetonitrile, carboxyfluorescein (cFlu), copper sulfate, sodium hydroxide was used for the visualization of breakdown ion flux.

5.2.2. Electrochemical characterization

To characterize the response ionic signal after ion injection, an *in situ* measurement of the ionic current was conducted using an electrochemical analyzer (MP3, ZIVE) with a constant reverse bias on the ionic diodes. After the formation of a fully depleted state in the polyelectrolyte gel diodes, under a constant reverse current, ionic solution (0.1 M KCl, NaCl, LiCl) was injected into the open junction of the microfluidic chip through a microinjection needle connected to a picoliter microinjector (PLI-100A, Warner instruments). The microinjection needle was produced by pulling glass capillaries (GC100-10, Harvard Apparatus) with a dual-stage glass micropipette puller (PC-10, Narishige). To protect the tip of the microinjection needle during filling, which is vulnerable to high pressure, ionic solutions were back-filled by inserting a nonmetallic microsyringe (Microfil, World Precision Instruments) into the microinjection needles. The volume of injected ions was calibrated by controlling the injection pressure and time pulse of the picoliter microinjector.

5.2.3. Optical measurements

The distribution of injected ions was visualized using charged fluorescent dyes. After injecting cationic and anionic fluorescent dye solutions through the open junction of devices (10 μM Rhodamine 6G and 10 μM fluorescein sodium salt, each), fluorescence images were observed. To investigate the additional ion flux caused by ion injection, Rhodamine B hydrazide (RBH) and carboxy-fluorescein (cFlu) dyes were utilized, which are selectively responsive to Cu^{2+} and OH^-, respectively. An RBH concentration of 50 μM was employed in the 0.1 M KCl reservoir on the pSPA side with 0.1 M HEPES buffer (pH 7.0, 80 %) and acetonitrile (20 %). Additionally, 50 μM cFlu was adopted in the KCl reservoir on the pDADMAC side. The concentrations of $CuSO_4$ and NaOH were set to 0.1 M. The fluorescence was measured by a fluorescence microscope (TE200U, Nikon), and the devices were connected to a potentiostat (CompactStat, Ivium) for electrochemical analysis.

5.2.4. Condition of computational simulation

For the in-depth understanding of ion-to-ion amplification effect in OJIDs, computational simulations were performed by using COMSOL Multiphysics. To observe the generation of amplification ionic current during the temporary breakdown, the charged particle tracing model was used. The detailed information on the simulation conditions in this study is provided below.

1. Governing equation

1) Newton's second law of motion (To describe the movement of ions.).

$$\frac{d(m_p v)}{dt} = F_t \qquad (Eq.\,5.1)$$

- m_p: The mass of particle corrected by the theory of relativity.
- v: Velocity of the particle.
- F_t: Total force applied to the particle.

2) Lorentz force (The force of charged particles under an electrical field.)

$$F = eZE \qquad (Eq.\,5.2)$$

- e: Electric charge of the electron.
- Z: Formal charge of the particle.
- E: Electrical field.

3) Definition of bound charge density (ρ_v).

$$\rho_v = \nabla \cdot D, \quad D = \varepsilon_0 \varepsilon_r E \qquad (Eq.\,5.3, 4)$$

- ε_0: Vacuum permittivity.
- ε_r: Relative permittivity of specific material.

4) Definition of electric field ($\boldsymbol{E}$). (Combination of 3) and 4) leads to the Poisson's equation in electrostatics.)

$$\boldsymbol{E = -\nabla V} \qquad (\boldsymbol{Eq.5.5})$$

- $\boldsymbol{V}$: Electrical potential.
- Combination of Eq. [3-5] leads to the Poisson's equation in electrostatics.

5) Interaction between charged particles and electrical field by using Dirac-Delta function.

$$\boldsymbol{\rho_s = \int_{j=1}^{N_t} nZe\delta(r - q_j)} \qquad (\boldsymbol{Eq.5.6})$$

- $\boldsymbol{\rho_s}$: Space charge density.
- $\boldsymbol{N_t}$: Total number of particles.
- $\boldsymbol{n}$: Charge multiplication factor.
- $\boldsymbol{r}$: The position to calculate the charge.
- $\boldsymbol{q_j}$: Electric charge of the particle.

2. Boundary condition

1) At glass wall: diffuse scattering condition

$$\boldsymbol{v_t = v_c \sin\theta}, \qquad \boldsymbol{v_n = v_c \sin\theta} \qquad (\boldsymbol{Eq.5.7,8})$$

- $\boldsymbol{v_c}$: The particle velocity when striking the glass wall.
- $\boldsymbol{v_t}$ & $\boldsymbol{v_n}$: The velocity of particle in transverse and normal directions after striking the glass wall.

2) At gel/reservoir interface: freeze condition $(\boldsymbol{v = 0})$.

3. Parameters for simulation

To compensate the number of charged particles in simulated models for the real systems, charge multiplication factor ($\boldsymbol{n}$) was introduced for each particle. In this work, we set the number of injected ions in experiments as 10 particles in simulation. As the amount of the injected KCl solution was fixed to 0.1 M for 113 pL, each particle in models represents

$$\mathbf{113}[\boldsymbol{pL}] \times \mathbf{0.1}\left[\frac{\boldsymbol{mol}}{\boldsymbol{L}}\right] \times \mathbf{10^{-12}}\left[\frac{\boldsymbol{L}}{\boldsymbol{pL}}\right] \times \mathbf{6.02} * \mathbf{10^{23}}\left[\frac{\boldsymbol{ions}}{\boldsymbol{mol}}\right] \times \frac{\mathbf{1}}{\mathbf{10}} = \mathbf{6.8} * \mathbf{10^{11}}\ \boldsymbol{ions}$$

As well as the mobile ions, fixed charges in polyelectrolyte gels were designed by considering this factor. For the calculation of mass of particles, the hydration number of K^+ and Cl^- ions were assumed to 6. The relative permittivity in matrix was set to 80 considering the aqueous state of devices, which corresponds to the value of water at 20 °C[5.13].

5.3. Verification of ion-to-ion amplification mechanisms

5.3.1. Suggested mechanisms for ion-to-ion amplification

In the previous chapter, we suggested a method for direct sensing of ionic signals through OJIDs. By designing an ion-injectable hole at polyelectrolyte gel diodes, ionic signals from the external environment can be directly transmitted to active elements of ionic devices. Moreover, it was observed that the minute ionic signals injected into the open junction can be amplified to a large amount of ions, which give an fascinating point for ion based signal processing system.

The proposed mechanism of the ion-to-ion amplification effect through the OJIDs is illustrated in **Figure 5.1**. When reverse bias voltages are applied to the OJIDs at the initial stage, counter mobile ions in the polyelectrolyte gels are depleted, and co-ions in the reservoir cannot be transported to the diodes because the repulsive force acts on the fixed ions in the polyelectrolyte gels and potential drops are mainly applied to the depletion region of the device rather than the gel/reservoir interfaces. Therefore, if the minute ionic solution is injected into the region adjacent to the p-n junction interface in the reverse-biased state, the ionic signal can be followed by the reverse current peak. In particular, as the depletion region in OJIDs is temporarily neutralized by injected ions through the open junction of the devices, the transport number of each polyelectrolyte gel can be lowered, and then, the co-ions at pile-up regions can transport into the gels, which results in an additional ionic current from the reservoir region. This phenomenon is similar to the breakdown current in electronics but replenishable in aqueous ionic systems.

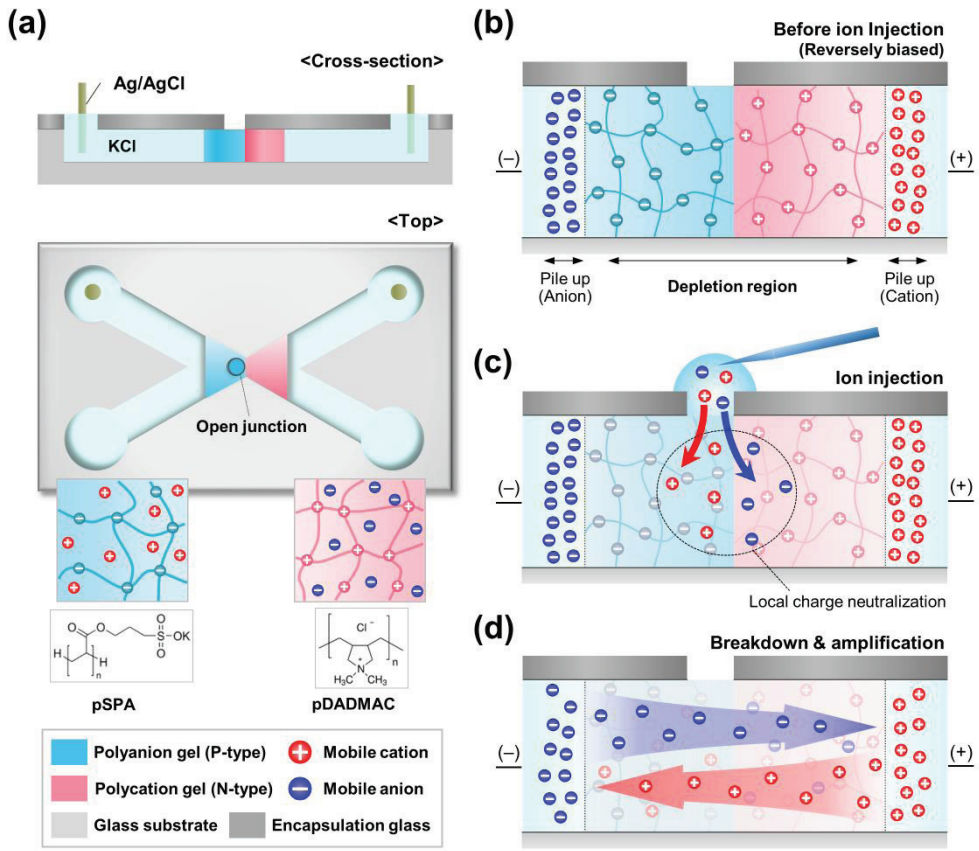

Figure 5.1 (a) Schematic representation of an OJID. Through the ion-injectable hole structure formed on the polyelectrolyte gel region, ionic signals can be directly transmitted to the active element of devices. (b-d) Suggested signal amplification mechanism by ion injection. (b) In the reverse-biased state of an OJID, the depletion region is formed in the diode, and mobile ions in the reservoir are piled up at reservoir/gel interfaces by charge repulsion. (c) When an ion is injected through the open junction, local charge neutralization in the diode occurs, and in addition to the injected ions, (d) an additional breakdown current from the reservoir can be observed.

5.3.2. Visualization of breakdown ion flux

To test our hypothesis that the breakdown ionic current occurs across the reservoir region due to local charge neutralization in the depletion region of OJIDs after ion injection through the microhole, selective fluorescent dyes[5,12] that emit fluorescence by reaction with a specific ion were utilized. The selective reaction of Rhodamine B hydrazide (RBH) with the Cu^{2+} ion was used to observe the crossing current due to the cationic flux from the reservoir on the pDADMAC side (**Figure 5.2a**). When the KCl solution including RBH was introduced into the pSPA side while $CuSO_4$ was introduced into the pDADMAC side and a reverse-bias voltage was applied, fluorescence was rarely detected due to the charge repulsion between fixed charges in the polyelectrolyte gels and counter mobile ions in the reservoir region. Interestingly, after injecting a KCl solution through the microhole in the OJIDs, a red fluorescence signal was observed at the KCl+RBH reservoir/pSPA interface, as shown in **Figure 5.2b**; this finding implies that the Cu^{2+}-based ionic flux crossed over to the polyelectrolyte gels during KCl injection. Likewise, the anion-based breakdown current from the pDADMAC side was also confirmed by the observation of OH^- flux through the selective reaction of carboxy-fluorescein (cFlu) on the pDADMAC side reservoir, which showed cyan fluorescence under a basic environment after the injection of a KCl solution (**Figure 5.3**). These results confirm that an additional amplification ionic current can occur during the temporary breakdown of the ionic diodes.

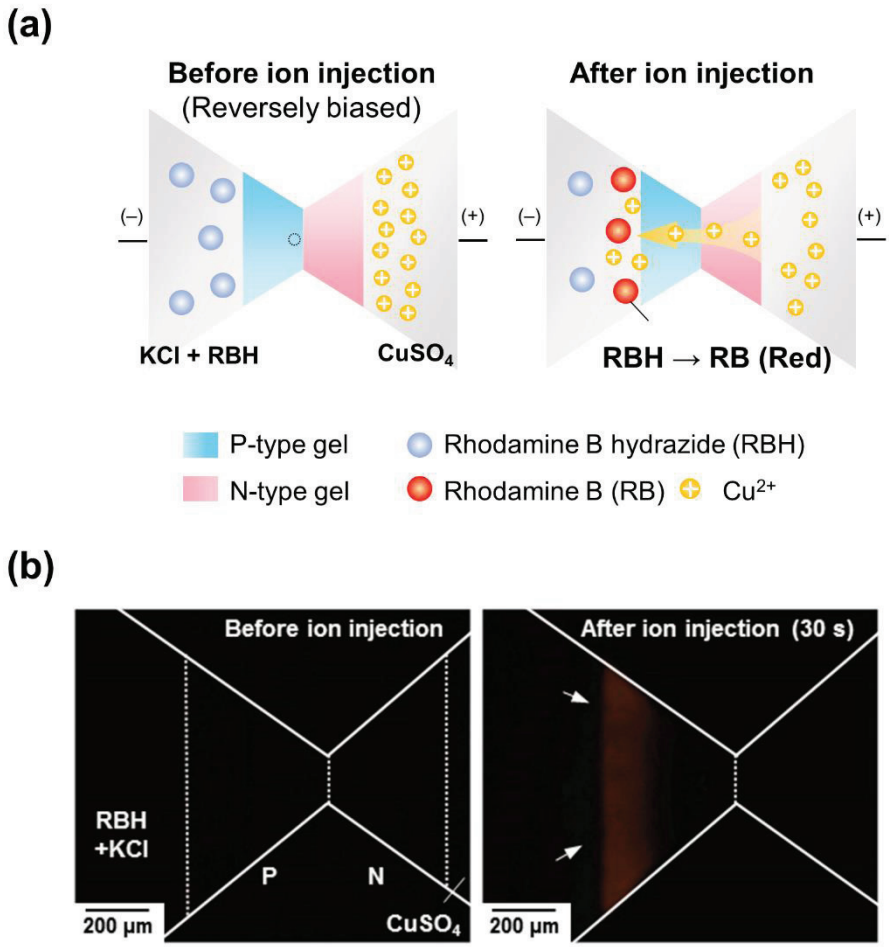

Figure 5.2 (a) Schematic depictions and (b) images of fluorescence induced by Cu^{2+} ion after ion injection. When Rhodamine B hydrazide (RBH) was incorporated into the reservoir on the pSPA side, red fluorescence emerged after KCl injection to the open junction, which was caused by the Cu^{2+} ion flux induced by the breakdown of the ionic diode.

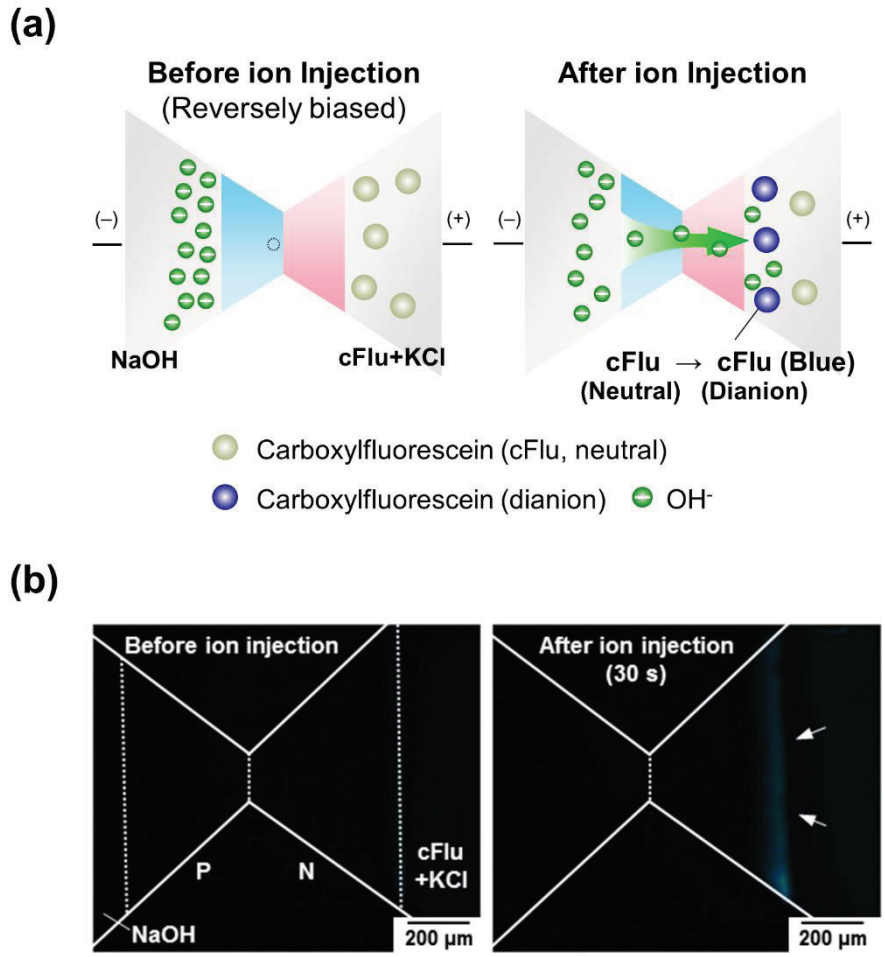

Figure 5.3 (a) Schematic illustrations and (b) images of fluorescence induced by OH^- ion flux after ion injection. As pH-sensitive carboxylfluorescein (cFlu) dye was introduced into the reservoir on the pDADMAC side, OH^- based anionic flux was visualized through cyan fluorescence.

5.3.3. Numerical simulation

In addition to the visualization of the ion flux using selective fluorescence dyes, we performed numerical simulation to investigate the generation of the breakdown ionic current crossing the diode using COMSOL Multiphysics. The physical models and their boundary conditions used for simulation are displayed in **Figure 5.4a**. A two-dimensional (2D) model was adopted to save computational resources, and the 2D geometry of the polyelectrolyte gels in the simulation was designed to be identical to that of the real devices. In the steady state under the reverse bias, it was assumed that the fully depleted state of the OJIDs could be attained, in which the regions of the pSPA and pDADMAC gels were only composed of anionic and cationic fixed charges, respectively. Additionally, the charge pile-up region at the gel/reservoir interface was designed by introducing a Cl^- accumulation layer on the pSPA side (detailed information regarding the numerical simulation is provided in **Section 5.2.4**.).

Figure 5.4b shows the ion distributions in the gel diode during the ion-to-ion amplification. Considering the symmetric structure of the model, only the anionic (Cl^- ions) flux crossing the pSPA region was calculated using the charged particle tracing model. Before ion injection, most of the Cl^- ions in the reservoir held their positions because of the repulsion between Cl^- ions and fixed charges in the pSPA gel. However, when the K^+ ion particles (overall charge amount = 1.08 μC) were injected near the junction at t = 1 s, a small amount of injected K^+ ions activated Cl^- ions in the pile-up region, overcoming the repulsion between anionic fixed charges in the pSPA gel and passing to the pDADMAC gel region.

Furthermore, the behavior of amplified ionic currents in OJIDs was also predicted by differentiating the change of the charge amount which was calculated by computational

simulation (**Figure 5.5a**). In this work, the width of gel was set to 150 μm for saving computational resources by reducing transmittance times for ion-to-ion amplification. After ion injection (t= 0 s), the gradual onset and decay behavior was also shown in the change of calculated amplified currents (**Figure. 5.5b**). Moreover, it requires a few seconds for the co-ions at pile-up regions to dissipate completely, which is comparable to the time scale of the 150-μm-wide devices, which will be shown in the **Section 5.5.1**

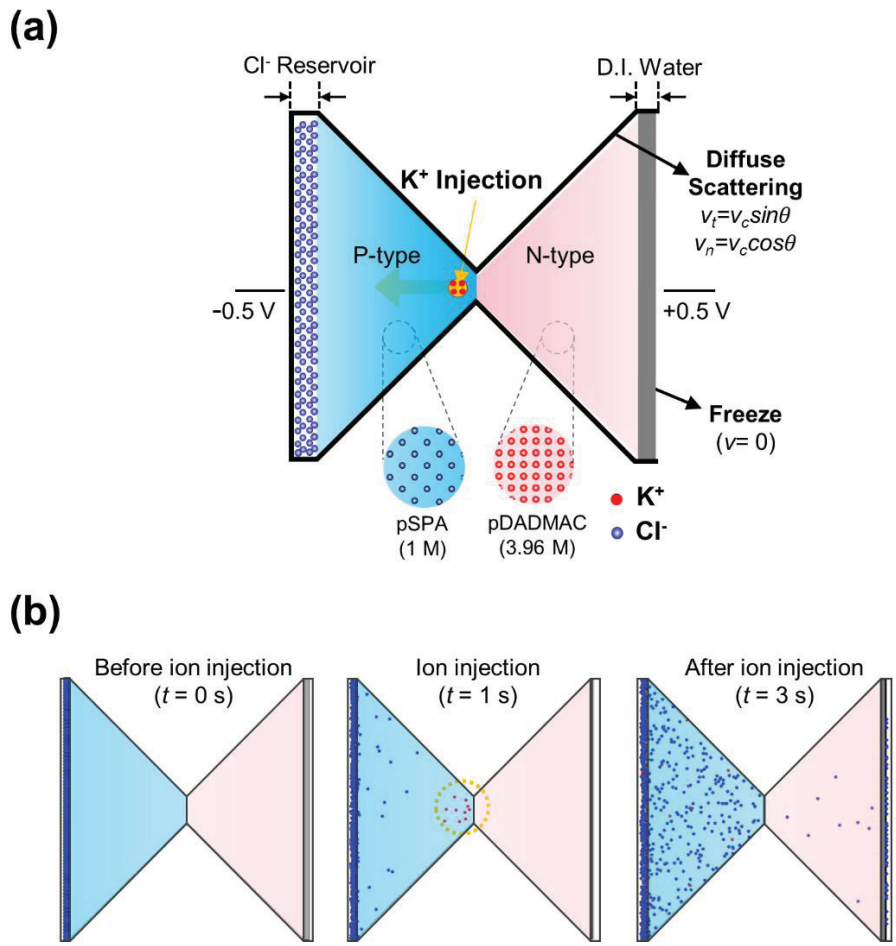

Figure 5.4 (a) 2D model and boundary conditions for numerical simulation. (b) Before ion injection, Cl^- ions were piled up at the reservoir/gel interface by charge repulsion. When ions were injected into the open junction at 1 s, charge neutralization in pSPA occurred locally, and the breakdown current (Cl^- ion flux) could be observed on the reservoir side.

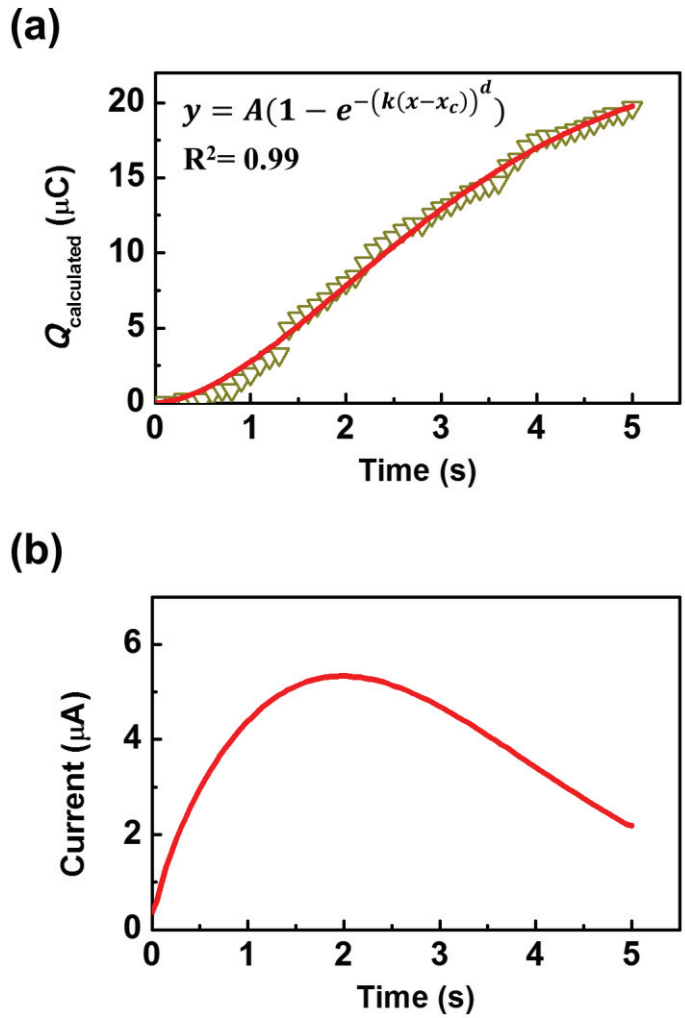

Figure 5.5 (a) Change of detected charge amount during ion-to-ion amplification calculated by using FEM simulation. Considering that the transportation of co-ions in OJID is based on temporary breakdown of diodes, it was fitted by a sigmoidal Weibull function (red line). (b) Expected ionic current behavior through the differentiation of fitted curve in (a).

5.4. Characterization of ion-to-ion amplification

5.4.1. *I-V* sweep characteristics of OJIDs

To analyze the rectification properties of the OJIDs under various conditions, the *I-V* sweep characteristics of the devices were measured using an electrochemical analyzer (MP3, ZIVE). **Figure 5.6a** exhibits the *I-V* sweep curves of OJIDs with varying reservoir ionic solutions in microfluidic channels. After a reverse voltage scan, the rectification of the ionic current was commonly observed, with hysteresis behavior, which was caused by the depletion of ions as previously reported[5.12]. When the cation in the reservoir was changed from KCl to NaCl and LiCl, the level of forward ionic current was slightly decreased due to differences in the conductivity of the cations in the polyelectrolyte gels. However, as the change of cation in the reservoir rarely affected the reverse current, the overall rectification property of the devices was well maintained.

In addition to the variations observed with the change in the reservoir ionic solution, the rectifying behavior of various OJIDs was observed with respect to the width of the constituent polyelectrolyte gels in ionic diodes (**Figure 5.6b**). Although the hysteresis area of the *I-V* curves under a reverse bias also increased as the width of the gel increased for the formation of a fully depleted state, the reverse current of the diodes remained nearly unchanged, demonstrating the stable rectification behavior of the devices.

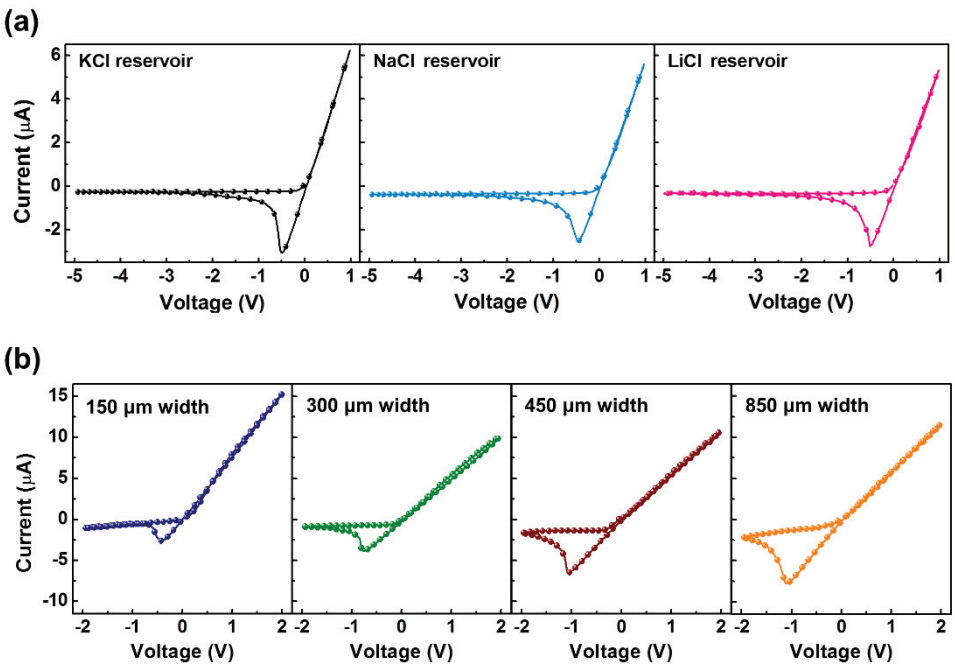

Figure 5.6 *I-V* sweep curves of various OJIDs with respect to (a) reservoir ionic solution and (b) width of constituent polyelectrolyte gels. The scan rate during the *I-V* sweep was set to 25 mV/s.

5.4.2. *In-situ* measurement of breakdown ionic currents

Based on the verification of the ion-to-ion amplification mechanism in the OJIDs, various case studies were conducted to investigate the factors responsible for the modulation and improvement of the amplification effect in the devices. **Figure 5.7a** presents the changes in the responsive ionic peak current after ion injection as a function of the concentration of the KCl reservoir. An *in situ* measurement of the breakdown current during ion injection was conducted by varying the ionic concentration of the KCl reservoir from 1 mM to 0.1 M, where the amount of the injected ion solution was fixed to KCl 0.1 M for 113 pL (Q~ 2.16 μC). For quantitative analysis, the detected charge amount was measured through the integration of the reverse current peak in the *i-t* curve for 1 min from the onset of ion injection (**Figure 5.7b**). When a sufficient depletion state was formed in the OJIDs by applying a reverse bias of –1 V for 3 min, the ionic current was well rectified, indicating only a low leakage current. After ion injection, the ionic signal response was observed in the form of the reverse current peak, as predicted. The onset and decay of ionic current peaks occurs during approximately 20~30 seconds for a diode with a width of 450 μm, which is quite different from the basic kinetics of a single polyelectrolyte hydrogel, which shows the sharp response to the bias. This result indicates that an additional ionic current across the reservoir region can also be confirmed by an electrochemical signal.

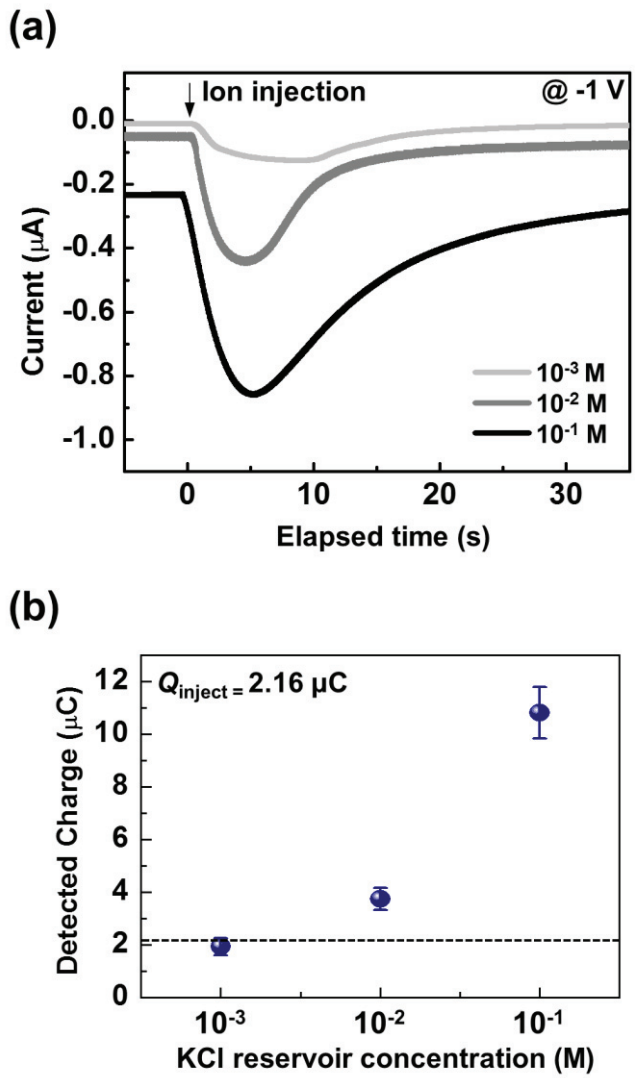

Figure 5.7 Changes in responsive ionic current after ion injection. Amplified ionic current began to flow when an ionic signal was injected and lasted for 20-30 s. (a) When the ion concentration in the reservoir was increased from 1 mM to 0.1 M, a remarkable change in the breakdown current was measured, thus (b) increasing the charge amount detected from the current peak.

For a KCl reservoir concentration of 1 mM, the amount of charge detected from the response current peak was measured to be 1.93 μC, which was similar to the charge of the injected ions. As the concentration of the KCl reservoir solution was increased to 0.01 M and 0.1 M, however, a considerable increase in the reverse peak current was observed. Moreover, the detected charge amount also increased to 3.75 μC and 10.81 μC, respectively. These results suggest that the reservoir concentration is related to the concentration of co-ions in the pile-up regions, which also increases the potential drops at the gel/reservoir interface for the generation of a breakdown ionic current from the reservoir. In this respect, in order to control the ionic signal amplification effect, it is necessary to understand the distribution of co-ions at pile-up regions based on the fundamental physics of the polyelectrolyte gel-based diodes as well as optimize the ionic transport performance of constituent polyelectrolyte gels in the material design aspects.

Additionally, the tendency between the reverse-bias voltage and the responsive ionic signal was also investigated, as shown in **Figure 5.8a**. When the reverse-bias voltage was varied from –0.5 V to –2 V and the concentration of the KCl reservoir was set to 0.1 M, the level of the ionic current peak was increased and even sharpened; thus, an increase in the charge amount was observed. It can be inferred that the field increases between both sides of the reservoir, which accelerates the crossing current through the diodes during the temporary breakdown. Furthermore, we also found that there was no significant difference in the performance of the devices regardless of the position of the hole as long as it is located near the junction interface (**Figure 5.9**).

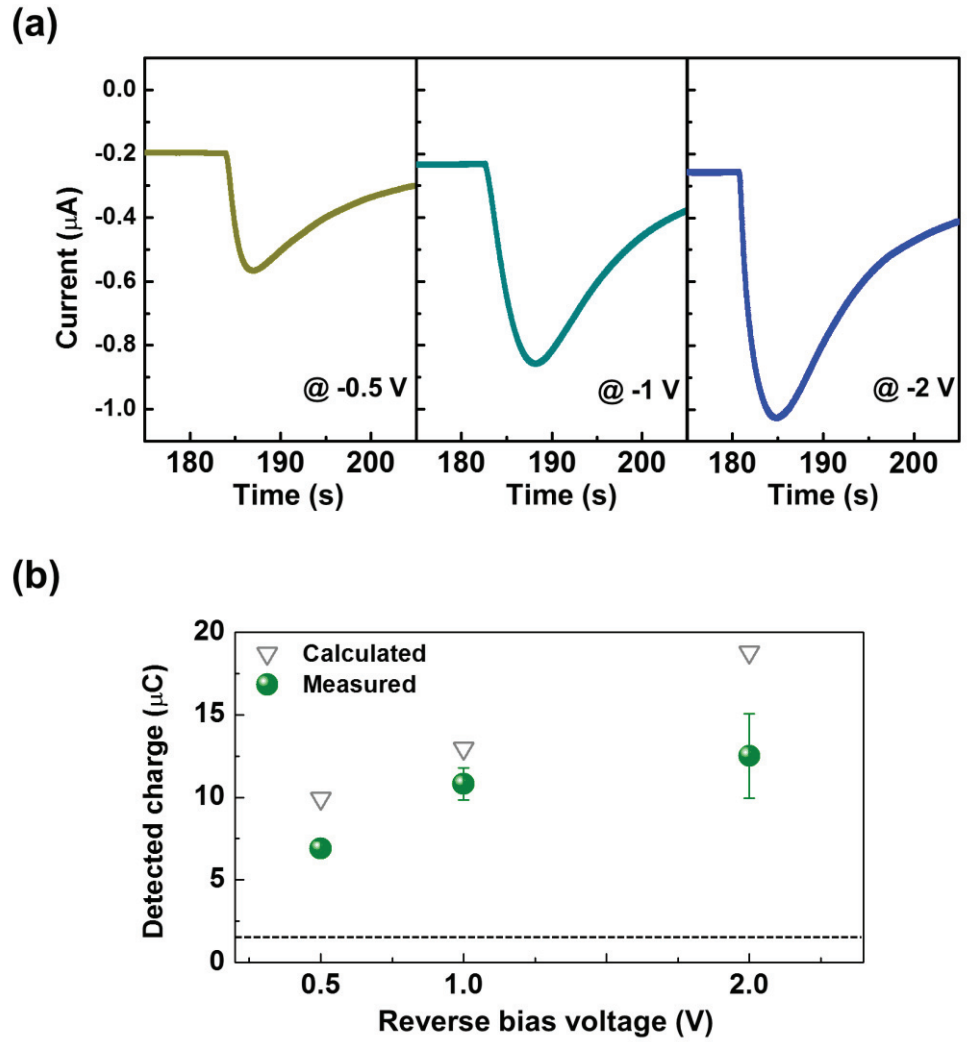

Figure 5.8 Changes of responsive ionic currents with respect to the bias conditions. (a) An additional increase in the breakdown currents was observed by varying the reverse-bias voltage conditions; this increase is related to the increase in the field applied to the diodes during breakdown. (b) The variation of the detected charge amount well matched the simulation results.

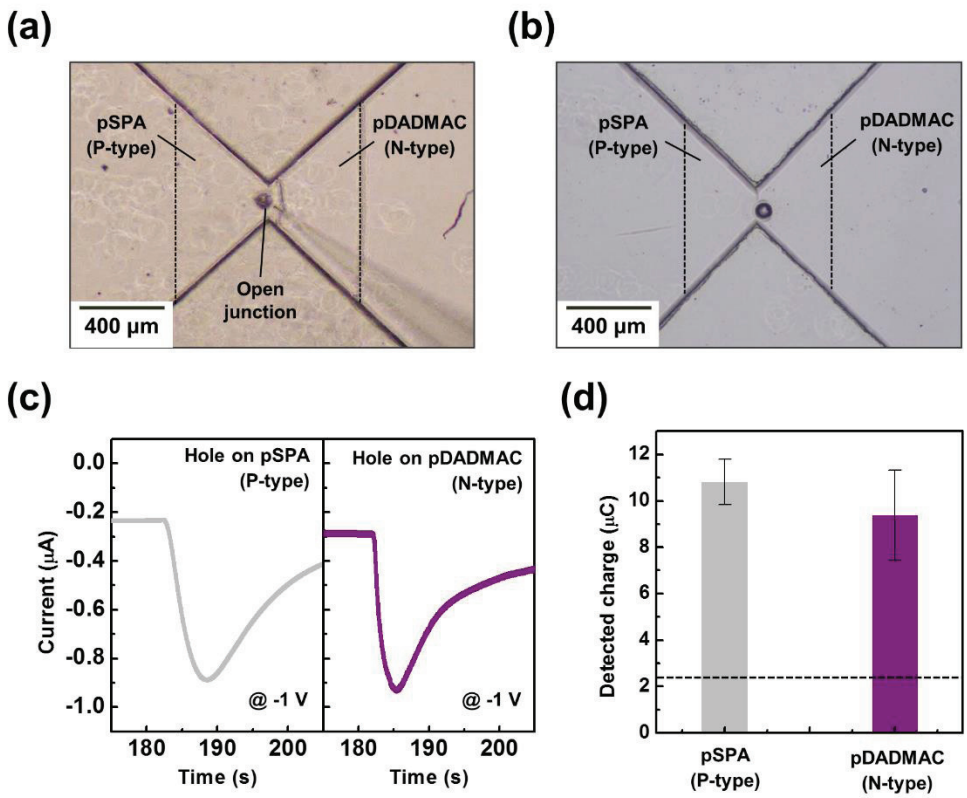

Figure 5.9 Comparison of the ion-to-ion amplification performance with the hole position. The representative image of OJIDs where the hole is located on (a) pSPA and (b) pDADMAC gel side. (c) The change in the responsive breakdown ionic current and (d) detected charge amount upon ion injection with respect to the position of hole. Despite the change of hole position, the characteristics of responsive current peak were nearly unchanged.

5.4.3. Ion species effect on amplification performance

We inspected the change in the amplification current of the OJIDs by varying the cations in the constituent reservoir solution and injecting a corresponding solution. **Figure 5.10 and 11** presents the signal characteristics map and calculated ionic charge amount with respect to the cation species in the reservoir and the variation in the injected ionic solution from KCl to NaCl and LiCl. Among the various types of cations constituting the reservoir ionic solution, the highest breakdown current peak was observed in the KCl reservoir-based diodes, and their amplification effect was progressively weakened in going from a NaCl to LiCl reservoir-based diode.

The ion mobility of cations in the polyelectrolyte gels was concluded to have a great effect on the crossing of the diodes during the momentary neutralization of the diodes in the reverse-biased state. When cations are hydrated, water molecules are attracted to the charged ions, and the effective radius of alkali ions increases in the order of $K^+<Na^+<Li^+$ (**Table 5.1**)[5.14], which leads to a decrease in mobility in polyelectrolyte gels. To confirm the difference in ion mobility with varying reservoir solution, ion conductivities were measured from the slope of the *I-V* sweep curve using the salt bridge model. The changes in ion conductivities in the pSPA and pDADMAC gels with different reservoir solutions are shown in **Figure 5.12**. In the case of the pSPA (p-type) gel, a decrease in ion conductivity was observed as the effective hydrated radius of the constituent cation increased. However, the ion conductivity in the pDADMAC (n-type) gel remained nearly unchanged with respect to the reservoir solution because the conduction of n-type gels is mainly caused by anions. However, we believe that the difference in ion mobility due to the difference in the effective hydrated radius of the

cations could also be effective in crossing the n-type gel region from the reservoir during the breakdown of the diodes.

In addition to the change in the reservoir solution, the change in the responsive ionic peak current and the subsequent detected charge amount were confirmed by varying the species of injected ionic solutions. As the mobility of cations in injected ionic solutions decreased (Li^+<Na^+<K^+), a reduction in the amplification effect of the devices was observed. Such changes could be caused by the difference in the drift length of the cations in the polyelectrolyte gels for local charge neutralization when injected, which can be related to the activation of the amplification mechanism in the diodes.

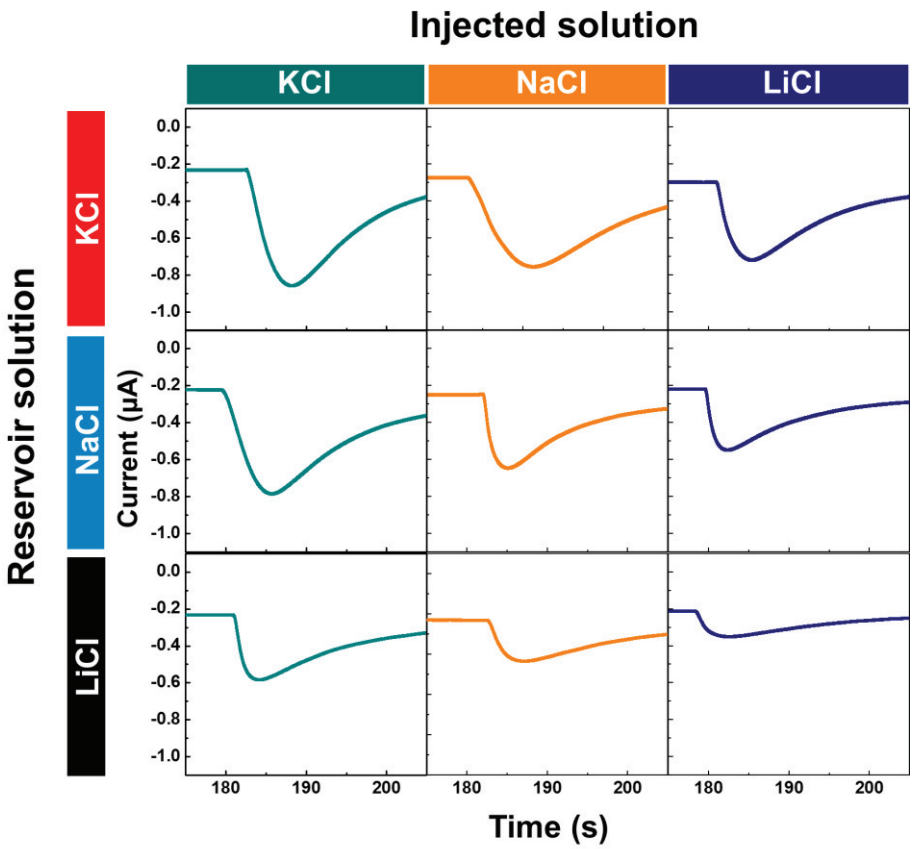

Figure 5.10 Breakdown current response map of various OJIDs considering the cations in the reservoir and injected ionic solutions. As the hydrated ionic radius increases (K^+< Na^+< Li^+), the ion mobility in the polyelectrolyte gels decreases, which yields different signal responses with varying constituent ions.

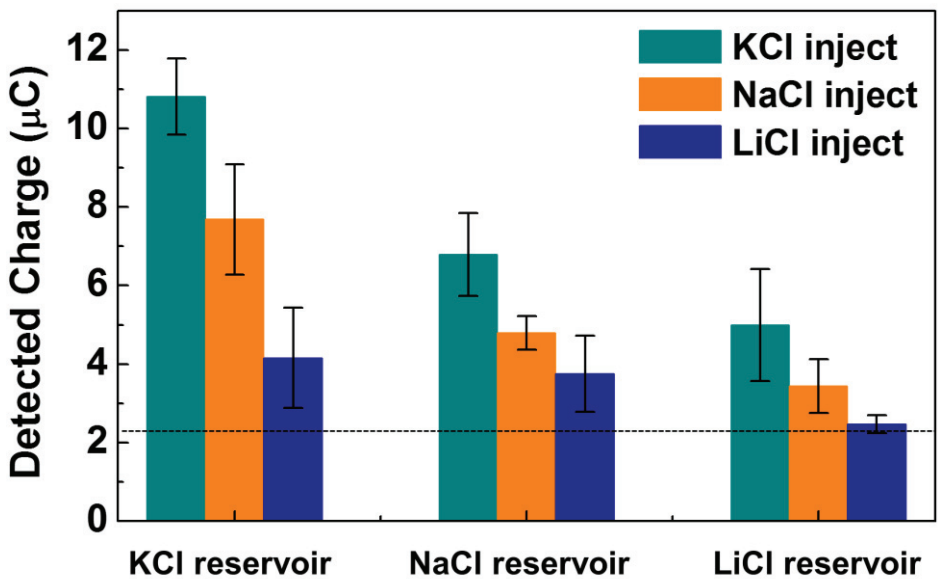

Figure 5.11 Measured charge amount from responsive current peak of various OJIDs with respect to the cation species in the reservoir and injected ionic solutions.

Ion	Bare (nm)	Hydrated (nm)
Li^+	0.094	0.382
Na^+	0.117	0.358
K^+	0.149	0.331
Cl^-	0.164	0.332

Table 5.1 The radii of various ions in the bare and hydrated states[5.14].

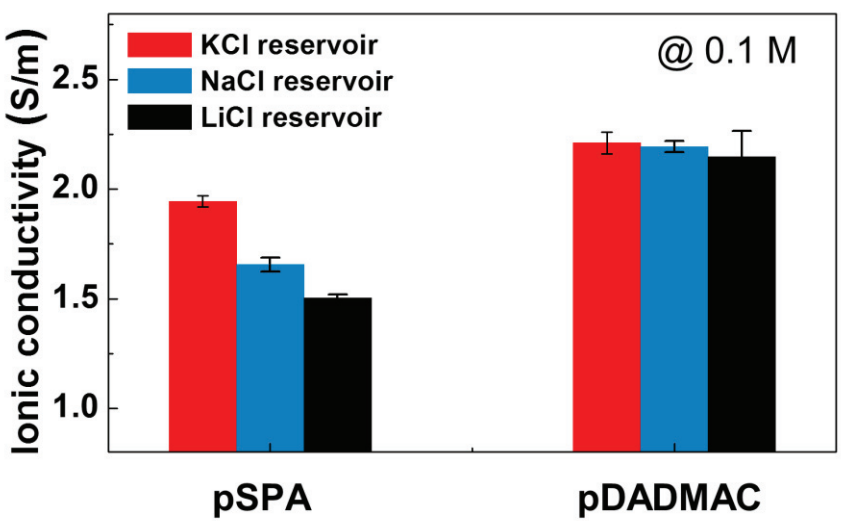

Figure 5.12 Changes in the ionic conductivity in the pSPA gel with respect to the cations in the reservoir solutions.

5.5. Enhancement of device performance

5.5.1. Size effects for signal amplification

Through the various case studies, it was verified that the amplification effect of the ion signal is systematically controllable by modulating the parameters related to the breakdown current in the diodes, such as the concentration of reservoir ionic solutions and the field applied between the reservoirs. Furthermore, additional improvement of the amplification effect can be expected with a decrease in the width of the constituent polyelectrolyte gels of the diodes. **Figure 5.13a** presents the responsive characteristics maps of various OJIDs with respect to the width of the polyelectrolyte gels in the diodes. The widths of both the pSPA and pDADMAC gels were modulated from 150 μm to 850 μm, and the reverse bias voltages were varied from –0.5 V to –2 V. As observed in each reverse-bias voltage condition, the intensity of the breakdown current was remarkably increased as the width of the gel constituting the diode decreased, indicating a significant improvement of the ion-to-ion amplification effect. However, when the width of the constituent gel was increased to 850 μm, the amplification effect of the devices was diminished, and the detected charge amount was close to that of the injected KCl ionic solution. These results strongly suggest that the decrease in the width of the constituent gels in the OJIDs is a key factor for inducing breakdown current by decreasing the crossing distance as well as increasing the field applied between the polyelectrolyte gels.

Along with the width of the diodes, an additional increase in the amplitude and sharpness of the response current peak was achieved as the reverse-bias voltage was increased to –2 V, which resulted in an improvement in the amplification ratio up to 18.9 times the charge amount of the injected KCl ionic solution (**Figure 5.13b**). Further

enhancement of the amplification performance can be expected through advances in the fabrication process for scaling down of devices.

5.5.2. Response time of OJID

Additionally, it was observed that the transmittance times for the signal response were drastically reduced. Based on slow breakdown sequences, the OJID exhibits a long response time compared to the conventional electronic devices. For practical application of OJIDs to the biological signal sensing, it is required to shorten the response time of the devices. Therefore, we also analyzed the speed of OJIDs; the results are presented in **Figure 5.14**. The response time of OJIDs was quantified by the time that recovers the 90% of initial currents ($t_{90\%}$) after ion injection (**Figure 5.14a)**. When the constituent gels and reverse-bias voltage of devices were set to 450 μm and –1 V, respectively, $t_{90\%}$ of the devices was measured to be approximately 30~40 s. However, as the width of the gel constituting the diode decreased to 150 μm, $t_{90\%}$ of the devices was significantly decreased below 10 s (**Figure 5.14b)**.

5.5.3. Stability of OJID

To confirm the stability of the amplification performance of the OJIDs, we measured the changes in the responsive currents in the devices for the five ion injections (**Figure 5.15**). The width of the constituent gels, concentration of KCl reservoir solution and reverse-bias voltage of devices were set to 450 μm, 0.1 M and –1 V respectively. When

the minute KCl ionic solutions were injected with an interval of 1 minute, the responsive current peaks of OJIDs were nearly unchanged with the repeated ion injections, thus showing the stable amplification performances of the devices.

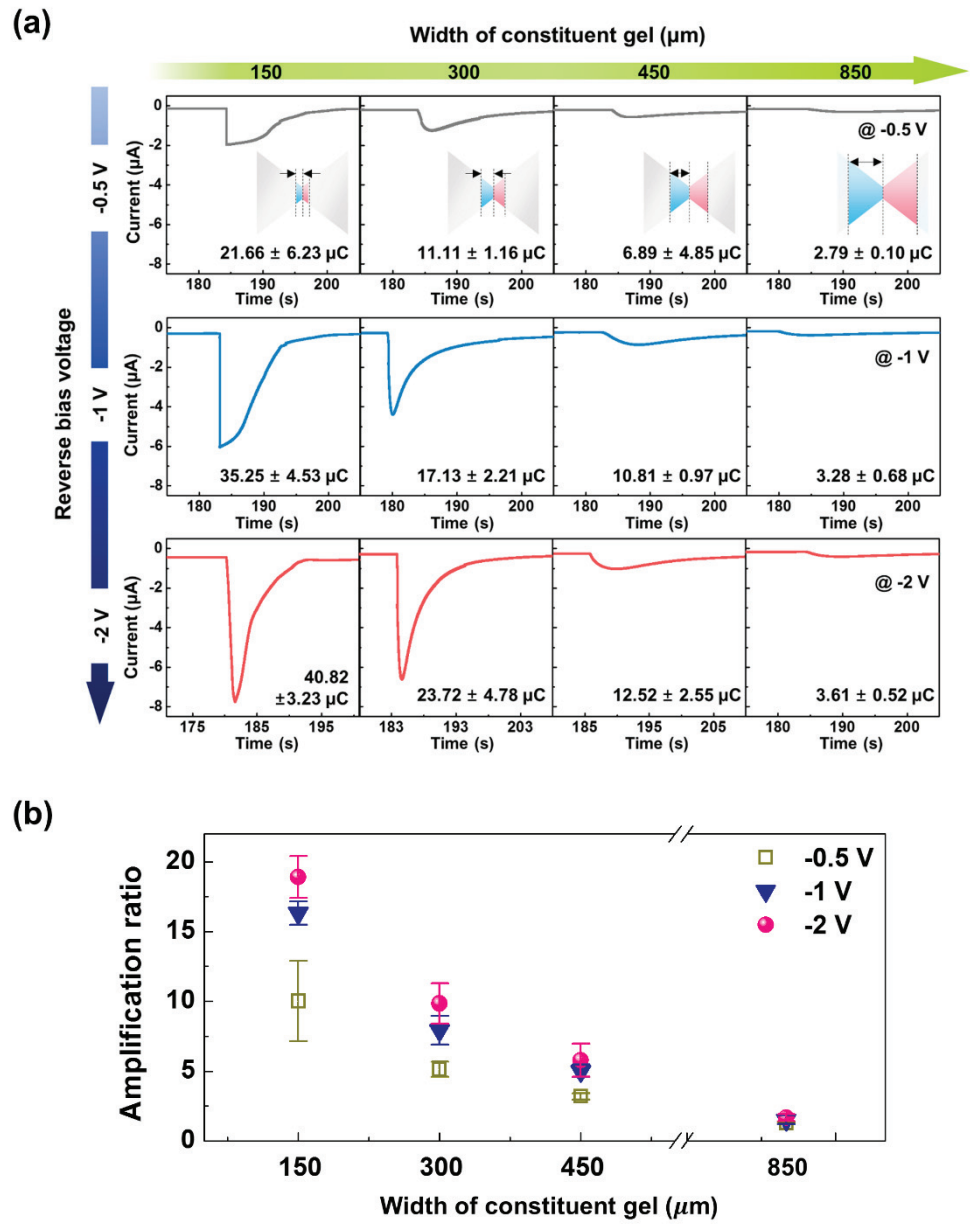

Figure 5.13 (a) Change in the responsive breakdown ionic current and (b) calculated amplification ratio in charge scale upon ion injection with respect to the dimensions of the constituent gels (150 μm~ 850 μm) and reverse-bias voltage (–0.5 V~ –2 V). The reservoir solution and injected ionic solution were fixed to 0.1 M KCl.

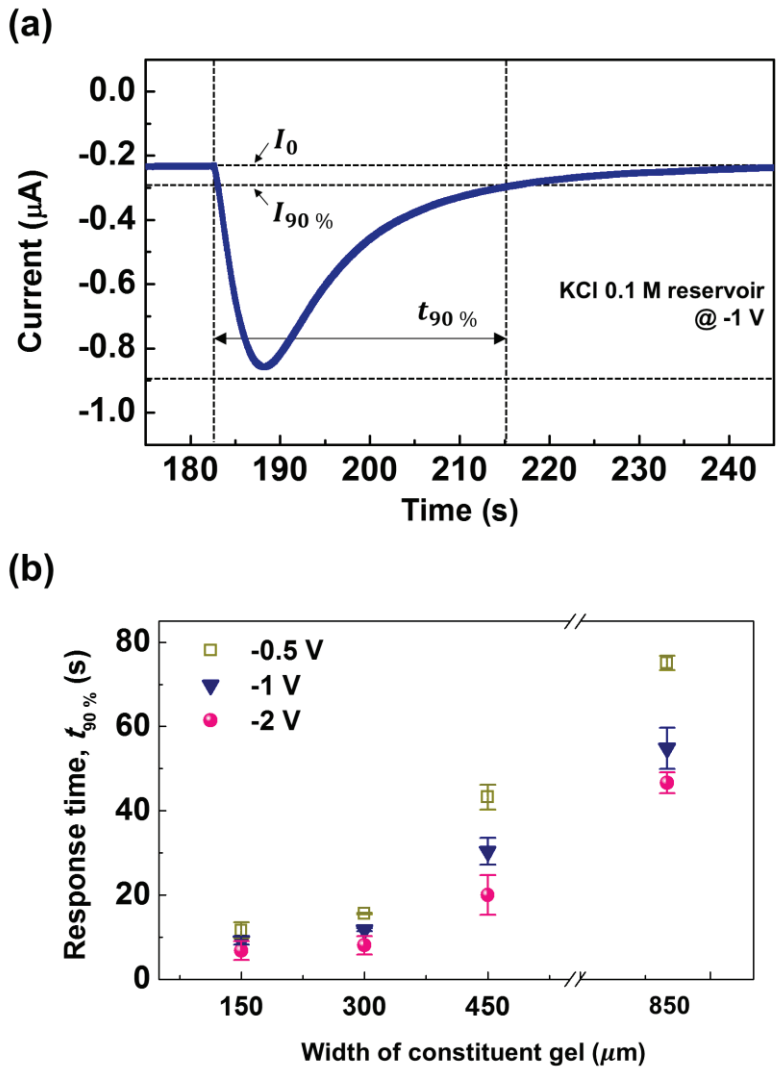

Figure 5.14 (a) Changes in breakdown ionic current of the 450-μm-wide OJID for showing the response time of devices. (b) The calculated $t_{90\%}$ of various OJIDs with respect to the dimensions of the constituent gels (150~850 μm) and reverse-bias voltage (–0.5 V~ –2 V). The concentrations of the reservoir solution and injected ionic solution were fixed to 0.1 M KCl, which corresponds to the **Figure 5.13** in the manuscript.

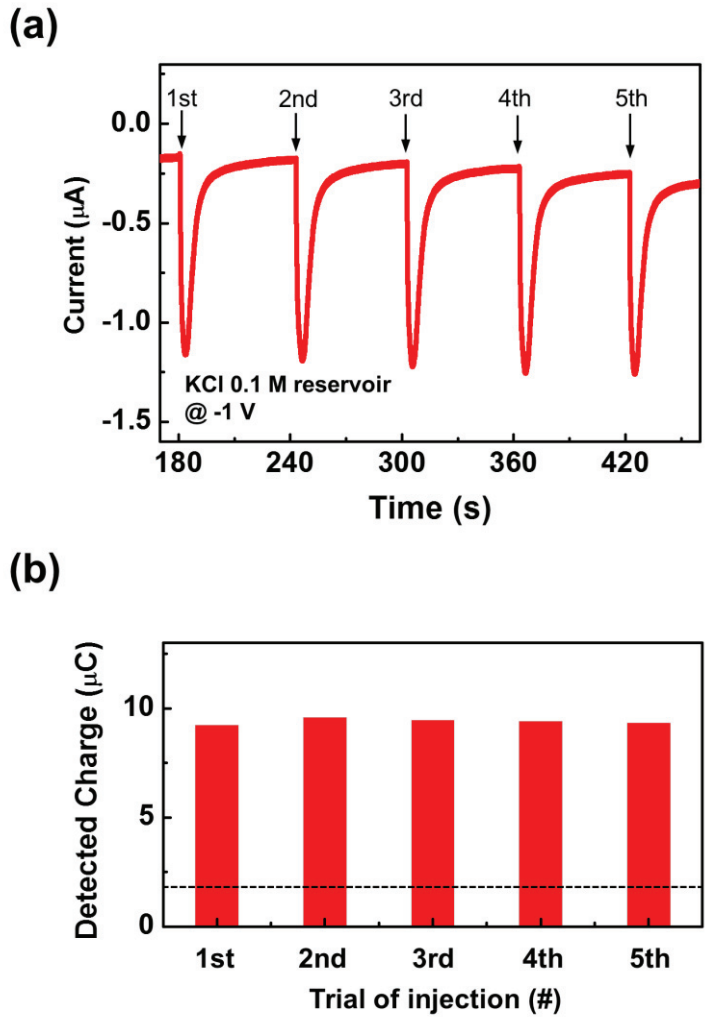

Figure 5.15 (a) The change of the responsive amplified ionic currents and (b) detected charges from the ionic current peaks after 5 ion injection times. The intervals of ion injection were set to 1 min. The amplification performance of the OJID was stable for the repeated ion injections.

5.6. Summary

In this study, we demonstrated unique sensing and amplification mechanisms based on the inherent features of ionic systems. Through the modified design of the microfluidic chip-based ionic diodes, direct communication between an ionic input signal and ionic devices was acheived. When an ionic solution is injected into the region adjacent to the interface of the p-n junction in the reverse-biased state, temporary breakdown in the diode can occur by the local charge neutralization in the depletion region at the polyelectrolyte gel junction, and an additional ionic current crossing over the diode from the reservoir can be generated in addition to the injected ionic signal. To verify the mechanisms of ion-to-ion signal amplification, the breakdown ionic flux was visualized using the ion-selective response of fluorescent dyes, which was also predicted by computational simulation. The signal amplification effect in open junction ionic diodes was successfully controlled by modulating the reservoir concentration, reverse-bias voltage and ion species. Furthermore, a considerable increase in the breakdown current was observed by scaling down the polyelectrolyte gels, which resulted in an amplification factor of approximately 20 times in fully ion-transfer systems. We believe that our findings indicate future opportunities for fabricating signal processing devices for ionic systems as well as for achieving intimate communication with biological signals.

References

[5.1] Lim, S.-M. *et al.* Ion-to-ion amplification through an open junction ionic diode. *Proc Natl Acad Sci U S A,* online published, doi: 10.1073/pnas.1903900116 (2019).

[5.2] Fattahi, P., Yang, G., Kim, G. & Abidian, M. R. A review of organic and inorganic biomaterials for neural interfaces. *Adv Mater* **26**, 1846-1885, doi:10.1002/adma.201304496 (2014).

[5.3] Jeong, J. W. *et al.* Soft materials in neuroengineering for hard problems in neuroscience. *Neuron* **86**, 175-186, doi:10.1016/j.neuron.2014.12.035 (2015).

[5.4] Lee, H. R., Kim, C. C. & Sun, J. Y. Stretchable Ionics - A Promising Candidate for Upcoming Wearable Devices. *Adv Mater* **30**, e1704403, doi:10.1002/adma.201704403 (2018).

[5.5] Gabrielsson, E. O. & Berggren, M. Polyphosphonium-based bipolar membranes for rectification of ionic currents. *Biomicrofluidics* **7**, 64117, doi:10.1063/1.4850795 (2013).

[5.6] Han, J. H., Kim, K. B., Kim, H. C. & Chung, T. D. Ionic circuits based on polyelectrolyte diodes on a microchip. *Angew Chem Int Ed Engl* **48**, 3830-3833, doi:10.1002/anie.200900045 (2009).

[5.7] Cayre, O. J., Chang, S. T. & Velev, O. D. Polyelectrolyte diode: Nonlinear current response of a junction between aqueous ionic gels. *J Am Chem Soc* **129**, 10801-10806, doi:10.1021/ja072449z (2007).

[5.8] Tybrandt, K., Larsson, K. C., Richter-Dahlfors, A. & Berggren, M. Ion bipolar junction transistors. *Proc Natl Acad Sci U S A* **107**, 9929-9932, doi:10.1073/pnas.0913911107 (2010).

[5.9] Tybrandt, K., Forchheimer, R. & Berggren, M. Logic gates based on ion transistors. *Nat Commun* **3**, 871, doi:10.1038/ncomms1869 (2012).

[5.10] Tybrandt, K., Gabrielsson, E. O. & Berggren, M. Toward complementary ionic circuits: the npn ion bipolar junction transistor. *J Am Chem Soc* **133**, 10141-10145, doi:10.1021/ja200492c (2011).

[5.11] Pierret, R. F. *Semiconductor device fundamentals*. (Addison-Wesley, 1996).

[5.12] Han, J. H. *et al.* Ion flow crossing over a polyelectrolyte diode on a microfluidic chip. *Small* **7**, 2629-2639, doi:10.1002/smll.201100827 (2011).

[5.13] Archer, D. G. & Wang, P. The Dielectric Constant of Water and Debye-Hückel Limiting Law Slopes. *Journal of Physical and Chemical Reference Data* **19**, 371-411, doi:10.1063/1.555853 (1990).

[5.14] Volkov, A. G., Paula, S. & Deamer, D. W. Two mechanisms of permeation of small neutral molecules and hydrated ions across phospholipid bilayers. *Bioelectroch Bioener* **42**, 153-160, doi:Doi 10.1016/S0302-4598(96)05097-0 (1997).

CHAPTER 6

Conclusion

6.1. Summary of results

In this study, the strategies to solve the practical issues in wearable devices have been suggested for detecting various signals from human bodies in material design aspects. By utilizing gel-type conductors as an active component of biological signal sensing devices, which shows excellent mechanical compliance with soft human bodies as well as unique signal transport properties, the mechanical reliability and sensing performance of devices have been significantly improved.

Firstly, a highly stretchable and reliable strain sensor was developed by incorporating poly(3,4-ethylene-dioxythiophene) poly(4-styrenesulphonate) (PEDOT:PSS) based electrically conductive gels to the Ecoflex™ dielectric layer. Due to their inherent stretchability and strain-insensitive response behavior, the conductive gels have a great

advantage in application to the capacitive type stretchable strain sensor. The fabricated devices guarantees high stretchability until 400 %, also showing a great mechanical endurance under the cyclic tensile deformation. Furthermore, additional improvement of the gauge factor of devices was achieved by introducing mechanically programmable auxetic elastomer as an dielectric layer, then overcomes the inherent limitations in performance of capacitive type strain sensors. Since all components of devices consist of soft materials, our devices show an excellent mechanical compliance for the skin-mountable applications, which can be further applied to real-time healthcare monitoring devices and human-machine interfaces controllers for soft robotics.

Secondly, to overcome the issues related to the differences in signal carriers between human/machine interfaces, we fabricated the ionic signal processing devices by using polyelectrolyte hydrogels. Through the modified design of an ion-injectable structure in microfluidic chip-based ionic diodes, direct communication between an ionic input signal and ionic devices was facilitated without an external bias in the medium. Furthermore, we firstly report on the ionic signal amplification effect observed in a fully ionic device system. As an input ionic signal is injected into the depleted state of ionic diodes, an additional ionic current across the reservoir can be generated by temporary diode breakdown. The mechanism of amplification was clearly verified by visualizing breakdown ionic flux with fluorescent dyes and analyzed by electrochemical measurement Furthermore, a considerable increase in the breakdown current was observed by scaling down the polyelectrolyte gels, which resulted in an amplification factor of around 20 times in fully ion-transfer systems. These findings can indicate future opportunities for fabricating gel- based signal processing devices for ionic systems as well as achieving intimate communication with humans.

6.2. Future works and suggested research

6.2.1. Improvement of electrical percolation network of conductive gels

As the mechanical property of gels is similar to that of biological tissues, conductive gels have a great potential for the application to skin attachable and bio-implantable devices. However, in spite of their excellent mechanical compliance with bio-systems, conductive gels still suffer from poor electrical performance for the practical use because the electrical conductivity of conducting polymer is quite lower than that of metallic conductors. Therefore, it is essential to focus on the enhancement of the electrical percolation of conducting components in a gel matrix (**Figure 6.1**).

In this respect, we suggest the introduction of Ag nanowire for the additional conducing component in gel matrix to improve the electrical percolation network of conductive gels (**Figure 6.2a**). The hybrid nanocomposites of (PEDOT:PSS)/Ag nanowire can be implemented by freeze drying the mixture of PEDOT:PSS solution and water based AgNW solution. From the microscopic analysis, the uniformly dispersed structure of AgNW mesh in PEDOT:PSS matrix was observed (**Figure 6.2b**). When they embedded in an acrylamide-based organogel, the electrical conductivity of hybrid-gel can be enhanced as Ag nanowire forms additional percolation network in the PEDOT:PSS polymeric conducting paths (**Figure 6.2c**). Moreover, during the cyclic tensile deformation with 50 % of strain, the electrical conductive property of hybrid organogels was well maintained and even improved, which can be caused by the ordering of Ag nanowire during the repeated deformation (**Figure 6.2d**). It is expected that the fabricated gel conductors can be applied to the improvement of the mechano-electrical reliability of active elements in various wearable devices.

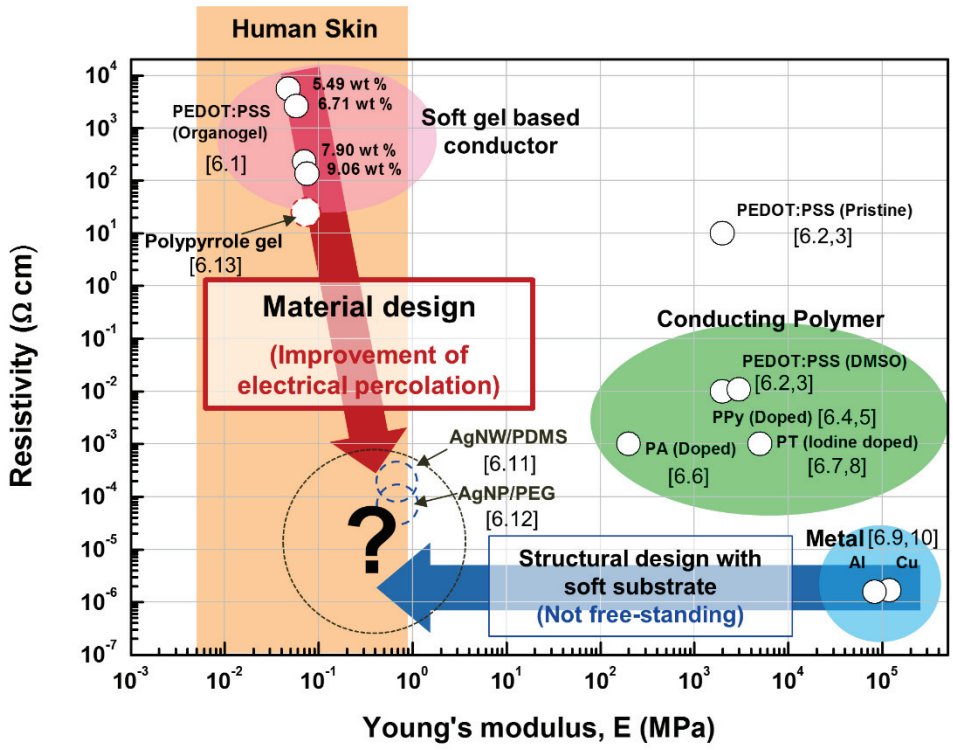

Figure 6.1 Resistivity-elastic modulus map of various conducting materials [6.1-12].

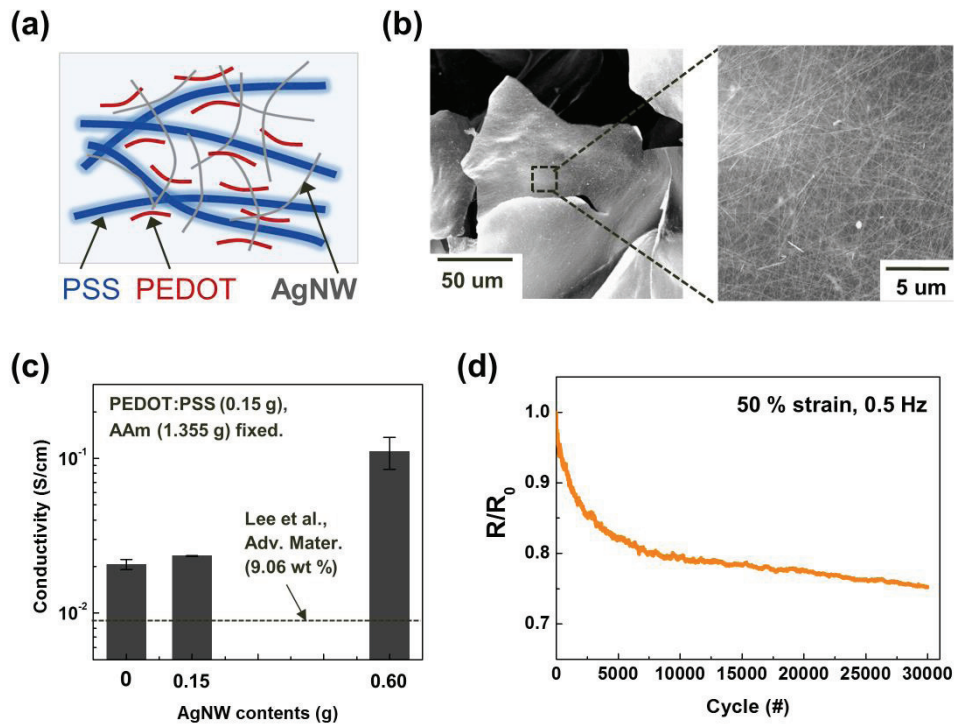

Figure 6.2 (a) Illustrations of expected percolation network in PEDOT:PSS-Ag nanowire/PAAm hybrid organogels. (b) SEM images of freeze dried PEDOT:PSS-Ag nanowire hybrid nanocomposites solute. The percolation network of Ag nanowire was well dispersed in PEDOT:PSS matrix. (c) Electrical conductivity of the hybrid organogels with varying contents of Ag nanowire. (d) Resistance changes of hybrid organogels during the repeated deformation. Continuous resistance decreases of hybrid gel were measured until 5000 cycles.

6.2.2. Integration of the ionic device with biological systems

In this study, direct ionic signal detection of ionic signals was clearly demonstrated through the modified design of ionic devices in a microfluidic chip, which can be called an open junction ionic diode (OJID). By utilizing OJIDs, it is expected to acquire the biological ionic signals with a high efficiency. **Figure 6.3** shows a suggested working principle of OJIDs for sensing neuronal signals from nerve cells. In the previous work, micro-patterning of hippocampal neurons on the microfluidic chips was achieved through the guided growth of axons[6.13], and it can be also utilized to OJIDs. At the initial stage, the OJIDs maintain OFF-state with the reverse bias. Upon neural stimulation, however, the K^+ ions are transmitted to the devices through the depolarization of nerve cells and the change of ionic currents can be observed. By measuring the responsive ionic currents during the perturbation of cells, the minute ionic signals can be detected signals from neuronal cells with lessening signal transfer loss.

Finally, we are dreaming of the ion-based signal processing systems that can communicate with biological area. Starting from sensing of neural signals, we would like to transfer the neural signals through artificial nerves, calculate and memorize with an artificial brain, and finally, actuate through an artificial muscles. With consideration of various design factors for bio-integration such as biocompatibility, biodegradability and mechanical compliance, the gel-based ionic devices can suggest a new paradiagm for intimate communication with biological systems.

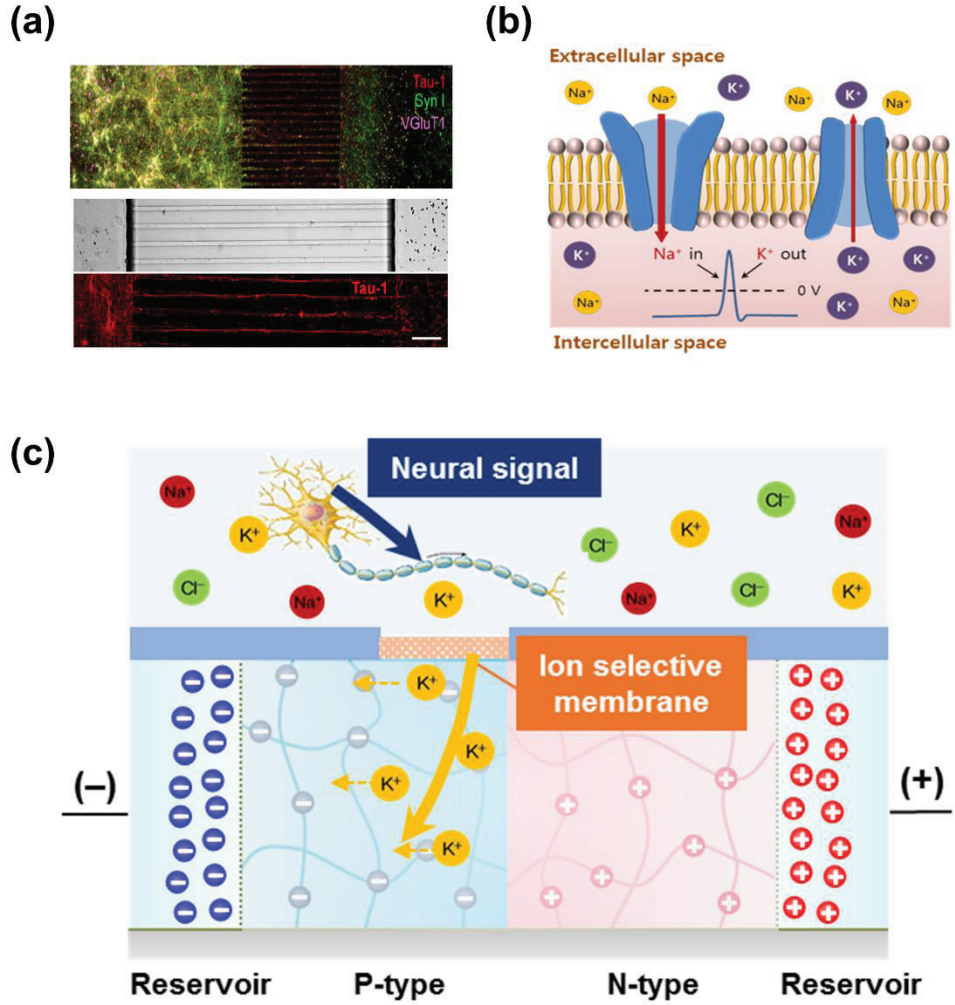

Figure 6.3 (a) Images of guided hippocampus neurons on the glass chip[6.13]. (b) Propagation of an action potential in neurons mediated by transportation of cations (Na^+, K^+) across the cell membrane through the each ion channel. (c) Schematics for showing the suggested mechanisms of recording neuronal signals upon somatic stimulation by using an OJID.

References

[6.1] Lee, Y. Y. *et al.* A Strain-Insensitive Stretchable Electronic Conductor: PEDOT:PSS/Acrylamide Organogels. *Adv Mater* **28**, 1636-1643, doi:10.1002/adma.201504606 (2016).

[6.2] Lang, U., Naujoks, N. & Dual, J. Mechanical characterization of PEDOT:PSS thin films. *Synthetic Metals* **159**, 473-479, doi:10.1016/j.synthmet.2008.11.005 (2009).

[6.3] Kim, J. Y., Jung, J. H., Lee, D. E. & Joo, J. Enhancement of electrical conductivity of poly(3,4-ethylenedioxythiophene)/poly(4-styrenesulfonate) by a change of solvents. *Synthetic Metals* **126**, 311-316, doi:DOI 10.1016/S0379-6779(01)00576-8 (2002).

[6.4] Cuenot, S., Demoustier-Champagne, S. & Nysten, B. Elastic modulus of polypyrrole nanotubes. *Phys Rev Lett* **85**, 1690-1693, doi:10.1103/PhysRevLett.85.1690 (2000).

[6.5] Kang, H. C. & Geckeler, K. E. Enhanced electrical conductivity of polypyrrole prepared by chemical oxidative polymerization: effect of the preparation technique and polymer additive. *Polymer* **41**, 6931-6934, doi:Doi 10.1016/S0032-3861(00)00116-6 (2000).

[6.6] Polymeric materials encyclopedia v. CD-ROM (CRC Press,, Boca Raton, 1996).

[6.7] Wang, X. S. & Feng, X. Q. Effects of thickness on mechanical properties of conducting polythiophene films. *J Mater Sci Lett* **21**, 715-717, doi:Doi 10.1023/A:1015737106002 (2002).

[6.8] Guenthner, A. J. *et al.* New Insights into Structure–Property Relationships in Thermosetting Polymers from Studies of Cocured Polycyanurate Networks. *Macromolecules* **45**, 211-220, doi:10.1021/ma202513h (2011).

[6.9] The periodic table of the elements, https://www.webelements.com/

[6.10] Wikipedia, The Free Encyclopedia, https://en.wikipedia.org/wiki/

[6.11] Xu, F. & Zhu, Y. Highly conductive and stretchable silver nanowire conductors. *Adv Mater* **24**, 5117-5122, doi:10.1002/adma.201201886 (2012).

[6.12] Hyun, D. C. *et al.* Ordered zigzag stripes of polymer gel/metal nanoparticle composites for highly stretchable conductive electrodes. *Adv Mater* **23**, 2946-2950, doi:10.1002/adma.201100639 (2011).

[6.13] Kim, E. J., Jeon, C. S., Lee, S. Y., Hwang, I. & Chung, T. D. Robust Type-specific Hemisynapses Induced by Artificial Dendrites. *Sci Rep* **6**, 24210, doi:10.1038/srep24210 (2016).

요약(국문초록)

최근 웨어러블 소자 제작이 미래 소자 개발의 주요 트렌드로 주목을 받고 있다. 기존 실리콘 기판을 넘어 보다 유연한 기판 위에 구현되어 피부에 붙이거나 몸속에 심을 수 있는 형태로 개발됨으로써 신체에서 발생하는 다양한 신호를 보다 밀접하게 받아들이는데 그 목적이 있으며, 실제로 헬스케어, 엔터테인먼트, 소프트 로봇 제작 등 다양한 분야에서의 활용 가능성이 제시되고 있다. 그러나 현재까지 개발되고 있는 웨어러블 소자의 경우 엑티브 구성요소를 담당하는 재료의 기계적 물성이 기판 재료에 비해 크게 고려가 되지 않았던 관계로 실제 몸에 착용하였을 때 반복 변형에 의한 신뢰성 이슈가 필연적으로 발생하게 된다. 더욱 나아가 우리 몸 속에서 발생하는 생체 신호는 이온의 흐름을 기반으로 하고 있기 때문에 기존 전자소자의 원리를 통해 측정하게 될 경우 신호 전달 시스템 불일치로 인한 효율 저하가 필연적으로 발생할 수 밖에 없다. 이러한 문제점들을 해결하기 위해서는 기판과 더불어 엑티브 구성요소를 이루는 재료에 대한 근본적인 개선이 필요하다고 볼 수 있다.

이를 위해 본 연구에서는 소프트 젤 기반 전도성 물질을 도입하여 현재 웨어러블 소자에서 발생하고 있는 각각의 이슈들을 해결하고자 한다. 젤은 다량의 액체를 기반으로 하고 있기 때문에 소프트하고 유연한 기계적 특성을 보유하고 있으며, 내부에 어떠한 전도성 물질을 포함하느냐에 따라 다양한 형태의 신호전달 특성을 보유할 수 있다. 첫 번째 파트에서는 전도성 고분자를 기반으로 한 전기 전도성 젤을 웨어러블 변형 센서에 도입하여 소자의 기계적 특성 및 신뢰성을 향상시킨 연구를 진행하였다.

전도성 젤의 경우 신축 환경에서도 젤 내부에 얽혀있는 고분자 전도 경로가 풀어지면서 자체적인 전기적인 특성을 유지할 수 있다는 특성을 가지고 있기 때문에 이를 정전용량 방식의 신축성 센서의 전극물질로 도입하였을 때 최대 400 % 의 신축성 및 높은 기계적 신뢰성을 나타냄을 확인할 수 있었다. 더불어 기판물질을 포함한 모든 구성 요소가 소프트 재료를 기반으로 이루어져 있기 때문에 피부에 부착시켰을 때 매우 우수한 착용감을 보여줌과 동시에 안정적으로 손가락 및 팔꿈치의 움직임을 실시간으로 감지할 수 있음을 확인하였다. 또한 추가적으로 음의 푸아송비를 가지는 2 차원 요각구조 옥세틱 구조체를 변형센서 유전체 내부에 도입시켜 센서 특성을 향상시킴으로써 소자 활용 가능성을 높이기 위한 방안을 제시하였다.

두 번째 파트에서는 외부 이온 신호와의 직접적인 연동이 가능한 이오닉 소자를 개발한 연구를 밝히고자 한다. 최근 금속 및 전도성 고분자를 기반으로 한 전극을 신체 내에 삽입시켜 전자소자를 통한 생체신호를 얻기 위한 다양한 연구가 이루어지고 있다. 그러나 기존 전극물질은 재료적 측면에서 생체 적합성이 다소 떨어질 뿐 아니라 우리 몸은 기본적으로 전자가 아닌 이온의 흐름을 바탕으로 한 신호전달체계를 바탕으로 하고 있기 때문에 신호 교류 측면에서 근본적인 문제점을 내포하고 있다. 이러한 측면에서 하이드로젤은 소프트하며, 뛰어난 생체 적합성을 보유함과 동시에 다량의 용존 이온을 통한 신호 전달에 유리하다는 장점을 가지고 있기 때문에 이를 바탕으로 소자를 구현할 수 있다면 생체 신호와의 연동 측면에서 뛰어난 특성을 기대할 수 있다. 본 연구에서는 마이크로플루이딕스 칩 기반 하이드로젤 이오닉 다이오드 소자의 접합 부위가 개방된 형태의 구조를 설계하여 외부의 이온신호의 직접적인 주입

및 연동이 가능한 시스템을 제안하였다. 이를 통해 이오닉 소자를 활용한 직접적인 이온 농도 신호 검출이 가능함을 확인하였다. 더불어 다양한 이온 신호 체계에서 발생하는 증폭현상을 발견한 후 전기화학, 광학, 전산 모사 등 다방면의 분석을 통해 이에 대한 메커니즘을 규명하는 연구를 진행하였다. 마지막으로 소자 구조 개선을 통해 추가적으로 증폭효과를 향상시킬 수 있는 설계 가이드라인을 보여줌으로써 향후 생체 신호에서 발생하는 미세 이온 신호를 보다 효과적으로 측정할 수 있는 새로운 방안을 제시하고자 한다.

표제어: 웨어러블 변형 센서, 신축성 전극, 이오닉 다이오드, 이온 신호 증폭, 다전해질 하이드로젤, 이오닉 소자 회로 요소

학 번: 2013-20618

CURRICULUM VITAE

Seung-Min Lim

EDUCATION

2013. 3. ~ 2019.8. ***Ph.D.*** *(Integrated course)*

Department of Materials Science and Engineering

Seoul National University, Seoul, Korea

Advisor: Young-Chang Joo, Professor

2013. 2. ***B. S.,*** Department of Materials Science and Engineering (*Cum Laude*)

Seoul National University, Seoul, Korea

RESEARCH EXPERIENCES

Hydrogel based ionic devices

- Synthesis of hydrogels and polyelectrolyte hydrogels
- Electrochemical characterization of ionic transport properties of hydrogels
- Fabrication of microfluidic chip-based ionic circuit elements
- Analysis of signal transduction mechanisms in ionic devices

Soft materials based stretchable electronic devices

- Synthesis of conductive gels by incorporating conducting polymers
- Characterization of electrical and mechanical properties of conductive gels

- Fabrication of soft material-based electronic devices for wearable applications (Stretchable strain sensors, Wireless power transfer devices)
- Formation of stable soft/hard contact

Amorphous oxide semiconductor (AOS)-based electronic devices

- Development of novel metal/oxide/metal structured devices for investigation of structural relaxation in AOS
- Optimization of thermal stability of AOS-based through Oxygen Vacancy Control at Metal/Oxide Interfaces
- Electrical characterization and analysis of conduction mechanisms of AOS based two terminal devices

Reliability of advanced metailization

- Characterization of time dependent dielectric breakdown (TDDB) in Cu damascene interconnect
- Measurement and analysis of electromigration (EM)-induced failure in Cu damascene interconnects

AWARDS AND HONORS

2019 **Bronze Prize**, **25th Humantech Paper Award**
Samsung Electronics, Seoul, Korea

2017 **Best Poster Award nominated**
2017 MRS Spring Meeting, Phoenix, Arizona, USA

2017~ **Ph. D. Scholarship**
Samsung Electronics Co., Ltd., Korea

2016 **Silver Prize, 22th Humantech Paper Award**

Samsung Electronics, Seoul, Korea

2013 **Alumni Prize (Department of Material Sciences and Engineering)**

Seoul National University, Korea

PROFESSIONAL ACTIVITIES

2017 **Chapter Representative of Seoul National University**

MRS University Chapter, USA

2015 **Conference Organizing Staff**

Advanced Metalization Conference 2015 25th Asian Session, Korea

2008 ~ 2010 **Mandatory Military Service**

Sergeant, Republic of Korea Army, Korea

PUBLICATIONS

- **Seung-Min Lim**, Hyunjae Yoo, Min-Ah Oh, Seok Hee Han, Hae-Ryung Lee, Taek Dong Chung, Young-Chang Joo, and Jeong-Yun Sun, "Ion-to-Ion Amplification through an Open Junction Ionic Diode", *Proc. Natl. Acad. Sci. USA,* online published (2019)
- Young-Joo Lee†, **Seung-Min Lim**†, Seol-Min Yi, Jeong-Ho Lee, Sung-gyu Kang, Gwang-Mook Choi, Heung Nam Han, Jeong-Yun Sun, In-Suk Choi*, and Young-Chang Joo*, "Auxetic Elastomers: Mechanically Programmable Meta-Elastomers with an Unusual Poisson's Ratio Overcome the Gauge Limit of a Capacitive Type Strain Sensor", *under review*
- **Seung-Min Lim**†, Han-Wool Yeon†, Gi-Baek Lee, Min-Gi Jin, Seung-Yong Lee, Janghyun Jo, Miyoung Kim, & Young-Chang Joo*, "Thermally Stable Amorphous Oxide-based

Schottky Diodes through Oxygen Vacancy Control at Metal/Oxide Interfaces" *Scientific Reports,* 9, 7872 (2019)

- Gwang Mook Choi, **Seung-Min Lim**, Yoo-Yong Lee, Seol-Min Yi, Young-Joo Lee, Jeong-Yun Sun, and Young-Chang Joo*, "PEDOT:PSS/Polyacrylamide Nanoweb: Highly Reliable Soft Conductors with Swelling Resistance", *ACS Appl. Mater. Interface.*, 11, 10099-10107 (2019)
- Hae-Ryung Lee, Jaesung Woo, Seok Hee Han, **Seung-Min Lim**, Sungsoo Lim, Yong-Woo Kang, Won Jun Song, Jae-Man Park, Taek Dong Chung, Young-Chang Joo, and Jeong-Yun Sun*, "A Stretchable Ionic Diode from Copolyelectrolyte Hydrogels with Methacrylated Polysaccharides", *Adv. Funct. Mater.*, 29, 1806909 (2019)
- Yoo-Yong Lee, Ho-Young Kang, Seok Hyeon Gwon, Gwang Mook Choi, **Seung-Min Lim**, Jeong-Yun Sun, and Young-Chang Joo*, "A Strain-Intensive Stretchable Electronic Conductor: PEDOT-PSS/Acrylamide Organogels", *Adv. Mater.*, 28, 1636 (2016)
- Han-Wool Yeon, **Seung-Min Lim**, Jung-Kyu Jung, Hyobin Yoo, Young-Joo Lee, Ho-Young Kang, Young-Jin Park, Miyoung Kim, and Young-Chang Joo*, "Structural-Relaxation-Driven Electron Doping in Amorphous Oxide Semiconductors through the Increase in Concentration of Oxygen Vacancies in the Shallow-Donor State", *NPG Asia Materials*, 8, e250 (2016)
- Kyung-Tae Jang, Yong-Jin Park, Min-Woo Jeong, **Seung-Min Lim**, Han-Wool Yeon, Ju-Young Cho, Min-Gi Jin, Jin-Sub Shin, Byoung-Wook Woo, Jang-Yong Bae, Yu-Chul Hwang, and Young-Chang Joo*, "Electromigration behavior of advanced metallization on the structural effects for memory devices", *Microelectronic Engineering.*, 156, 97-102 (2016)
- Su Hong Kwak, Seung-Ryong Kwon, Seol Baek, **Seung-Min Lim**, Young-Chang Joo, and Taek Dong Chung*, "Densely charged polyelectrolyte-stuffed nanochannel arrays for power generation from salinity gradient", *Scientific Reports*, 6, 26416 (2016)

- Yoo-Yong Lee, Gwang Mook Choi, **Seung-Min Lim**, Ju-Young Cho, In-Suk Choi, Ki Tae Nam and Young-Chang Joo*, "Growth Mechanism of Strain-Dependent Morphological Change in PEDOT:PSS Films", *Scientific Reports*, 6, 25332 (2016)
- Han-Wool Yeon, Jun-young Song, **Seung-Min Lim**, and Young-Chang Joo*, "Effect of pulsed electric fields on dielectric breakdown in Cu damascene interconnects", *Appl. Phys. Express*, 8, 031502 (2015)
- Yongwon Chung, Sanggeun Lee, Chandreswar Mahata, Jungmok Seo, **Seung-Min Lim**, Min-su Jeong, Hanearl Jung, Young-Chang Joo, Young-Bae Park, Hyungjun Kim, and Taeyoon Lee*, "Coupled Self-assembled Monolayer for Enhancement of Cu Diffusion Barrier and Adhesion Properties", *RSC Advances*, 4, 60123-60130 (2014)

PRESENTATIONS IN INTERNATIONAL CONFERENCE

- **Seung-Min Lim**, Yoo-Yong Lee, Seok Hyeon Gwon, Gwang Mook Choi, Jeong-Yun Sun* and Young-Chang Joo*, "Soft Electronic Conductors based on PEDOT:PSS based Hybrid-gels", *The 16th International Nanotech Symposium& Nano-Convergence Exhibition (Nano Korea 2018),* Ilsan, Korea (2018)
- **Seung-Min Lim**, Yoo-Yong Lee, Jung-Kwon Yang, Seok Hyeon Gwon, Gwang Mook Choi, Jeong-Yun Sun* and Young-Chang Joo*, "Highly Electrically Conductive Soft Materials based on PEDOT:PSS-Metal Nanowire Hybrids/Acrylamide Organogels", *2017 Materials Research Society (MRS) Spring Meeting*, Phoenix, USA (2017)
- **Seung-Min Lim**, Yoo-Yong Lee, Jung-Kwon Yang, Seok Hyeon Gwon, Gwang Mook Choi, Jeong-Yun Sun* and Young-Chang Joo*, "PEDOT:PSS based hybrid Organogels for the Soft Electronic Conductors", *4th International Conference on Electronic Materials and Nanotechnology for Green Environment (ENGE 2016)*, Jeju, Korea (2016)

- **Seung-Min Lim**, Han-Wool Yeon,Seung-Yong Lee, Janghyun Jo, Miyoung Kim and Young-Chang Joo*, "Modulation of Oxygen Vacancy and Stoichiometry in Amorphous Metal Oxides at Metal/Oxide Interfaces for Enhancement of Rectifying Property", *Advanced Metalization Conference 2015 25th Asian Session*, Seoul, Korea (2015)
- **Seung-Min Lim**, Han-Wool Yeon, and Young-Chang Joo* "High Performance Schottky Diode for Crossbar Array Memory Fabricated through Controlled Reaction of Cu-Mn Interconnects and Amorphous Indium Gallium Zinc Oxide", *2014 Materials Research Society (MRS) Spring Meeting*, San Francisco, USA (2014)

PATENTS

- Young-Chang Joo, In-Suk Choi, Young-Joo Lee, **Seung-Min Lim**, "Capacitor type strain sensor and manufacturing method thereof', Korea Patent (10-2019-0006444), PCT Patent (PCT/KR2019/000859)
- Young-Chang Joo, In-Suk Choi, Young-Joo Lee, **Seung-Min Lim**, Jung-Kwon Yang, Gwang Mook Choi, "Stretchable Substrate Structure for Enhanced Stretchability and Reliability of Stretchable Device", Korea Patent (10-2017-0155974)

R&D PROJECTS

- "Hydrogel-based Ionic Transistor", SRFC-MA1402-11, Samsung Research Funding Center of Samsung Electronics, 2014. 12. ~ 2018. 11.
- "Development of Highly Reliable Electrode Material for Next Generation Cross-Point Memory Device", Cooperative System Project funded by Samsung Electronics Co., Ltd., 2015. 7. ~ 2019. 6.
- "Soft Robotics Research Center", Engineering Research Center (ERC) Program funded by National Research Foundation of Korea., 2017. 1. ~ 2017. 12.

- “Development of Reliable Fine-Pitch Metallization Technologies”, Technology Innovation Program funded by the Ministry of Knowledge Economy, 2013. 3. ~ 2015. 2.
- “Research of Reliability of Cu Interconnects under Dynamic Electric Field Environment”, Cooperative System Project funded by Samsung Electronics Co., Ltd., 2013. 3. ~ 2015. 3.